國立交通大學

材料科學與工程學系

碩 士 論 文

自組裝膠體晶體及其金屬反蛋白石結構之製備及特性分析

Fabrication and Characterization of Planar and Cylindrical Colloidal Crystals and their Nickel Inverse Opals

研究生： 賴俊翰 (C. H. Lai)

指導教授： 吳樸偉 博士 (Dr. P. W. Wu)

中 華 民 國 九十八 年 六 月

自組裝膠體晶體及其金屬反蛋白石結構之製備及特性分析

Fabrication and Characterization of Planar and Cylindrical Colloidal Crystals and their Nickel Inverse Opals

研究生：賴俊翰　　Student: Chun-Han Lai

指導教授：吳樸偉 博士　　Advisor: Pu-Wei Wu

國 立 交 通 大 學

材料科學與工程學系

碩 士 論 文

A Thesis

Submitted to Department of Materials Science and Engineering

College of Engineering

National Chiao Tung University

in partial Fulfillment of the Requirements

for the Degree of

Master

in

Materials Science and Engineering

June 2009

Hsinchu, Taiwan, Republic of China

中 華 民 國 九十八 年 六 月

自組裝膠體晶體及其金屬反蛋白石結構之製備及特性分析

研究生：賴俊翰　　指導教授：吳樸偉 博士

國立交通大學材料科學與工程學系

摘　　要

本研究以電泳披覆法 (Electrophoretic deposition) 分別製作平板及柱狀自組裝膠體晶體於 ITO 導電玻璃及碳纖維上。以最佳化之參數所製備之平板膠體晶體具有單一光子能隙 (Photonic band gap) ，其能隙位置會隨著實驗中使用之微球尺寸而改變；而柱狀膠體晶體由於反射面積有限，加上自組裝之微球延柱狀表面呈輻射狀之排列，導致其光子能隙強度減弱，然而，其反射峰之半高寬卻因柱面之特性而增加。另外，柱狀膠體晶體表面由於入射光之散射，因此可觀察到彩虹般的平行線。　本研究接著以定電壓 1 V 在 50 ℃下進行電鍍 (Electrodeposition) ，將鎳填入膠體晶體之孔隙中，製備金屬反蛋白石結構，再以 250℃之熱處理去除結構內之聚苯乙烯微球。由於膠體晶體之侷限，金屬反蛋白石結構具有特定的成長方向。另外，隨著熱處理的時間增加，聚苯乙烯可完全被移除，同時結晶性也隨之增強，電阻率隨之下降。在光學分析上，平板鎳之反蛋白石結構具有光子能隙邊界 (Photonic band edge) ，而柱狀結構則具有共振腔之特性。

Fabrication and Characterization of Planar and Cylindrical Colloidal Crystals and their Nickel Inverse Opals

Student: Chun-Han Lai Advisor: Dr. Pu-Wei Wu

Department of Materials Science and Engineering

National Chiao Tung University

Abstract

Planar and cylindrical colloidal crystals were fabricated by electrophoretic deposition with 460 and 660 nm PS microspheres on ITO-glass and carbon fibers, respectively. To improve the quality of the colloidal crystals, variables including microsphere concentration, electrical field, and deposition time were investigated. With the optimized process, the multi-layer colloidal crystals with ordered structure could be obtained within 1 hr. In planar colloidal crystals, we observed an obvious photonic band gap in reflectance spectra. In contrast, a series of iridescent fringes was present in cylindrical colloidal crystals. To fabricate Ni inverse opals, potentiostatic electrodeposition was carried out on the colloidal crystals. With careful control in the plating step, we were able to obtain inverse opals in finite thickness. To remove the PS microspheres, the deposited samples underwent chemical dissolution using ethyl acetate and thermal oxidation at 250 ℃ after the electrodeposition. The heat treatment was able to clean the PS microspheres without structure distortion. Meanwhile, the crystallinity of the Ni inverse opals was improved during the heat treatment.

Acknowledgements

兩年的研究所生涯，倏忽即逝。此論文的完成，不過是這兩年的一小片段，而知識和認知的累積，卻是這兩年最大的收穫。在此要感謝這兩年研究生活中陪我走過的每一個人；因為與你們每個人的相遇，使得這份論文能夠以我現有的知識順利完成。

首先，要感謝的是父親、母親及家人們，你們打造了一座完美的避風港，在心理上及經濟上給予我相當的支持，使我能在他鄉一心一意的做研究。接著感謝女友，有妳的相伴，碩二生活充滿光彩，感謝妳總能在失意時給予我最大的關懷，並以歡笑帶給了我對生活的期待。

接著，要感謝實驗室的大家。首先是苡叡學長，感謝你在實驗上及專業知識上給予我最大的幫助，讓我在嘗試的過程中找到最近的路；感謝勝結大哥，在我還是專題生的時候在凌晨三點協助拍攝 SEM；感謝雲閔學長，總是提供我生活上的小智慧，並陪我一起跨越美國國界。感謝于凡學妹、冠廷學弟在我碩一參與的計畫中大力相助，使計畫得以順利結案。感謝同屆的戰友：境妤、和成、張三角、梁阿夢還有柚子，在最後幾個月於實驗上交換心得，於論文上給予協助。

本論文中，特別感謝楊玉麟學長於光學量測上之協助與討論，陳智教授實驗室於儀器協助及操作之指導，岱民同學於電性量測上之協助與討論，以及儷尹學妹於電泳材料上之合成，使此論文能有健全的發展。

最後，我要感謝我的指導教授，吳樸偉博士在這三年的實驗生涯中大力栽培，無論是知識上、金援上，令我沒齒難忘。

Contents

List of Figures

List of Table

Chapter 1

Introduction

Concept of photonic crystals (PCs) was first introduced in 1987 [1,2]. The PCs provide characteristic optical responses due to their artificial lattices, which amplify the resonance of electromagnetic waves at proper wavelengths. Meanwhile, at specific wavelengths, the waves in the PCs interfere with others destructively, producing a photonic bad gap (PBG). In short, devices with a PBG can reveal a high reflectance at specific wavelengths, and this property is attractive for optical applications.

To fabricate photonic crystals, materials with distinct refractive index are arranged in a periodic pattern. To date, fabrications of desirable periodic structures have received substantial attention from research groups around the world. In general, methods for fabricating the PCs can be separated into two parts: lithography in semiconductor process and self-assembly of colloids [3-5]. Lithography technique can provide high accuracy in structural design and excellent quality for the 2-D PCs. However, the inherent high cost and long processing time are the limiting factors for commercial application. Besides, it is challenging to fabricate a 3-D complex structure using this method.

In contrast, self-assembly of colloidal crystals is relatively low cost, and the process is simpler than that of the semiconductor one. Therefore, colloidal crystals self-assembled by sub-micron microspheres such as polystyrene and silica were widely studied [6,7]. The self-assembly is typically carried out in a stable suspension, Methods include physical confinement, gravitational sedimentation, and electrophoretic deposition (EPD) [4, 8-10] are explored as the driving force to arrange these microspheres. With the EPD process, the colloidal crystals can be prepared within a short period compared with other methods [11]. In addition, to make colloidal crystals multifunctional, periodical structures in different shapes

were also studied [12]. For example, rod-like or tubular structures were reported and their fabrication techniques utilized driving forces such as shape-confinements and capillary forces [13-16].

3-D metallic PCs have attracted considerable attention since they exhibit a complete PBG at a specific range of wavelength [5, 17-19]. To fabricate the 3-D metallic PCs, the colloidal crystals are used as a 3-D template. By filling voids within the template with high refractive index materials, inverse opals of 3-D metallic PCs can be obtained. Deposition techniques including sol-gel [20], CVD [21], electroless deposition [22], and electrodeposition [23] are commonly used to prepare inverse opals. Among them, the electrochemical route provides a simple and inexpensive way to prepare the 3-D metallic inverse opals.

In this work, we demonstrate the fabrication of colloidal crystals by electrophoretic deposition. Sequentially, we prepare their inverse opals by nickel electrodeposition (NED). After removing the PS microspheres, both planar and cylindrical nickel inverse opals are obtained.

Chapter 2

Literature Review

2.1 Photonic Crystals

In semiconductors, the propagation of electrons is confined with periodic potential induced by well-arranged ions. With these periodic potentials, these electrons work as wave packages that interact with each other, forming an "electronic band gap". According to the wave-particle duality, the velocity of a propagating electromagnetic (EM) wave is determined by the refractive index of the material. Therefore, as the EM waves are traveling in an artificial material with periodic refractive indices, a wave diffraction will be generated from the material. A high reflectance at a regime of frequency is obtained as a result of destructive interference by the diffracting waves. Namely, this is so-called "photonic band gap (PBG)"

This PBG character was first addressed by E. Yablonovitch in 1987 [1], and was utilized to reduce the undesirable spontaneous emissions in semiconductor lasers. In the same year, S. John [2] also published a paper about theoretical calculation of photon localization within periodic structures. After two years, the first hybrid photonic band structure in face-centered lattice was developed [24]. Their experiment results are presented in Fig. 2.1. Later, the band structure was applied to non-spherical shapes, and a complete PBG for s and p polarizations were also discussed. Their fabrication scheme and results are provided in Fig. 2.2 [25]. In addition, similar simulations were also developed for the PCs with different structures and materials. They estimated that the PBG was expected to be occurring with a refractive index contrast of 2.8 for dielectric materials [26, 27]. Therefore, on the reflectance spectrum, the PCs made of dielectric material revealed a single peak as PBG. This is because the dielectric materials were usually transparent for EM waves, and their

refractive indices are rarely changed upon different wavelengths [28]. In contrast, the refractive indices of metal are contingent on the frequency of incident waves. The metallic PCs demonstrated a photonic band edge at a specific wavelength, above which the incident light would be totally reflected [19,29].

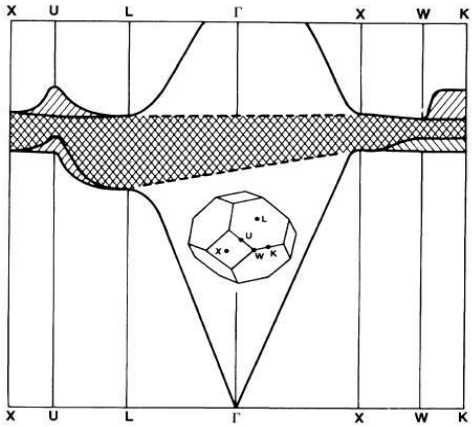

Figure 2.1 First hybrid band structure of photonic crystal in a face-centered arrangement [24].

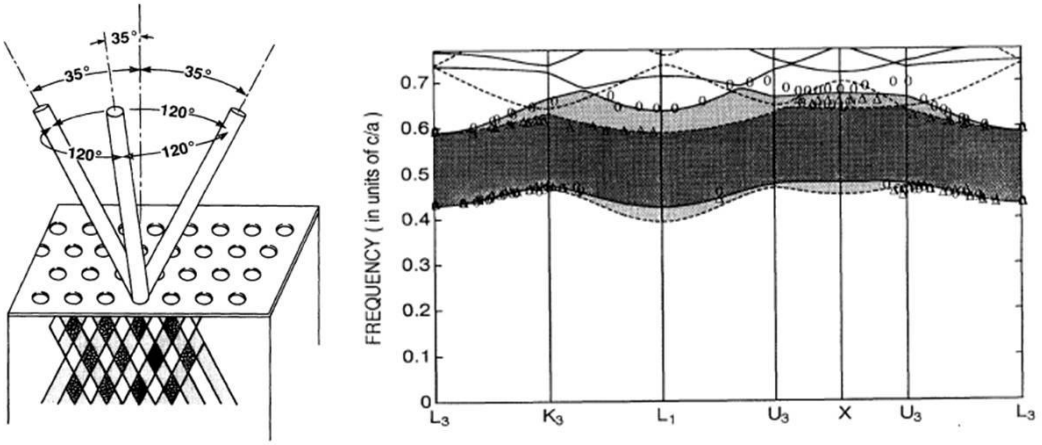

Figure 2.2 Method to construct a FCC structure with non-spherical shapes and the forbidden band diagram of the structure [25].

This unique feature makes the PCs attractive for optical applications. For example, the 1-D PCs in layer structure were commonly used as dielectric mirrors [30, 31]. These layers provided designed geometry that offered a 180° phase difference between the incident and

reflective EM waves [32], as shown in Fig. 2.3. Moreover, PBG optical fibers were fabricated with period 2-D PCs [15,33], as provided in Fig. 2.4(a). The incident light propagated in the middle of the fiber, and the dispersion of wave was confined inside the structure, as presented in Fig. 2.4(b). To extend the PBG to 3-D structures, a diamond structure [34] was designed to have the complete PBG, and its hybrid band structure are presented in Fig. 2.5. So far, we can conclude that the designs for the PCs are mainly based on the periodic structure and materials with distinct index of refraction.

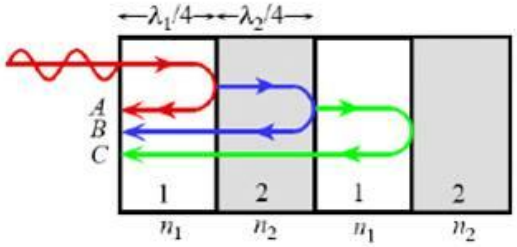

Figure 2.3 A schematic illustration of the principle of the dielectric mirror for 1-D PCs [32].

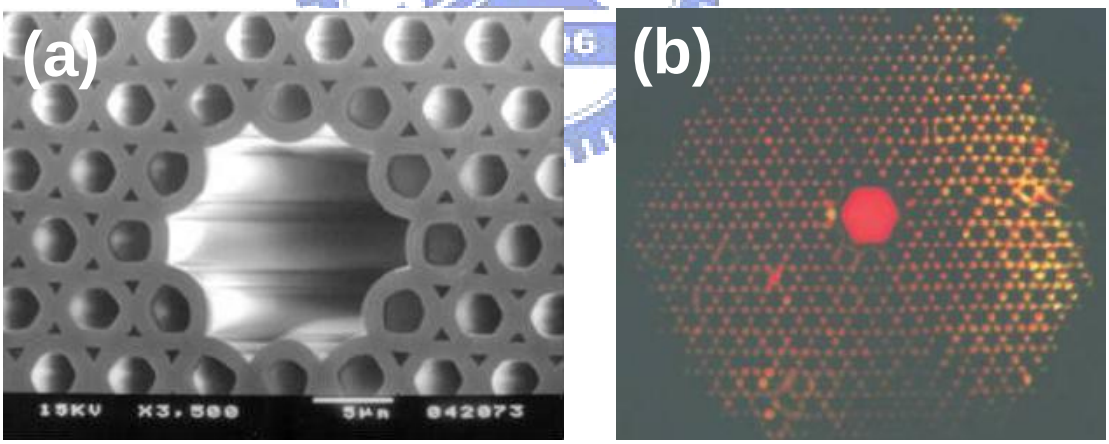

Figure 2.4 (a) SEM image of a PBG optical fiber and (b) the optical micrograph of the field intensity pattern at the optical exit face [33].

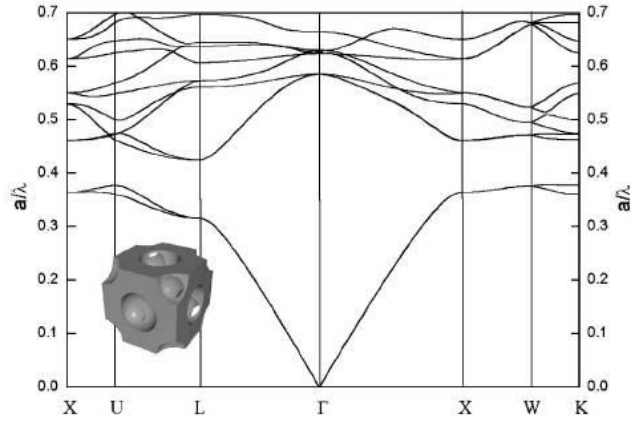

Figure 2.5 Photonic band diagram of a silicon diamond opal [34].

2.2 Electrophoretic Deposition

Electrophoretic deposition (EPD) is a fabrication technique involving driving of charged particles in a suspension to the working electrode [35]. Before initiaing the EPD process, a stable suspension is required. The DLVO theorem demonstrated a model to explain how the colloids could suspend stably. In a suspension system, some ions of suspension are physically attached on the colloids, forming a layer of ions that is defined as the "Stern layer". In a negative-charged stern layer, positive ions in the solution would be attracted, raising a potential distribution from the particles to the bulk solution. The region where the potential works is defined as the diffusion layer. As the colloids are getting closer, their diffusion layers would interact with each other. Attractive and repulsive forces are generated from the interaction of the diffusion layers, as presented in Fig. 2.6(a). With only one minimum M_1, the particles are likely to aggregate together, forming clusters. By extending the repulsive field, a metastable state M_2 could form, as shown in Fig. 2.6(b). The colloids ccould stay at the position of M_2 from others, providing a stable suspension.

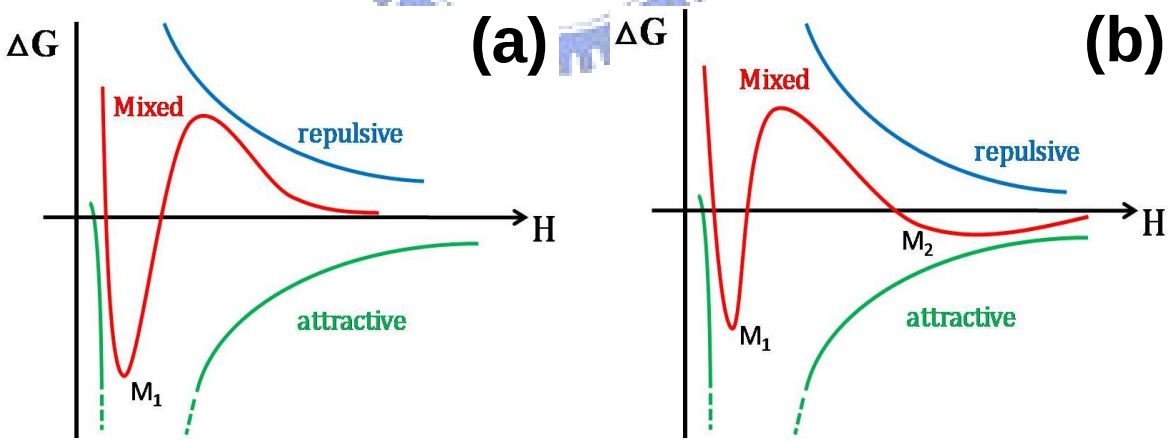

Figure 2.6 A plot of Free energy (ΔG) dependence on distance (H) from a particle surface (a) before and (b) after extending the repulsive field.

This technique was further applied to prepare colloidal crystals [11]. To explain the particle migration in EPD process, a hydrodynamic model combining electrophoresis and

electroosmosis was proposed in 1997 [36]. The model rationalized that the cluster of microspheres was formed by long range colloidal forces, including electrical field and fluid flow. Afterward, the colloidal crystals were prepared with PS microspheres in various sizes by the EPD [9]. Their optical responses as a function of particle size were discussed, and the PBG on reflectance spectra revealed a peak with high intensity about 0.8. To control the self-assembly under an electrical field, an electrophoretic phase diagram was developed [10]. The arrangement of particles can be adjusted by the particle concentration and electrical fields, as presented in Fig. 2.7. With careful control in the electrical field and suspensions, we were capable to prepare large-area colloidal crystals by electrophoretic deposition [37].

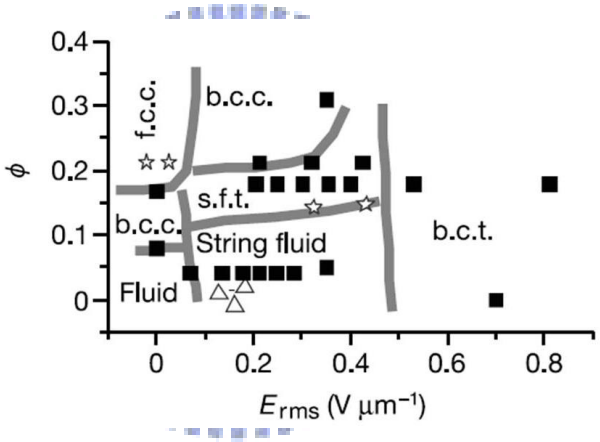

Figure 2.7 A volume fraction-electric field phase diagram for the EPD [10].

Cylindrical colloidal crystals were usually fabricated by capillary forces within a physical confinement [13-16, 38-40] or by dip-coating [41]. With a slow evaporation rate, the microspheres were self-assembled on a curved surface, as shown in Fig. 2.8. As clearly shown in Fig. 2.9, the sizes for these cylindrical colloidal crystals were limited by the mold in their fabrications. In addition, the low evaporation rate during the process was time-consuming. In contrast, the EPD process allows a tunable size. For making colloidal cylinders, the thickness can be increased with deposition time, and the length is simply

controlled by substrates. Besides, the fabrication time is shortened and not as long as that for slowly evaporation.

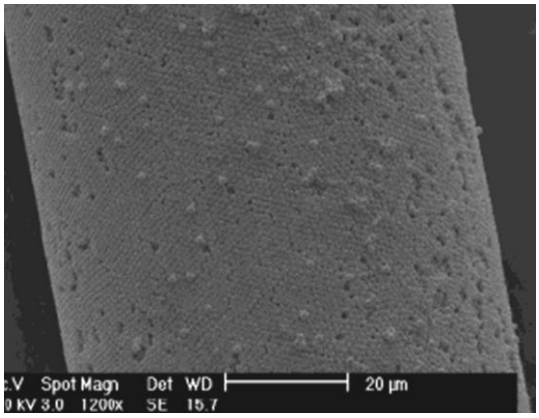

Figure 2.8 SEM image of cylindrical colloidal crystals fabricated by capillary force within a micro-capillary [15].

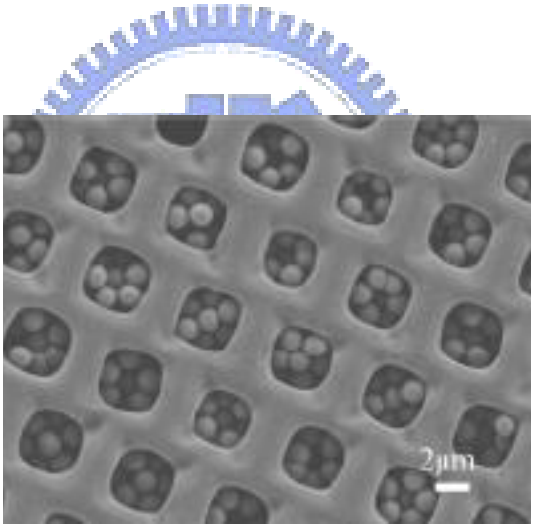

Figure 2.9 Top view SEM image of cylindrical colloidal crystal within a mold [13].

2.3 Electrodeposition

Electrodeposition is the most common method for surface modification to alter the material property. The process is carried out with two- or three-electrodes arrangement under an applied voltage. Moreover, the overpotential to drive the electroplating can be estimated via the Nearnst equation, and the amount of deposits can be calculated by Faraday's law [42]. In electrodeposition, variables like pH value, ion concentration, temperature, and additives are usually adjusted and studied to achieve bottom-up fabrications. Likewise, to fill the void in colloidal crystals, the electrodeposition has been carried out in potentiostatic [23] or galvanostatic [43] modes. Au [44], Pt [45], Ag [44], Pd [45], Co [45], and Ni [17, 23, 46-50] inverse opals were recently fabricated through a potentiostatic electrodeposition. Because of the layer structure of colloidal crystals, the current response revealed an oscillation with deposition time, as shown in Fig. 2.10.

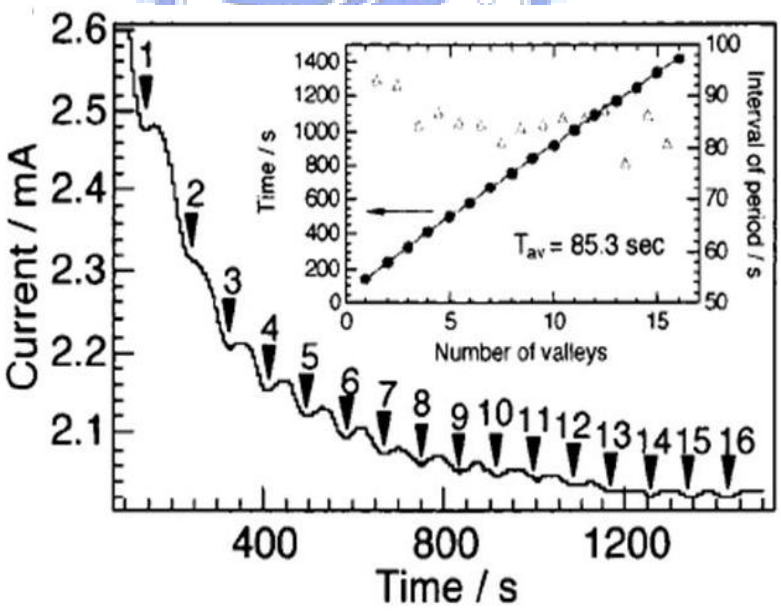

Figure 2.10 Time dependence of current in fabrication of inverse opals by electrodeposition. The numbered arrows indicate the valleys of current. Inset shows the times when the valleys appeared (●) and the intervals between each valley (△) [50].

Chapter 3

Experimental

This chapter introduces a facile process to prepare high quality colloidal crystals on planar and rod-like substrates through electrophoretic depositons (EPD). In addition, nickel inverse-opals were fabricated via nickel electrodeposition (NED) in the colloidal crystals. As shown in Figure 3.1, the EPD process can fabricate ordered arrays of PS microspheres in a desirable three-dimensional pattern, while the NED can successfully convert the periodic structure into an inverse one after dissolving the PS templates. Lastly, the as-prepared samples were characterized by various instrument to determine their electrical and optical properties. Figure 3.2 provides the flow chart for the sample preparation steps involved.

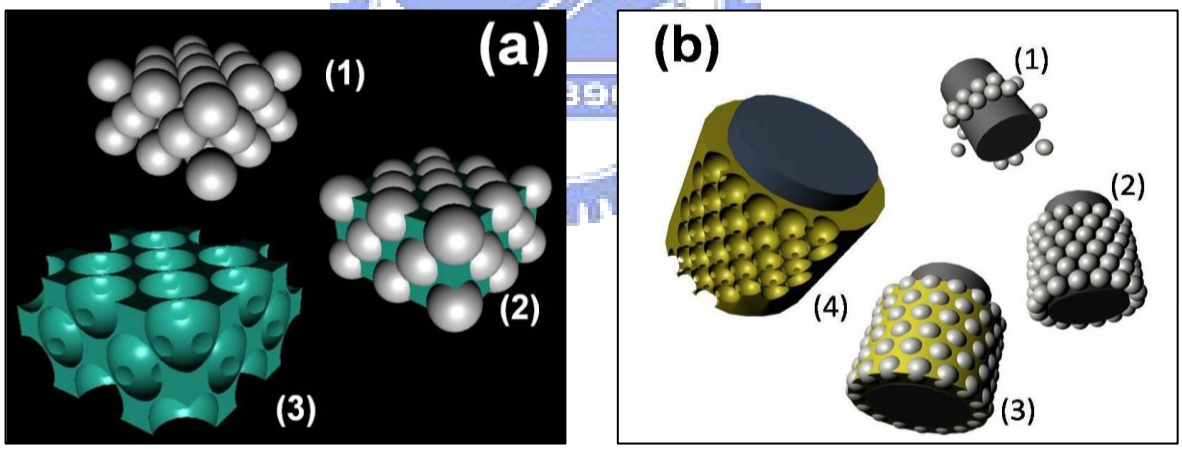

Figure 3.1 Schematic diagrams for fabrication of (a) planar and (b) cylindrical inverse opals.

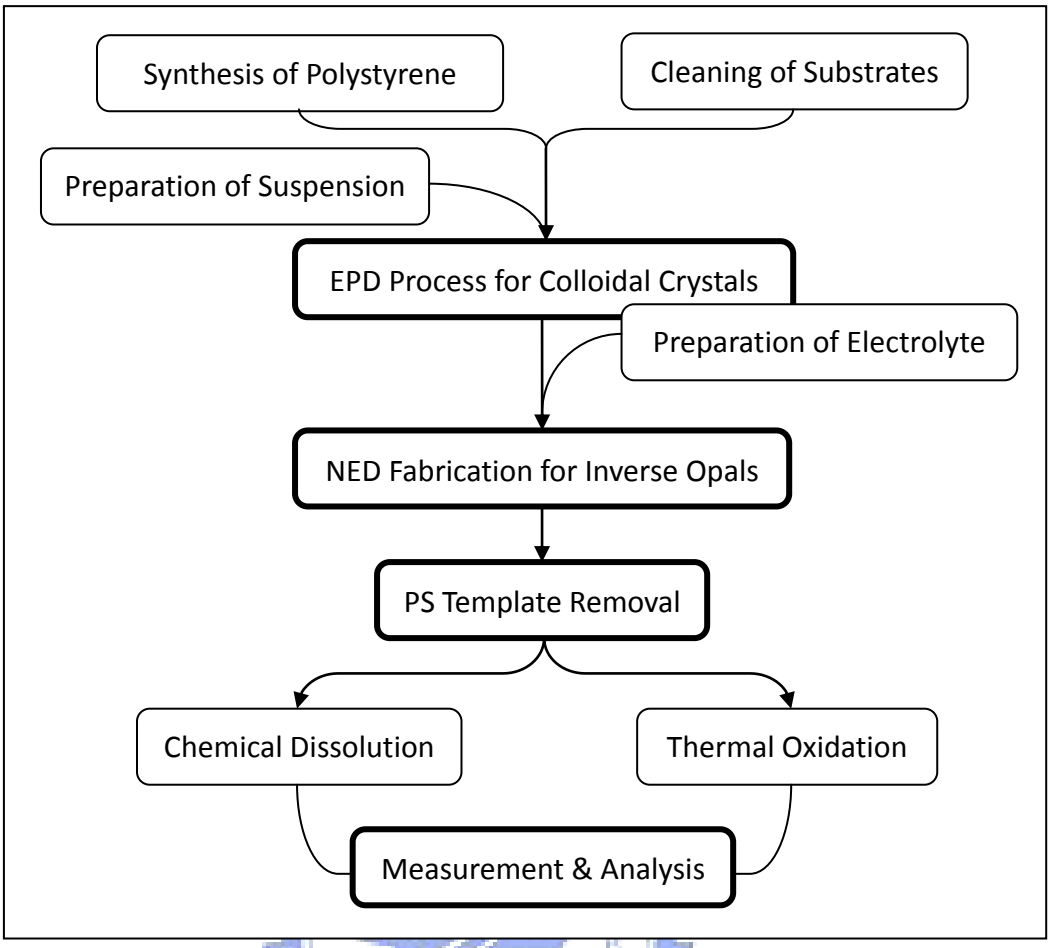

Figure 3.2 Flow chart for the experimental steps involved in this research work.

3.1 Materials

3.1.1 Synthesis of Polystyrene Microspheres

PS microspheres with diameter of 460 and 660 nm were synthesized via an emulsifier-free emulsion polymerization process. Styrene was served as the monomer after removing inhibitors and $K_2S_2O_8$ was used as the initiator. A minute amount (0.5 g/L) of sodium bicarbonate was added in preparation of 460 nm PS. The polymerizations took place at 75℃ under a nitrogen atmosphere for 18 hrs. Afterward, the colloidal suspension was diluted with deionized (DI) water and filtrated through a filter paper (ADVANTEC 5C 110 mm) with a mechanical pump in order to remove remaining monomers. Mono-disperse PS microspheres were later collected from the filter and suspended in DI water. After evaporation under 60 ℃ for 3 to 4 days, we were able to obtained dry PS powders.

3.1.2 Preparation of Suspensions

1g of 660 nm PS microspheres and 0.25 g of 460 nm ones were mixed respectively with 100 mL of 99.5 wt% ethanol to form stable suspensions, followed by ultrasonication and vigorous stirring for 5 hrs to reach a stable state. To adjust the properties of suspensions, PS microsphere concentration, pH value, and microsphere size were systematically controlled to stabilize those microspheres. In these suspensions, values for zeta-potential and electrophoretic mobility were -65.19 mV and -1.31×10^{-4} $cm^2V^{-1}s^{-1}$ for the PS 460 suspension, and -61.17 mV and -1.23×10^{-4} $cm^2V^{-1}s^{-1}$ for the 660 nm one. These values were recorded by a zeta-potential instrument (Malvern Zetasizer Nano Zs).

3.2 EPD for Colloidal Crystals

3.2.1 Pretreatment on Planar Substrates

ITO on glass (30×35 cm^2) purchased from Uni-Onward company with a sheet resistance of 7 ohm and 0.7 mm in thickness was used as a planar substrate in EPD process. Pieces of the ITO-glass (15×15 and 10×5 mm^2) were pre-cleaned with DI water and degreased in acetone under ultrasonication for 1 hr, followed by oven drying at 50 ℃. Then, they were treated with ethanol for 10 min at room temperature prior to the EPD process.

3.2.2 Fabrication of Planar Colloidal Crystals

Two electrodes were arranged vertically at a distance of 10 mm for the EPD process, as shown in Fig. 3.3. They were stainless steel plate (counter electrode) and ITO-glass piece (working electrode). A voltage of 10 V was applied for 10~60 min to reach desirable colloid thickness. Upon finished, the samples were carefully removed from the suspension, followed by a controlled drying at 20 ℃ for 30 min. This is to avoid unnecessary evaporation that might alter the colloidal crystal structure.

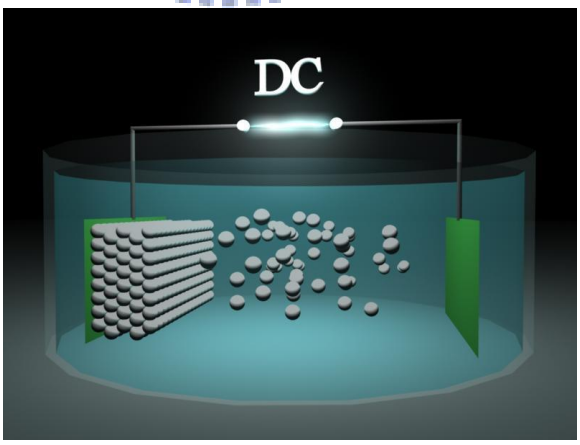

Figure 3.3 A schematic diagram of experimental setting for the planar EPD process.

3.2.3 Preparation of Circular Electrodes

Individual carbon fibers (CFs) with 7 μm in diameter were first carefully separated from a

bunch of CFs (TORAYCA-T300). Then, they were pre-cleaned with DI water and degreased in acetone under ultrasonication. Subsequently, a segment of copper tape with silver colloidal gel was employed as a conductive cladding to fix the CF. Afterward, the as-prepared sample was further heated in oven at 50 ℃ to achieve complete dehydration. Next, the sample was cut into length of 1.5 cm to proceed EPD.

3.2.4 Fabrication of Cylindrical Colloidal Crystals

The EPD was carried out with two electrodes arranged vertically in a co-axial configuration. An as-prepared CF sample was immersed into the suspension at 1 cm depth. A stainless steel (A304) in circular shape was used as the counter electrode, as presented in Fig. 3.4.

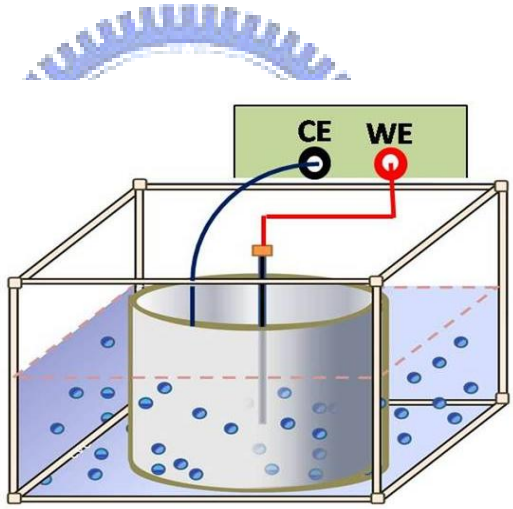

Figure 3.4 A schematic diagram of experimental setup for the cylindrical EPD process.

A voltage of 10 V was applied to drive the EPD, and the distance between the counter and working electrodes was 2.3 cm. The assembly process lasted 0-60 min. When finished, samples of CCC were removed and kept at 20 ℃ for 10~20 min to evaporate ethanol slowly. At this stage, the dark surface of CF was covered in a white cloak with an obvious light diffracting character, which can be observed via an optical microscope easily.

3.3 NED for Inverse Opals

3.3.1 Preparation of Electrolyte

The electrolyte for the nickel electrodeposition included $NiSO_4 \cdot 6H_2O$ (130 gL^{-1}), $NiCl_2 \cdot 6H_2O$ (30 gL^{-1}), H_3BO_3 (18 gL^{-1}), and H_2O_2 (3 mLL^{-1}). A minute amount of H_2SO_4 and NaOH were added to adjust the pH value of the electrolyte. In addition, the solution was stirred for 1 day before electroplating, and raised to 45℃ prior to the NED process.

3.3.2 Fabrication of Inverse Opals

To fabricate Ni inverse opals, planar and CF substrates underwent similar EPD process in different PS suspensions with various processing variables. Before the electrodeposition, samples were immersed in the plating electrolyte with moderate stirring for 1 hr, and a hotplate coupled with a thermal couple was employed to control the temperature of the system. Next, the electrodeposition was carried out on EPD-derived colloidal crystals under an applied voltage of 1 V at 45 ℃ in electrolyte of pH 5.2. Upon finished, the samples were cleaned with DI water and dehydrated in oven at 50 ℃ for 1 hr. Table 3.1 provides relevant processing variables in the fabrication process. Current output was recorded with a Keithley 2400 during the NED process.

Table 3.1 EPD parameters of samples for sequent NED process.

Particle Size	**PS-460**		**PS-660**	
Concentration	2.5 gL^{-1}		10 gL^{-1}	
Shape	Planar	Cylindrical	Planar	Cylindrical
Substrate Size	5×5 mm^2	7×10^{-2} π-mm^2	15×15 mm^2	7×10^{-2} π-mm^2
Electric Field/ Applied Voltage	15 V/cm	10 V	10 V/cm	10 V
EPD Time	7.5 min	30 sec	30 min	45 sec

3.4 Removal of Polystyrene Template

3.4.1 Chemical Dissolution

PS microspheres after the NED process were carefully etched away by immersing the samples in an ethyl acetate (95 wt%) solution. The color for the sample would immediately change from white to purple/red as the solution percolated throughout the structure, making a larger contrast in the refractive index. After 2 days, the remaining Ni skeleton was cleaned with ethanol several times until the odor of ethyl acetate was removed. At this stage, we successfully made the Ni inverse opals.

3.4.2 Thermal Oxidation

PS microspheres were directly removed by a thermal oxidation treatment at temperatures of 250 ℃, 350 ℃, and 450 ℃ for 2 days. It is noted that the T_g (glass transition temperature) and T_m (melting point) of PS are 95 ℃ and 240 ℃, respectively. Upon finished, the samples were kept in oven for furnace cooling in order to avoid undesirable thermal distortion of the inverse structure.

3.5 Instrument

3.5.1 Morphological Observation

Scanning Electron Microscope (SEM)

A SEM (JEOL-LSM-6700) was employed to observe relevant morphologies for colloidal crystals and inverse opals. In SEM sample preparation, the specimens were mounted on a copper holder, while sputtering of Pt was carried out at 20 mA for 90 sec (for insulating samples) or 40 sec (for conductive samples). Afterward, the SEM specimens were maintained under a pressure of 9.63×10^{-5} Pa, and observed with an acceleration voltage of 15 kV and an emission current of 10 μA.

Optical Microscope (OM)

With light incidence directly normal to the sample surface, the OM (Olympus CX41) was used to observe the light diffracting from cylindrical colloidal crystals. The images were captured by a coupled digital CCD camera (CY-100A).

3.5.2 Characterizations

Energy Dispersive X-ray (EDX)

EDX attached on a SEM was used to perform the semi-quantatative composition report and elemental mapping for the inverse opals.

High Resolution X-ray Diffractometer (HRXRD)

A HRXRD (Bede D1) was used to determine the crystallinity and relevant composition for the nickel inverse opals before and after thermal treatments.

Four-Point Measurement (4pp)

To measure the electrical properties, a four-point measurement was carried out by a

Keithaley 4200 to obtain the conductivity for the planar nickel inverse opals. For cylindrical nickel inverse opals, samples were fixed on a non-conductive glass with two silver bumps serving as the probe contact points, and a forward bias of 0~400 mV was applied during the measurement.

UV-Vis-IR Spectrum

Optical response for the colloidal crystals and their inverse opals were acquired through a Fourier Transform Infrared (FTIR) microscope (Hyperion 2000, Bruker) in a nitrogen atmosphere. During the measurement, the samples were illuminated with a selective light source (CaF_2), and the reflectance was obtained by normalizing the measured signals detected from the samples to that from a flat aluminum mirror.

Chapter 4

Results and Discussion on EPD Process

This chapter provides the results and discussion on fabrications of colloidal crystals by the EPD in various processing parameters. Variables under studies were suspension concentration, applied electric field, and deposition time. In general, the deposit weight from an EPD process is expressed in equation 4.1 and 4.2 for planar and cylindrical cases, respectively [11];

$$Y = \frac{2}{3} C_s \cdot S \cdot \varepsilon \cdot \xi \cdot \left(\frac{1}{\eta}\right) \cdot \left(\frac{V}{L}\right) \cdot t \qquad \text{[eq. 4.1]}$$

$$Y = \frac{lVC_s \varepsilon \xi t}{3ln(a/b)\eta} \qquad \text{[eq. 4.2]}$$

In equation [4.1], ***Y*** is the deposited weight of EPD layer, $\boldsymbol{C_s}$ is the mass concentration of PS microspheres in suspension, ***S*** is the area of substrate, $\boldsymbol{\varepsilon}$ and $\boldsymbol{\xi}$ are the dielectric constant and zeta potential of PS microspheres, $\boldsymbol{\eta}$ is the viscosity of solvent in suspension, ***V*** is the applied voltage, ***L*** is the distance between working and counter electrodes, and ***t*** is the deposition time. In equation [4.2], there are three more variables in cylindrical EPD system; ***l*** and ***a*** are the length and radius of the working electrode, and ***b*** is the radius for the coaxial counter electrode (***b*** > ***a***). In this work, suspensions made of 460 and 660 nm PS microspheres (**PS-460** and **PS-660**) were prepared in different C_s and examined to achieve a smooth EPD coating. By driving the EPD process with suitable applied voltage (electric field), the planar and cylindrical colloidal crystals (**PCC-460/660** and **CCC-460/660**) were successfully fabricated. The following sections provide detailed discussion on individual variables and their effects on the quality of colloidal crystals.

4.1 Suspensions and Substrates

The as-synthesized PS microspheres are demonstrated in Fig. 4.1. The larger ones exhibited a diameter of 660 nm with a standard deviation of 16.4 nm while the smaller ones revealed a diameter of 460 nm with a standard deviation of 10.1 nm. Assembly of PS microspheres could be easily achieved simply by solvent evaporation. As shown, we obtained reasonable uniformity in size distribution and this attribute was critical for our EPD process. The PS microspheres were further mixed with ethanol to prepare the suspensions, PS-460 and PS-660.

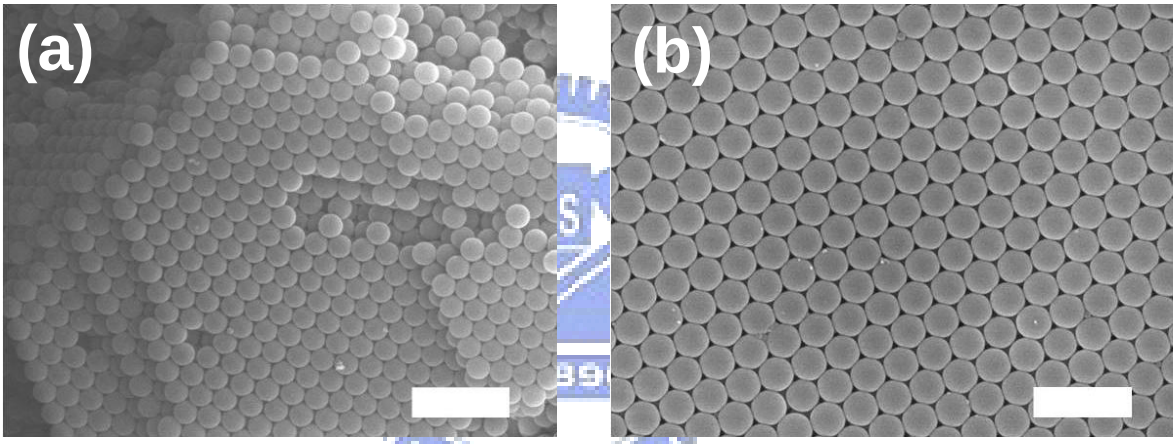

Figure 4.1 SEM images of PS microspheres with diameter of (a) 460 nm and (b) 660 nm. The scale bars are 2 μm.

Figure 4.2 presents the plots of electrophoretic mobility in PS-460 and PS-660. Their concentrations were 2.5 g/L and 10 g/L, respectively. The mobility for the PS microspheres in each suspension appeared in a single peak with corresponding zeta-potential was above 60 mV. Both results suggested that our suspensions were in excellent stability and the size of PS microspheres was reasonably mono-dispersive.

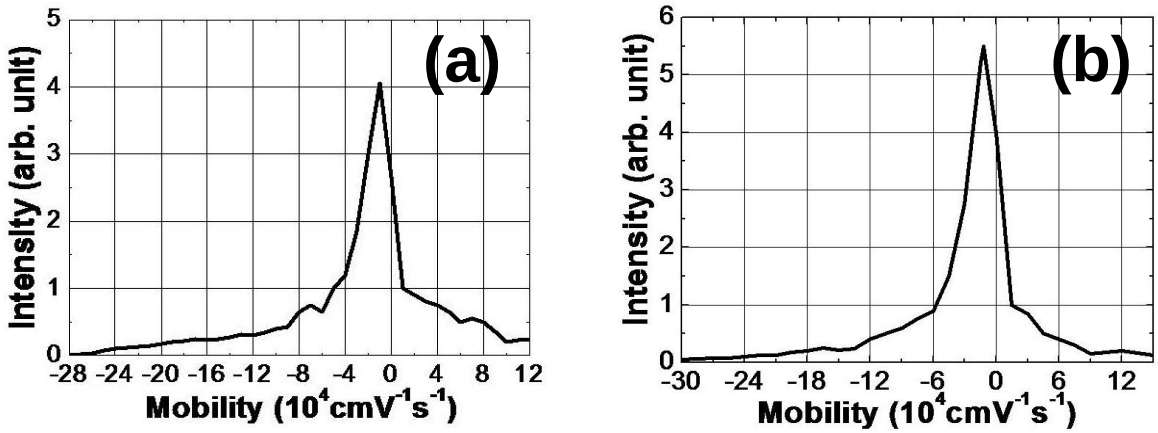

Figure 4.2 Electrophoretic mobility of suspension (a) PS-460 and (b) PS-660.

4.1.1 Microsphere Concentration in Suspensions

While the PS microspheres were driven to deposit on the substrate from bulk suspension, it took some time to assemble them into a desirable close-packed arrangement. It is necessary for the first layer to be close-packed before the second layer can be deposited. Therefore, a reduced deposition rate was considered critical in fabricating high-quality colloidal crystals. After rearranging those variables in equation 4.1, we could derive that the C_s is proportional to the deposition rate (Y/t). Thus, the C_s plays significant influence over the quality of the colloidal crystals.

Figure 4.3 presents the SEM images of EPD layers fabricated in PS-460 with C_s of 10 g/L and 2.5 g/L under 10 V/cm. As clearly shown in Fig. 4.3(a), the PS microspheres were in random arrangement with approximate domain size in 2~3 μm. In addition, a number of voids was observed among particles. When we reduced the PS microsphere concentration to 2.5 g/L, the domain of colloidal crystals became larger, as exhibited in Fig 4.3(b). These behaviors suggested that the EPD fabrication with an excess C_s could not deliver high-quality colloidal crystals. Moreover, increase in the C_s enhanced the volume fraction of PS microspheres, which raised op the viscosity of suspension and zeta potential. Thus, a larger C_s not only rendered a faster deposition rate but also affected the Brownian motion among individual microspheres.

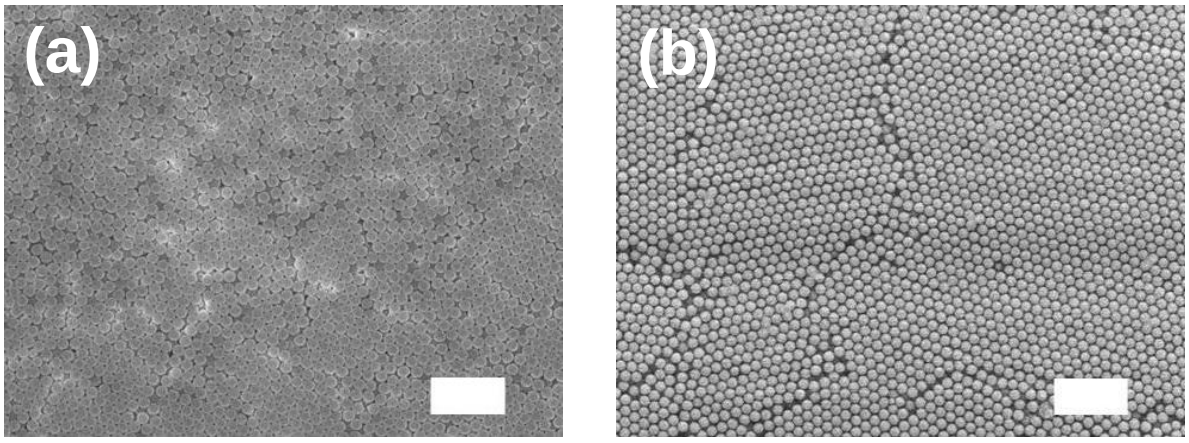

Figure 4.3 SEM images of EPD layers prepared in PS-460 with various microsphere concentrations of (a) 10 g/L and (b) 2.5 g/L. The electrical field was fixed at 10 V/cm for 3 min. The scale bars are 3 μm.

Identical experiments were also performed in PS-660 suspensions, with their results presented in Fig. 4.4. Similarly, the suspension of 10 g/L demonstrated a better quality in colloidal crystals over 25 g/L one. However, this great difference in the optimized PS microsphere concentration between PS-460 and PS-660 suspension was resulted from their distinct volume fraction.

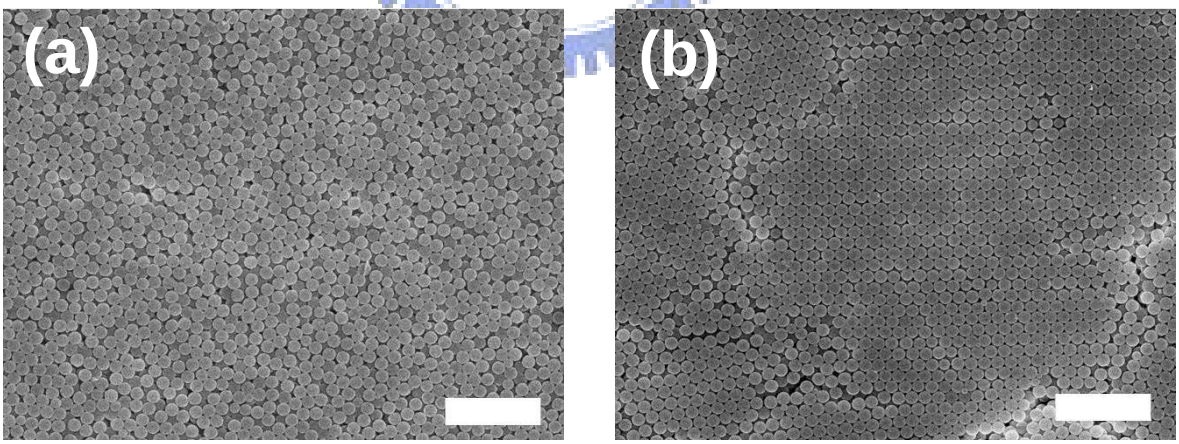

Figure 4.4 SEM images of EPD layer made in PS-660 with microsphere concentrations of (a) 25 g/L and (b) 10 g/L. The electrical field was fixed at 10 V/cm for 10 min. The scale bars are 5 μm.

To achieve identical volume fraction, the concentrations ratio for the PS-460 to PS-660 should be kept at about 0.3:1 (g/L), which was close to 2.5:10 in our experiments. Besides,

the values for electrophoretic mobility in PS-460 (2.5 g/L) and PS-660 (10 g/L) were almost the same, as shown in Fig. 4.2. This suggested that the stability of suspension was more relevant to the volume fraction but not mass fraction. Therefore, in following experiments we chose the 2.5 g/L of PS-460 and 10 g/L of PS-660 to fabricate colloidal crystals.

4.1.2 Shape of Substrates

Figure 4.5 exhibits the SEM images of EPD layers on planar ITO glass and carbon fiber prepared under 10 V in 0.25 g/L PS-460. The EPD layer on the ITO glass revealed a (111) plane in FCC lattice. In contrast, a defective structure was observed in the EPD layer on CF. We surmised that linear defects and curved surface of the CF might convert the state of arrangement from close-packed structure into a non-close-packed one. In the insets of Fig. 4.5, the thickness of ITO layer was 200 nm, and the diameter of CF was about 7 μm. In cylindrical case, the diameter size of the CF (7 μm) was only 10~15 times larger than that of PS microspheres (460 nm and 660 nm). Namely, EPD process was carried out on this curved surface (CF) with PS microspheres assembly, leading to a disordered EPD layer.

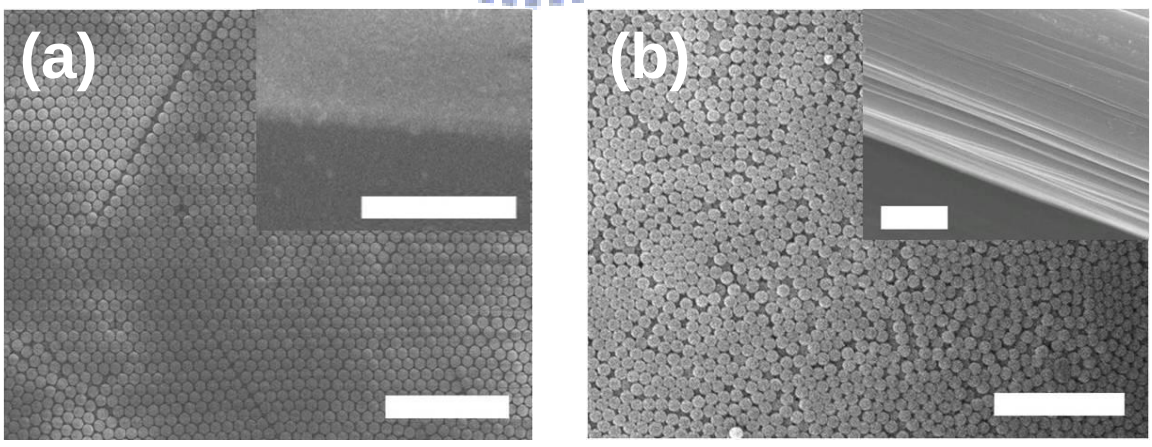

Figure 4.5 SEM images of EPD layer on (a) ITO glass and (b) carbon fiber. The insets provide the SEM images of each substrate. The scale bars are 5 μm in the figure and 2 μm in the inset.

4.2 Fabrication of Planar Colloidal Crystals (PCCs)

4.2.1 Electric Field in EPD process

Figure 4.6 provides the thickness of PCC-660 made of various electric fields for 15 min on ITO glasses. The deposit thickness was linearly increased when the electric field was larger than 10 V/cm. However, a reduced deposition rate was present at 5 V/cm, which suggested that there was a transition regime for EPD rate between 5 V/cm and 10 V/cm.

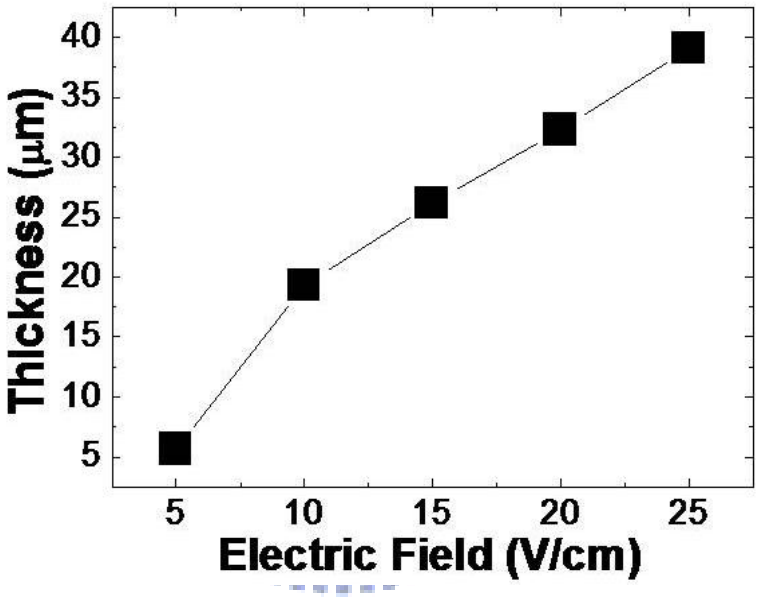

Figure 4.6 Thickness versus electric field for the colloidal crystals made of PS-660. The EPD fabrication time was 15 min.

Figure 4.7 displays the SEM images for the colloidal crystals from 5 V/cm, 10 V/cm, and 20 V/cm, respectively. The PS microspheres were in close-pack structure at 5 V/cm, and became disordered as the applied electric field was increased. This suggested a larger driving force would engender a defective assembly. It is also known that a large electric field might shorten the fabrication time, albeit with a compromised crystals quality. Therefore, the electric field of 10 V/cm was chosen for the EPD fabrication in PS-660.

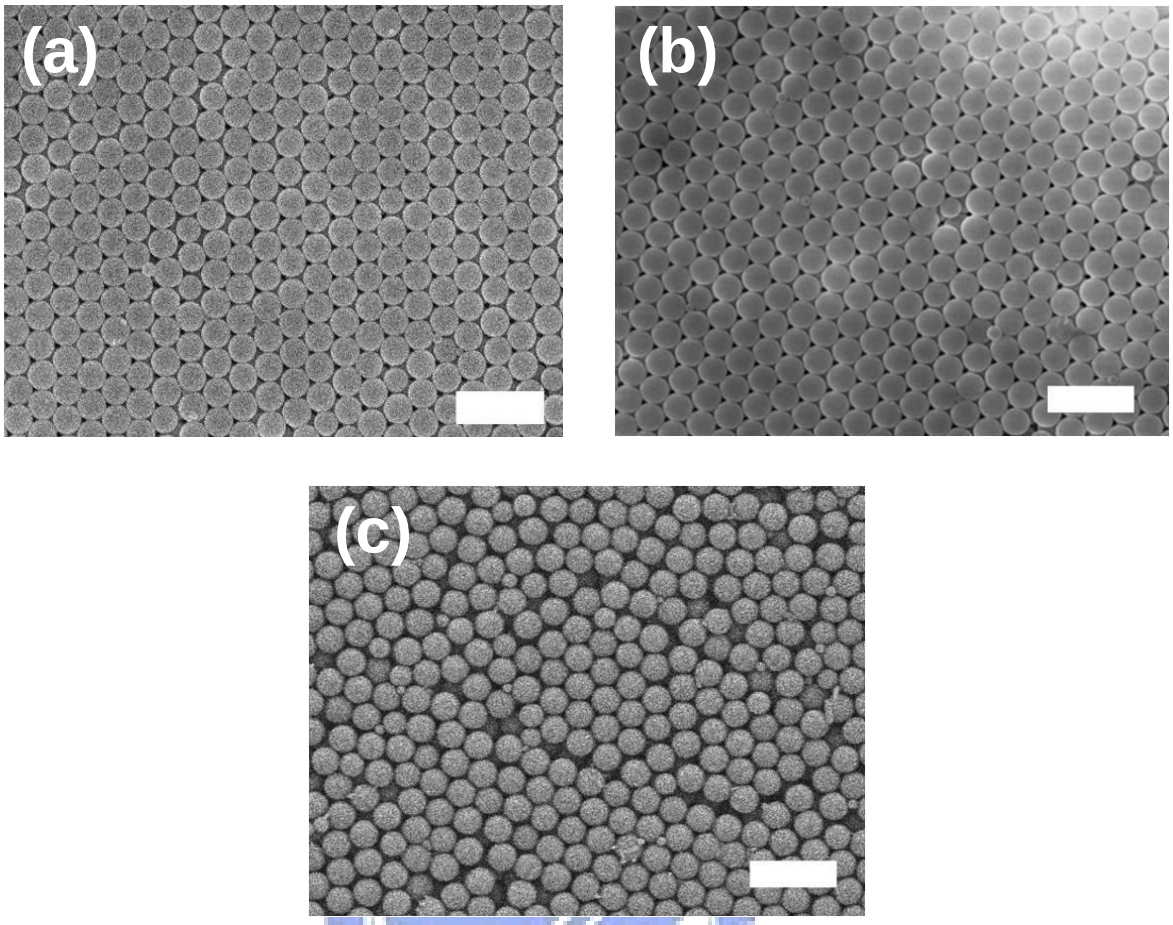

Figure 4.7 SEM images of PCC-660s fabricated in PS-660 under (a) 5 V/cm, (b) 10 V/cm, and (c) 20 V/cm for 15 min. The scale bars are 2 μm.

The thickness of EPD layer as a function of electric field using the 460 nm microspheres is displayed in Fig. 4.8. It was observed that the thickness of PCC-460 was linearly increased with the electric field. Figure 4.9 provides the SEM images for the samples made of 10 V/cm, 15 V/cm, and 25 V/cm, respectively. As expected, a larger electric field rendered a relatively disordered structure. Therefore, to improve the quality of PCCs, the electric field should be moderately reduced. Hence, we selected 15 V/cm in the EPD process using PS-460. Figure 4.10 demonstrates the relationship between current density (j) and deposition time (t) under the selected electric fields in PS-660 and PS-460. Both j-t curves reveal a decreasing current density at extended deposition time. This behavior indicated that the PS microspheres were self-assembling on the ITO glass, producing a mask to shield the electrical field, a phenomenon commonly known as “screen effect”.

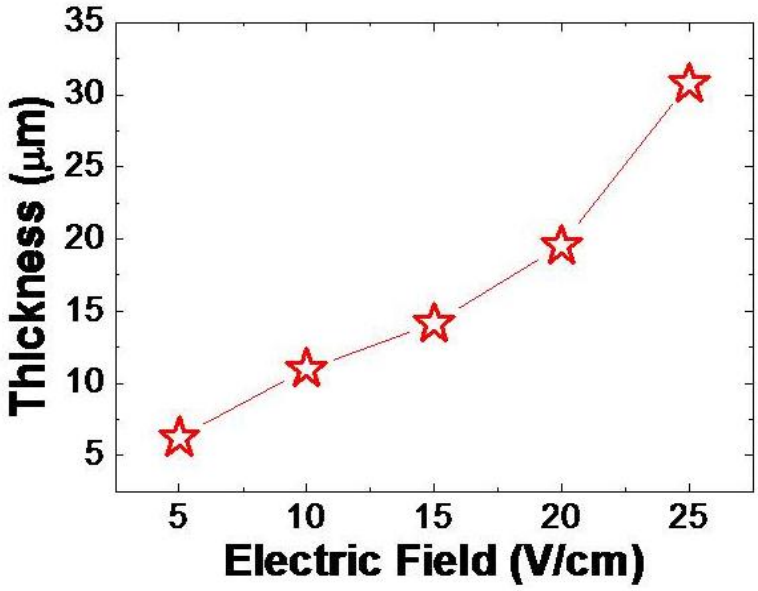

Figure 4.8 Thickness versus electric field for the colloidal crystals made of PS-460. The EPD fabrication time was 10 min.

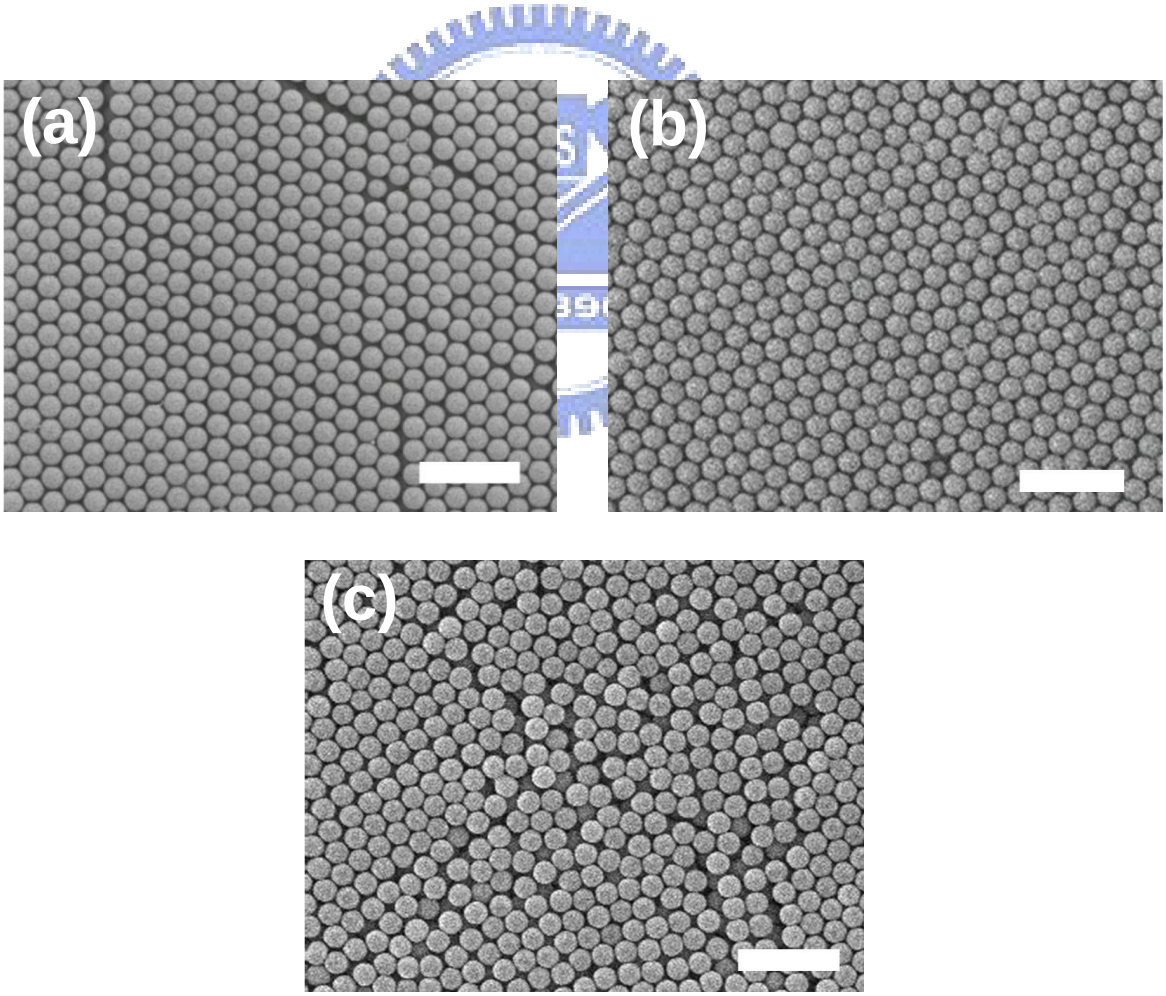

Figure 4.9 SEM images of PCC-460s on ITO glass fabricated under (a) 10 V/cm, (b) 15 V/cm, and (c) 20 V/cm for 15 min. The scale bars are 2 μm.

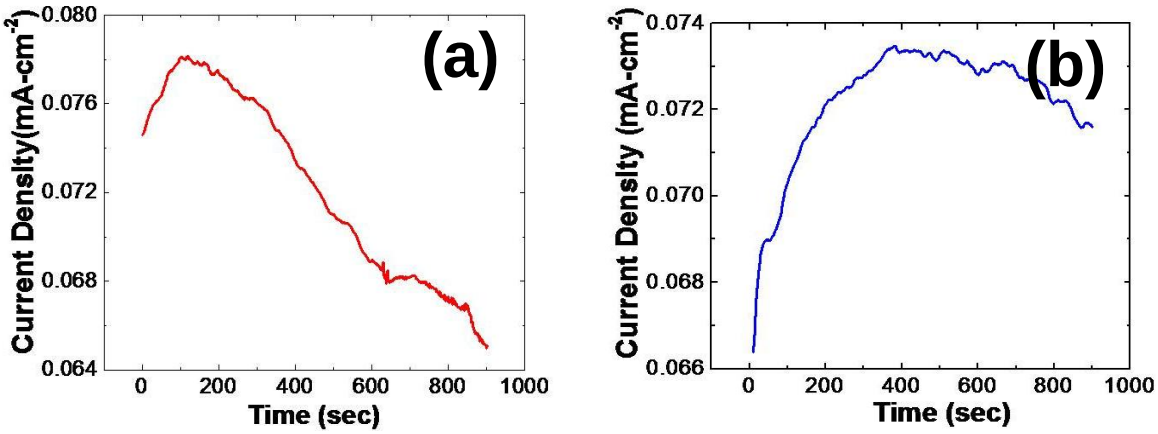

Figure 4.10 Evolution of current density vs. time during the EPD process under (a) 10 V/cm using PS-660 microspheres and (b) 15 V/cm using PS-460 microspheres.

4.2.2 Deposition Rate for Planar EPD

Figure 4.11 demonstrates the plot of thickness versus time for the samples prepared in the EPD process.

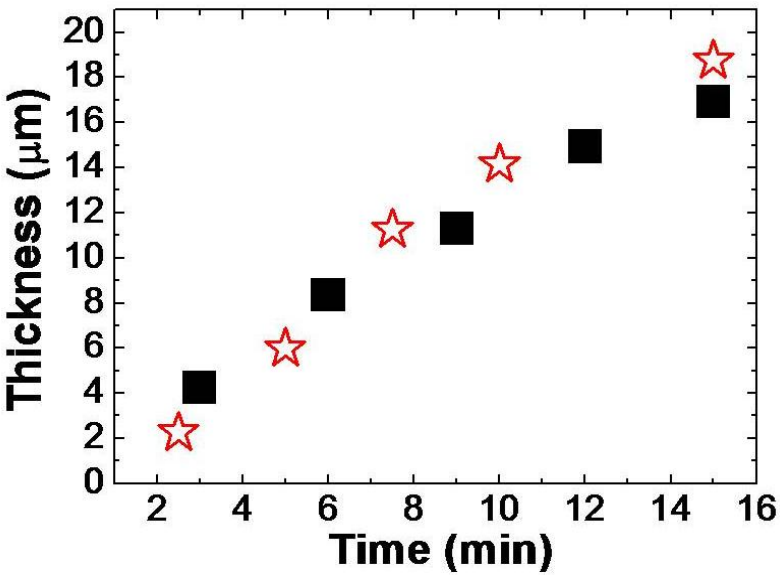

Figure 4.11 Thickness versus EPD time for the PCC-660 (■) and PCC-460 (☆). The applied electric field was 10 V/cm in PS-660 and 15 V/cm in PS-460.

The estimated deposition rates were 1.064 μm-min^{-1} and 1.337 μm-min^{-1} for the PCC-660 and PCC-460, respectively. As clearly shown, the growth of PCCs was slowing down with

the EPD time. We attributed this phenomenon to the decreasing electric field as the PS microspheres assembled on the substrate. Figure 4.12 and 4.13 exhibit the SEM images for the samples prepared in the EPD process with the optimized parameters. As expected, the microspheres were assembled properly to form colloidal crystals in multiple layers.

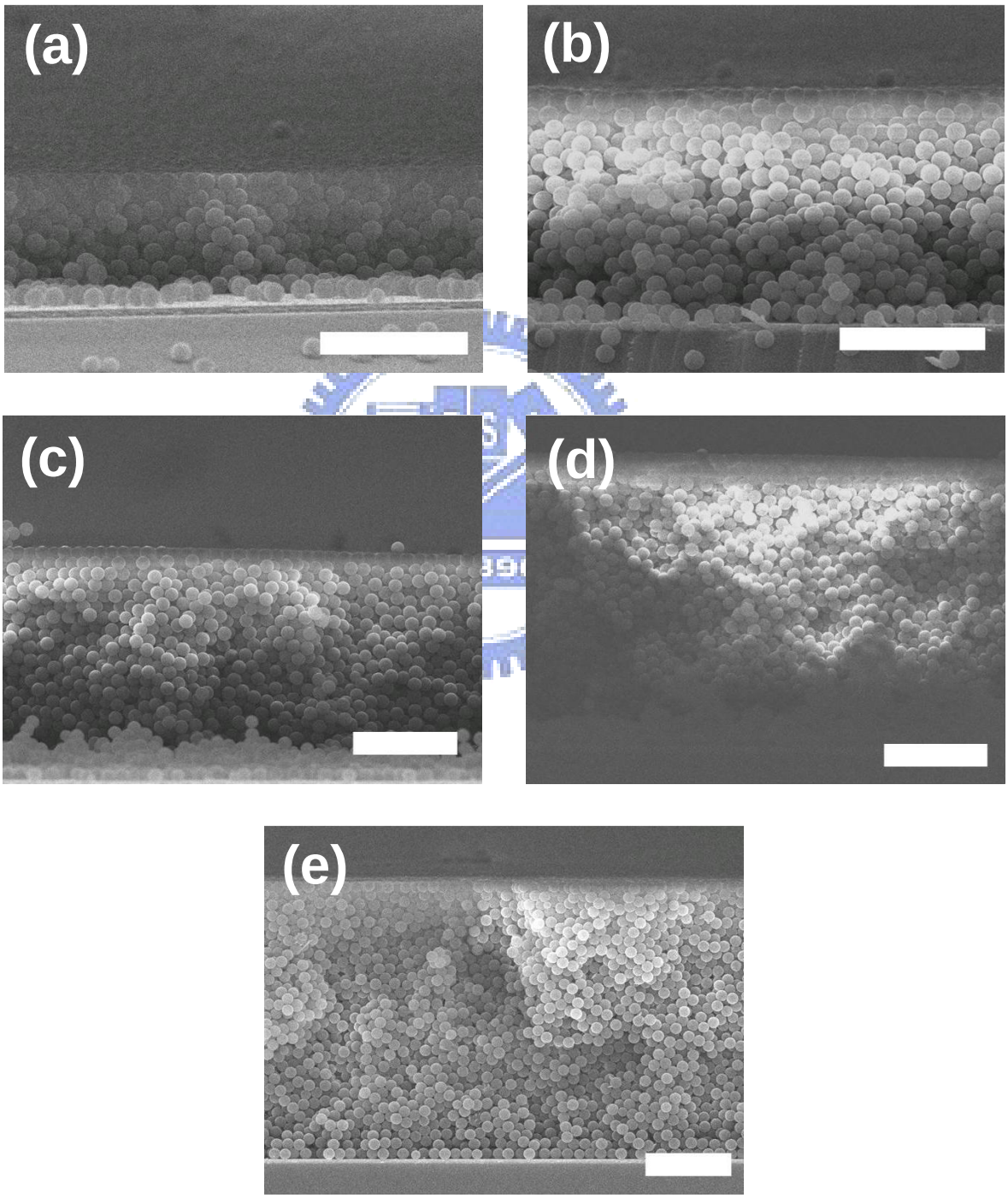

Figure 4.12 SEM images of PCC-660s fabricated under 10 V/cm for (a) 3, (b) 6, (c) 9, (d) 12, and (e) 15 min, respectively. All scale bars are 5 μm.

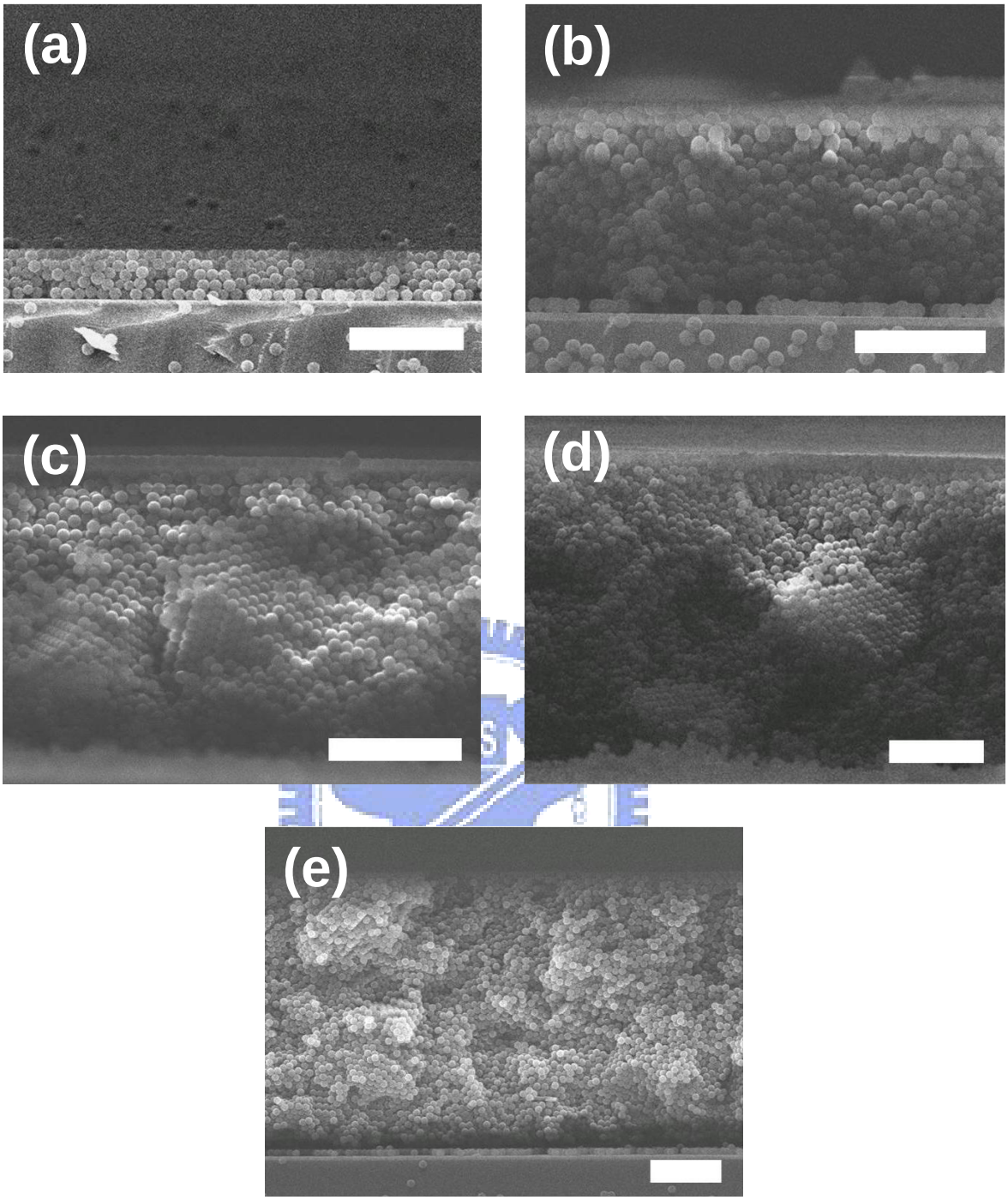

Figure 4.13 SEM images of PCC-460s fabricated under 10 V/cm for (a) 2.5, (b) 5, (c) 7.5, (d) 10, and (e) 15 min, respectively. All scale bars are 5 μm.

4.3 Fabrication of Cylindrical Colloidal Crystals (CCCs)

4.3.1 Applied Voltage in EPD Process

As shown in equation 4.2, the yield amount from the cylindrical EPD process was modified by additional three parameters, ***a***, ***b***, and ***l***, and it was further reduced by a constant about 8.79 (***ln(a/b)***) from that of planar EPD process. On the other hand, the applied voltage (***V***) was present in the equation as an independent parameter. Hence, we only controlled the voltage in the cylindrical EPD process.

Figure 4.14 display the SEM images of CCC-460s made from two different voltages in PS-660 for 30 sec. The morphology for the CCCs revealed a defective packed structure, which was resulted from the curved CF surface, as shown in Fig. 4.14(a). The diameter of CCC made of 5 V was about 9 μm, which was equal to 3 EPD layers. At this stage, the color of substrate remained dark, which can be easily observed by naked eyes.

In contrast, as shown in Fig. 4.14(b), the diameter of sample made of 10 V was about 60 μm, which was almost 30 layers. Because the size of CF was in micron range, its dimension was relatively small compared with the planar substrates. Therefore, under identical yield amount, the EPD layer prepared on the CF would be 10^3-10^4 times thicker as opposed to that of planar substrate. As a result, the effect of voltage during the EPD became extremely critical in the cylindrical case.

Figure 4.15 provides the diameter of CCCs under different applied voltages in the PS-460 and PS-660. Obviously, a voltage of 5 V was not able to deposit large amount PS microspheres in a short time, but 10 and 20 V were capable of delivering a much enhanced deposition rate for both PS-460 and PS-660 suspensions.

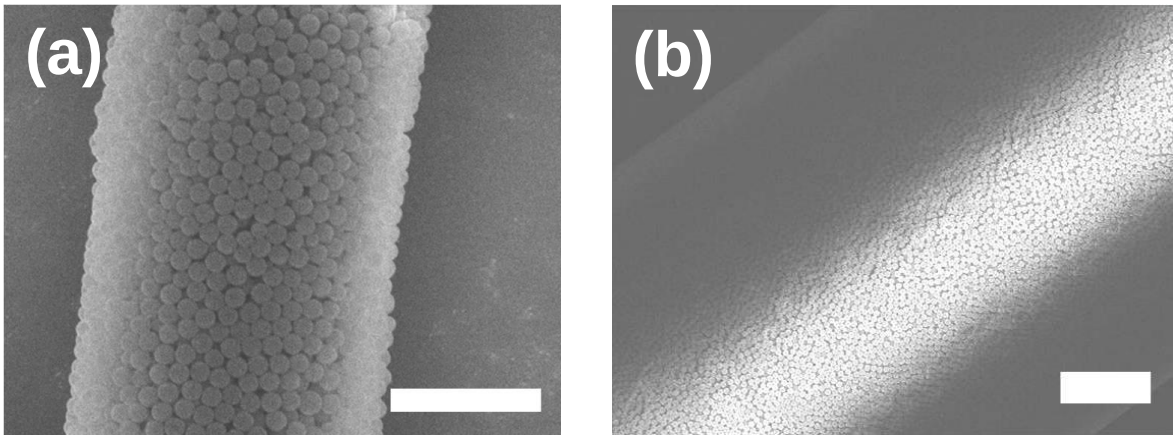

Figure 4.14 The SEM images of CCC-460s made of (a) 5 V, and (b) 10 V. The fabrication time was 30 sec. The scale bars are 5 μm in (a) and 10 μm in (b).

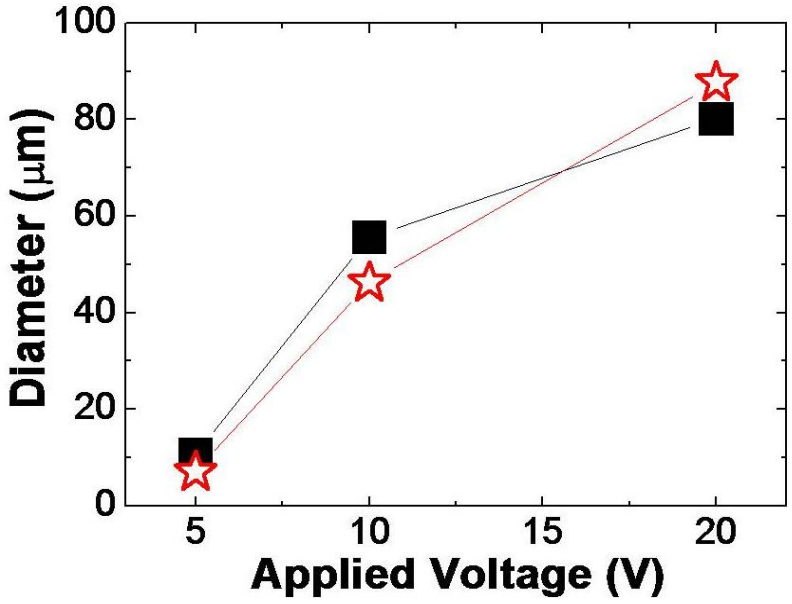

Figure 4.15 Diameter versus voltage for the CCC-460s (☆) and CCC-660s (■). Their fabrication time was 30 sec.

Figure 4.16 presents the SEM images of CCCs made of 10 V and 20 V by PS-660 and PS-460. Among them, the applied voltage of 20 V rendered a poor packing quality in the EPD layer because unnecessary larger EPD rate. In contrast, the 10 V exhibited a relatively dense packing in both suspensions. Because the diameter for the CCC-460 made of 10 V was much larger than that of CF, its fabrication could be approximated to a planar EPD case. Hence, the crystal quality of CCCs made of 10 V was still reasonable even the EPD rate of 10

V was much larger than that of 5 V. In addition, the CCC-460 revealed a better quality than that of 660 nm, as shown in Fig. 4.16(a) and Fig. 4.16(c). This suggested that the ratio of microsphere size to the diameter of substrate plays a critical role in desirable ordered arrangement. Hence, difference in the diameter for the CCCs indicated the importance of applied voltages. However, it was challenging to control the layer numbers with a large voltage because the deposition rate for the cylindrical EPD was taking place too fast.

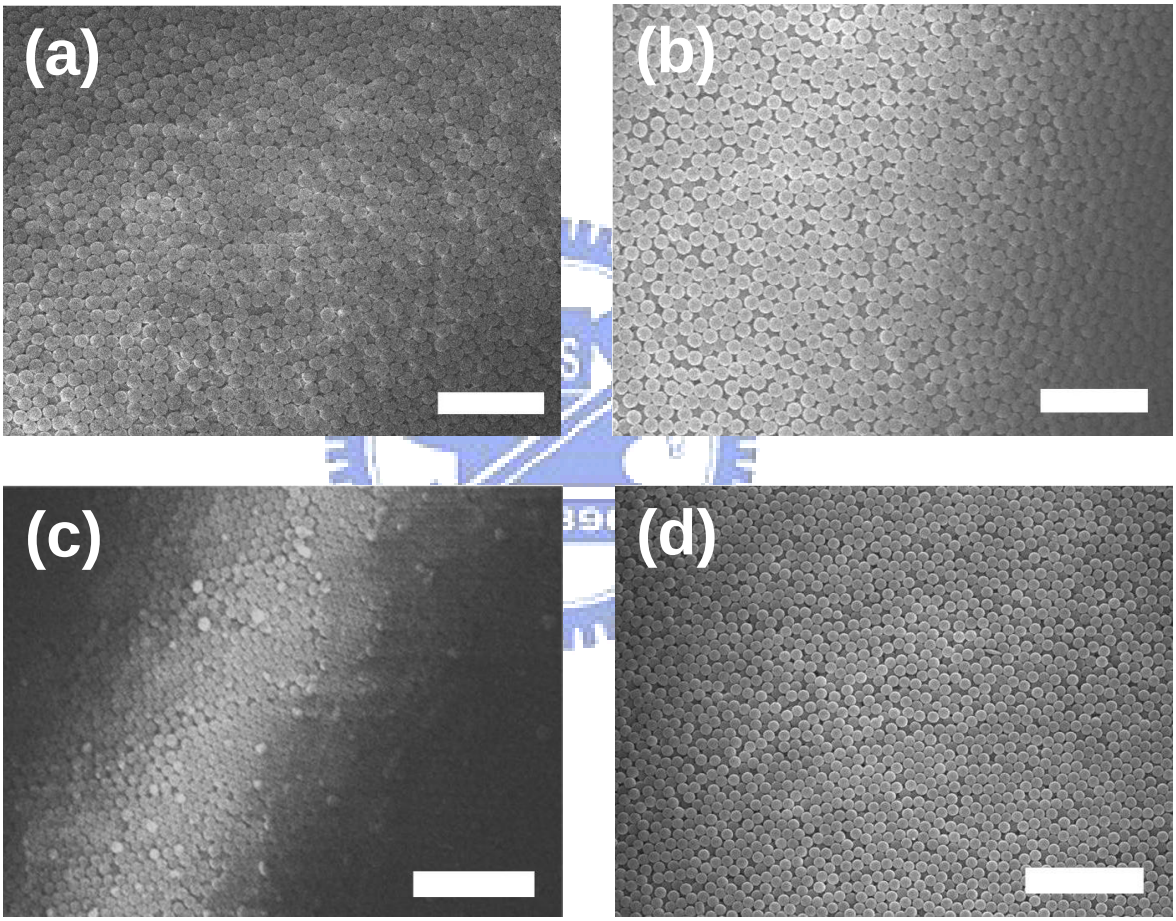

Figure 4.16 SEM images on the surface morphology of CCC-660 made of (a) 10 V and (b) 20 V, as well as CCC-460 made of (c) 10V and (d) 20V. The fabrication time was 30 sec, and the scale bars are 5 μm.

Figure 4.17 demonstrates the plots of current density versus time at voltage of 10 V. Both current values experienced a sudden jump, and reached a plateau afterwards. As the size of EPD layer was sufficiently large, the EPD process can be considered as a planar one,

and the self-assembling of PS microspheres was easy to be achieved. Hence, we selected the 10 V in following experiments

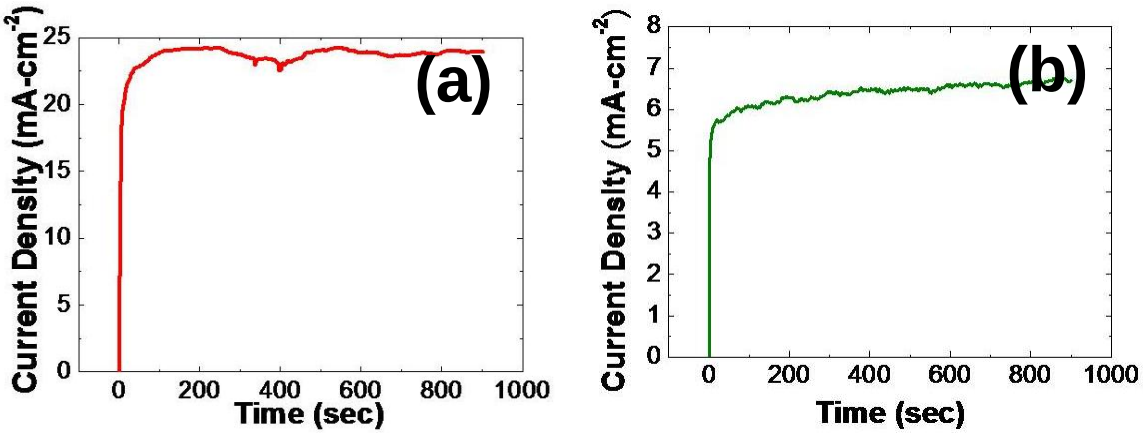

Figure 4.17 Time dependence of current density for (a) CCC-660 and (b) CCC-460 during cylindrical EPD process. The applied voltage was fixed at 10 V.

4.3.2 Deposition Rate for Cylindrical EPD

Figure 4.18 presents the plot of diameter versus time plots for the cylindrical colloidal crystals in the EPD process with PS-460 and PS-660. The diameter of CCC was linearly increased with deposition time, and a higher deposition rate was obtained in PS-440 than that in PS-660. Their respective deposition rates for the CCC-460 and CCC-660 were 0.322 μm-s^{-1} and 0.301 μm-s^{-1} intially, following by a slightly decrease to 0.201 μm-s^{-1} and 0.145 μm-s^{-1} after 6 min. These reduced rates indicated that those microspheres were arranged in proper packing order, reducing the pathway for the current on the substrate. According to the modified Hamaker's equation [51] for cylindrical EPD, the linear dependence indicated our experiment was still in the primary stage of EPD. This suggested that the deposits could be further thickened in a short time.

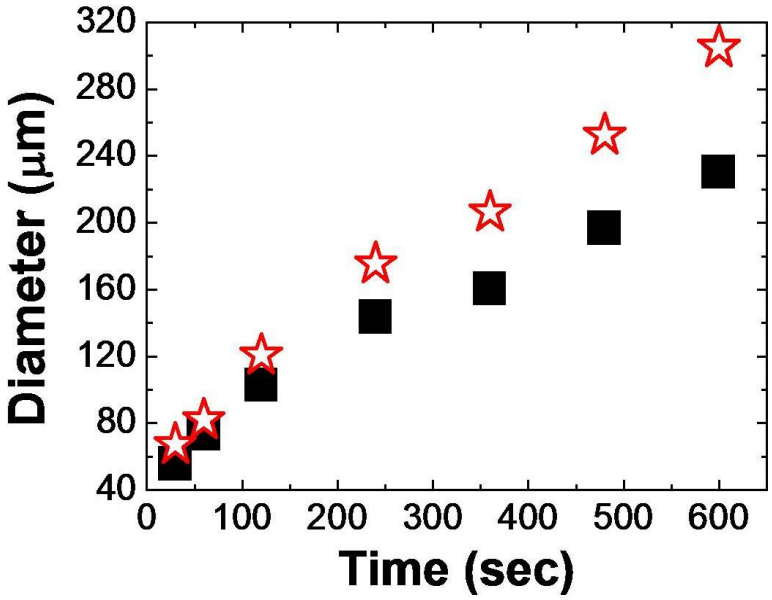

Figure 4.18 Diameter versus EPD time for the CCC-660 (■) and CCC-460 (☆) fabricated in suspensions under a voltage of 10 V.

Figure 4.19 displays the SEM images for the CCC-660 made of 10 V in PS-660 for different EPD time. Microspheres in size of 660 nm were not stacking well on the CF first, but ordered layers were observed later and became FCC (111) plane, as shown in Fig. 4.19(a) and 4.19(b). It suggested that as the diameter of CCCs increased, the disorder region could be compressed and became the grain boundaries distributed in the close packed structure. If the deposition time was further prolonged, there were some BCC grains obtained in the EPD layers, as exhibited in Fig. 4.19(c). This indicated that the most stable state was not present by self-assembly on the carbon fiber substrate. There might be two reasons to explain the appearance of planes such as FCC (100) and BCC (100).

The first plausible cause is the undesirable high EPD rate. It is known that the EPD rate increased with deposition time within 10 min. Hence, a higher EPD rate would raise the probability of EPD layers from a lower energy state to a higher energy one. The other explanation is the size incoherence. The diameter of CCC continued changing with the EPD time, and if the diameter of CCC was just a multiple of microsphere size, the microspheres tended to assemble in an ordered state on the same layer. Following this logic, the other

planes would reveal a non-close packed structure, or the BCC (100). This implied the EPD on a curved surface might be useful to achieve a defective packing structure. Figure 4.20 presents the SEM images of CCC-460 made of 10 V for various time in PS-460. Similarly, the size of ordered domains was becoming larger with the EPD time. However, the BCC plane was not found in the EPD layers.

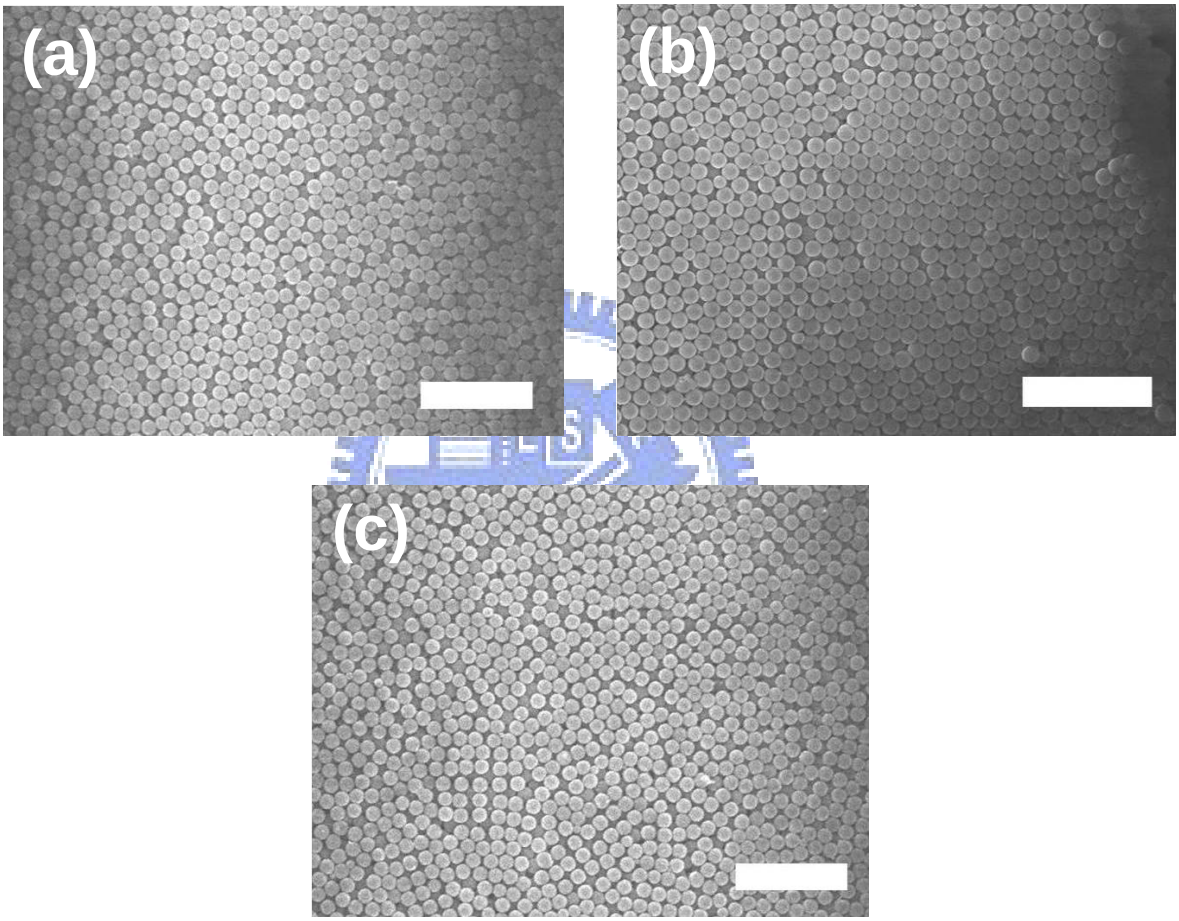

Figure 4.19 SEM images for the surface morphology of CCC-660s made of 10 V in PS-660 for (a) 2 min, (b) 4 min, and (c) 8 min, respectively. All scale bars are 5 μm.

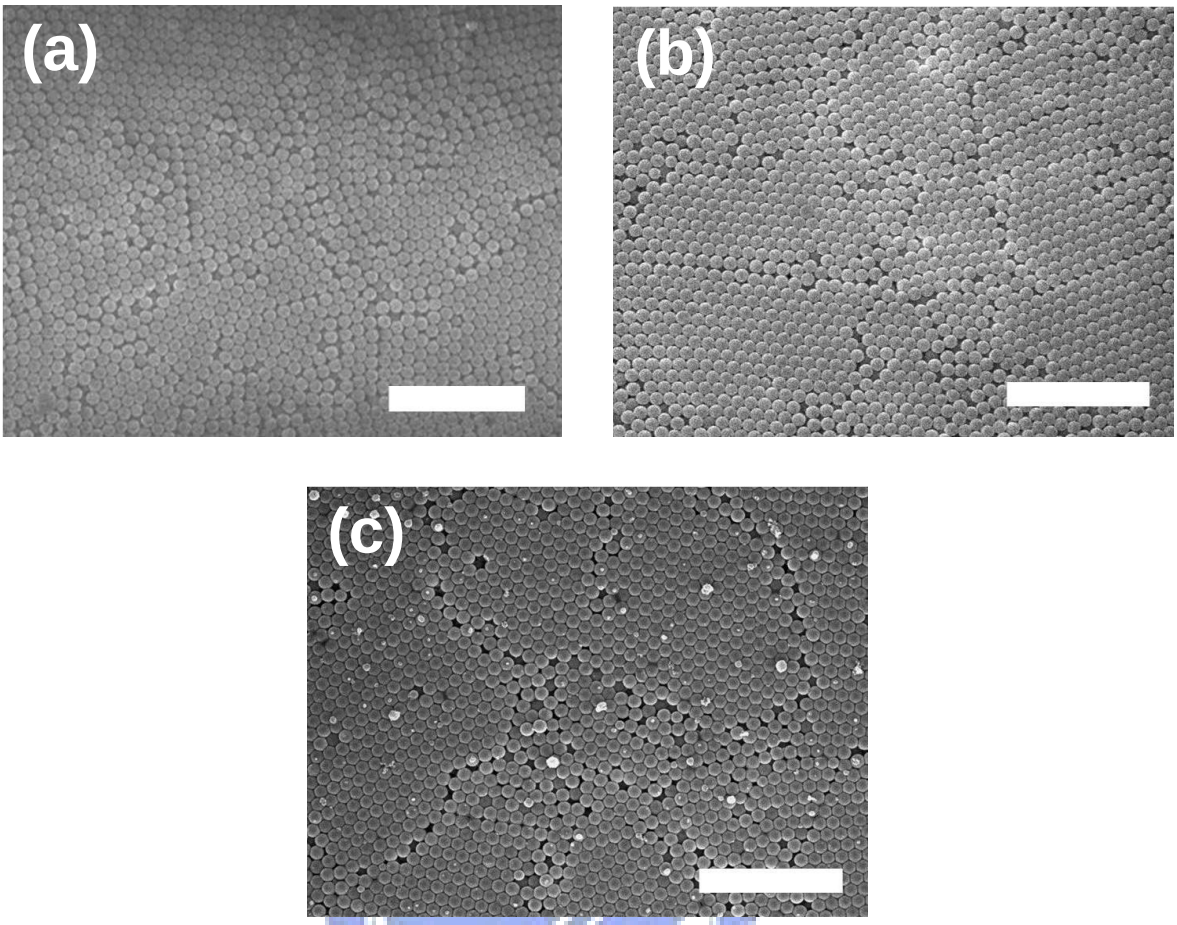

Figure 4.20 SEM images of the surface morphology of CCC-460s made of 10 V in PS-460 for (a) 2 min, (b) 4 min, and (c) 8 min. All scale bars are 5 μm.

Figure 4.21 presents the time dependence plot for the diameter of CCCs within 1 hr. From this figure, the increase in diameter of CCCs tended to reach a stable state after certain time. As pointed with arrows in the figure, a higher growth rate of CCCs was occurring after 30 min. The abnormal increase might be accidentally induced by “dip-coating” during sample removal.

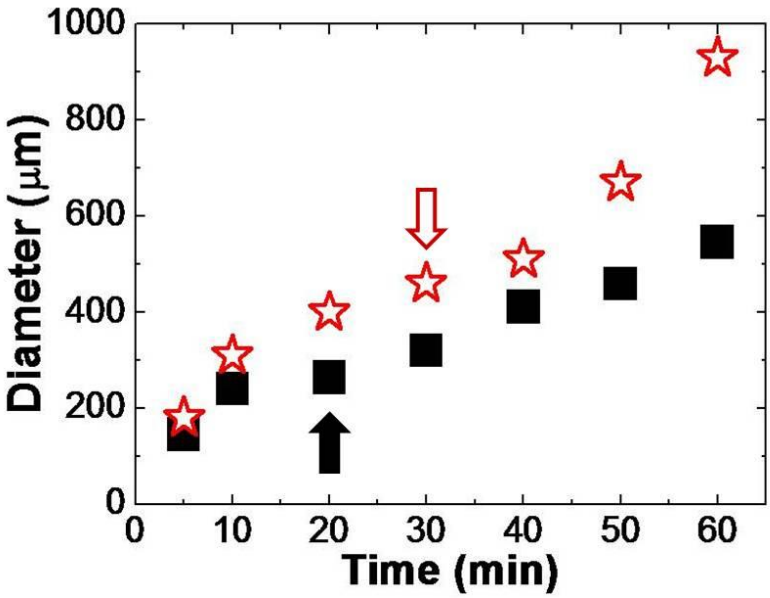

Figure 4.21 Diameter versus EPD time for the CCC-660 (■) and CCC-460 (☆) fabricated in suspensions under a voltage of 10 V.

Figure 4.22 and 4.23 present the photographs of CCCs taken by an optical microscope. Both CCC-460 and CCC-660 exhibited smooth surfaces along the longitudinal axis, and the diameter for each sample revealed rather impressive uniformity. Therefore, for every sample, a direct reflectance was observed in the middle of CCC, and its intensity was enhanced when its diameter was increased under identical light source.

In optical response, the CCC-460 displayed a set of light diffracting fringes as the EPD process was extended longer, as shown in Fig. 4.22. These diffracting lines demonstrated a distribution of the reflective light in illumination with various angles on FCC (111), and the wavelength of reflectance increased from substrate to the surface due to increasing lattice spacing. However, there is no obvious light reflecting when the CCC-660 was illuminated by a white light, as exhibited in Fig. 4.23(a) and 4.23(b). The self-arranged layer of PS-660 was essentially distorted by a curved substrate and the size incoherence between substrate and spheres, as well as those linear defects on the CF.

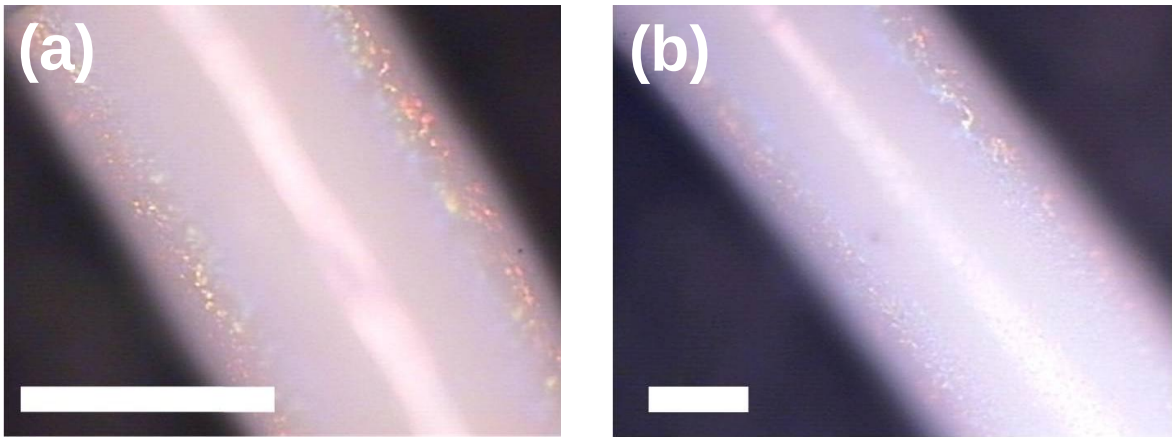

Figure 4.22 Optical microscopy images of CCC-460 self-assembled in PS-460 for (a) 10 min and (b) 50 min. The scale bars are 200 μm.

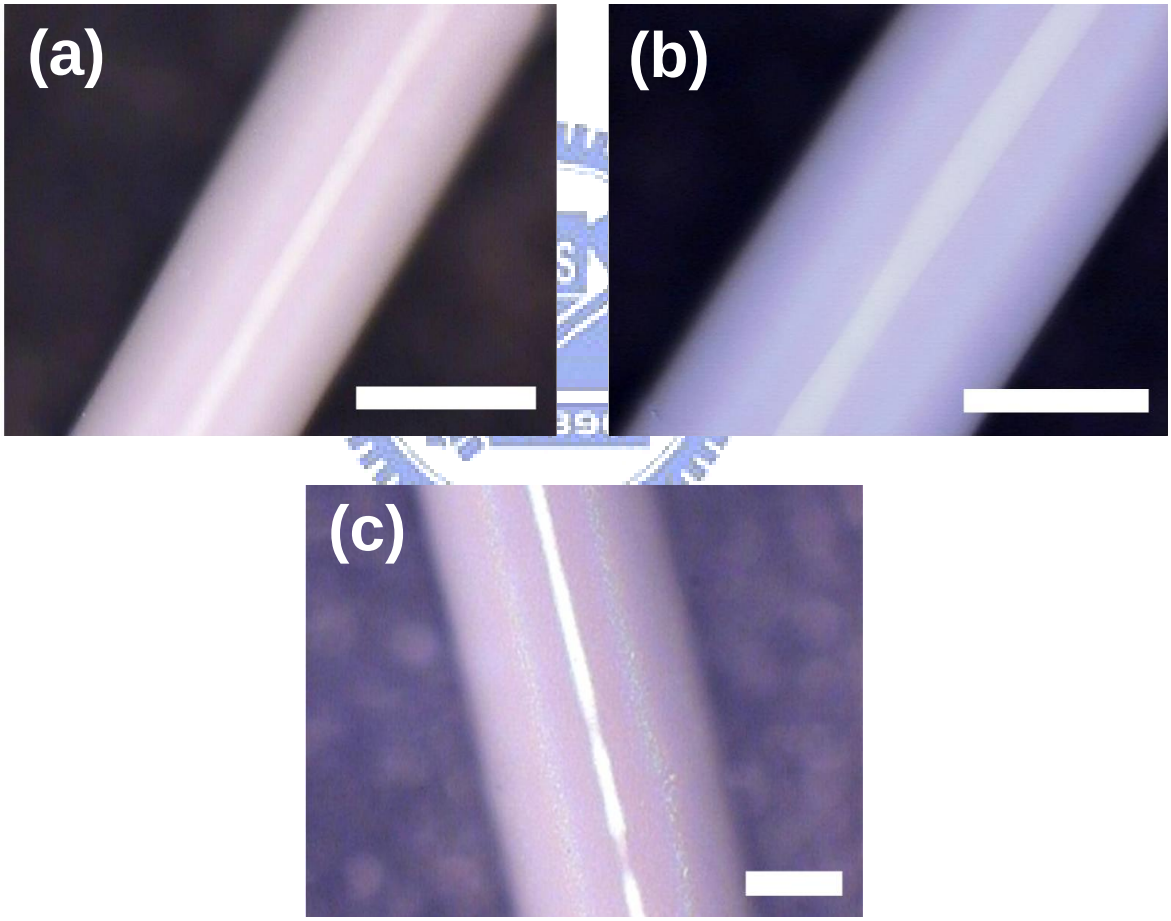

Figure 4.23 Optical microscopy images of CCC-660 self-assembled in PS-660 for (a) 10 min, (b) 30 min, and (c) 50min, respectively. The scale bars are 200 μm.

So far, we have demonstrated that in fabricating the CCCs in a fixed diameter, smaller microspheres were easier to assemble. We observed that the CCC-660 was strongly affected by the substrate. For example, a pale rainbow color appeared on the CCCs with a longer EPD time, as shown in Fig 4.23(c). In short, the EPD process could deliver cylindrical colloidal crystals in a short period, and the applied voltage was optimized with the time dependence of current density. Furthermore, with a high EPD rate and curved surface, self-assembling of PS microspheres on a cylindrical electrode was capable of producing colloidal crystals with defective arrangements. More details from optical observation will be discussed in following sections.

Chapter 5

Results and Discussion on NED and PS Removal Processes

This chapter provides the results and discussion for NED and PS removal process in nickel inverse opals fabrication. In the NED process, a potentiostatic electrodeposition technique was carried out on the colloidal crystals to fabricate nickel inverse opals (**NIO-460** and **NIO-660**) and cylindrical inverse opals (**CIO-460** and **CIO-660**). Figure 5.1 provides the SEM images for those inverse opal structures. To remove colloidal PS templates, the as-prepared samples were treated under different temperatures in chemical dissolution or heat treatment.

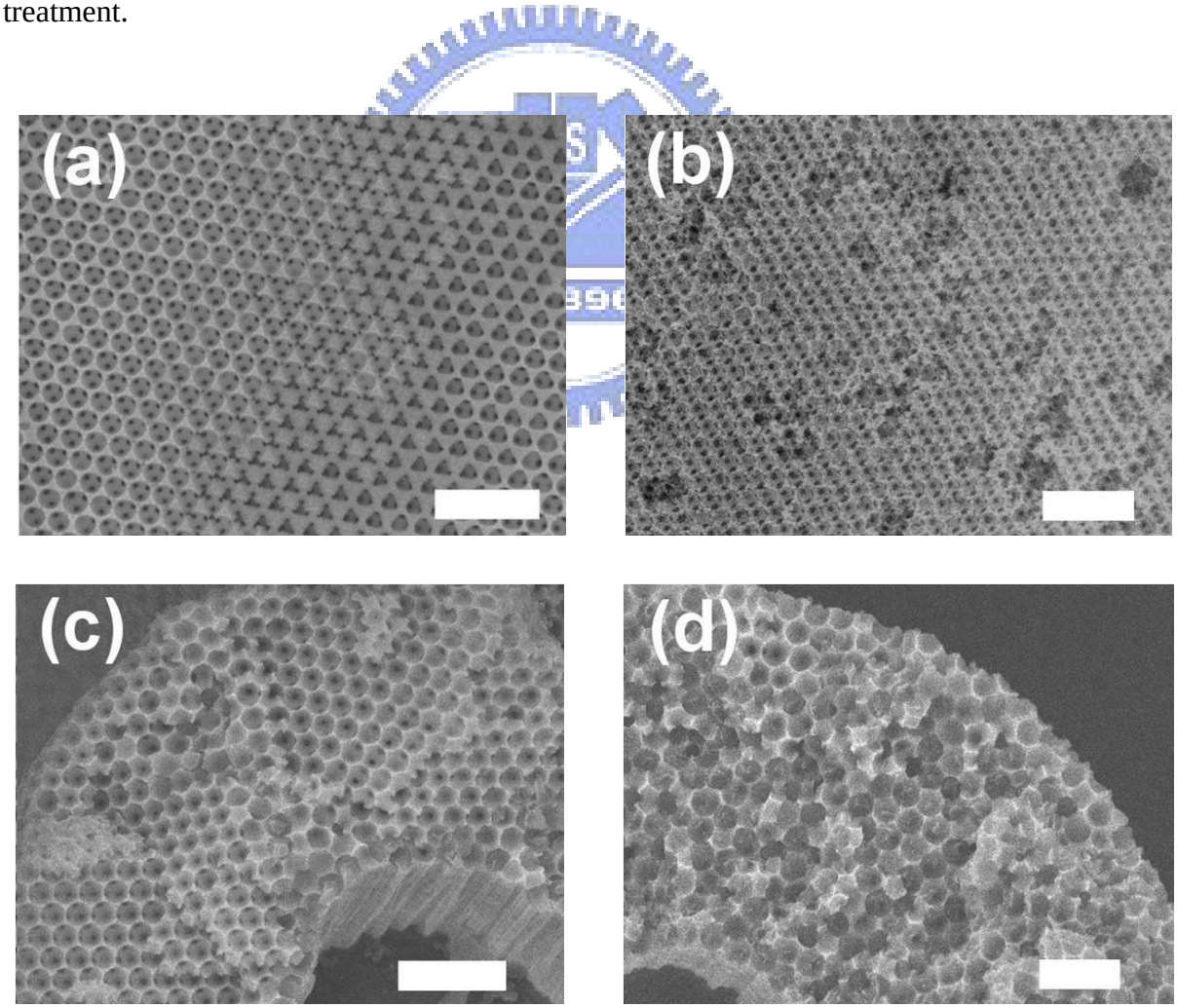

Figure 5.1 SEM images of (a) NIO-460, (b) NIO-660, (c) CIO-460, and (d) CIO-660. All scale bars are 2 μm.

Figure 5.2 presents the cross-sectional views for the as-prepared PCCs on ITO glass. The thickness of EPD layer for the PCC-460 and PCC-660 were 11.25 and 8.97 μm, respectively. As clearly shown in the figure, the PCCs were in good quality of proper stacking, and the PS microspheres demonstrated a three-dimensional close-packed arrangement.

Figure 5.3 displays the surface morphology for the as-prepared CCCs prior to the NED process. Clearly, the microspheres in the CCC-460 were in good order. In contrast, in the CCC-660, there revealed a defective packed structure. The insets exhibit the OM images for the as-prepared samples. The diameters were about 67.31 μm for the CCC-460 and 52.94 μm for the CCC-660, and these values were rather uniform along the longitudinal axis for both cases. It is noted that these colloidal templates were rather robust as immersing them in electrolytes did not produce unwanted detachments or structural damage.

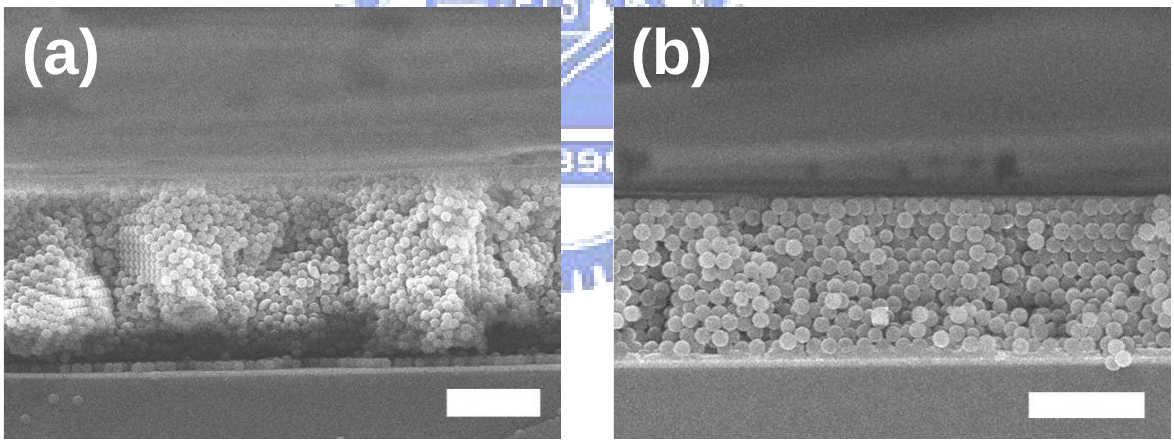

Figure 5.2 Cross-sectional SEM images for the (a) PCC-460 and (b) PCC-660 before NED process. The scale bars are 5 μm.

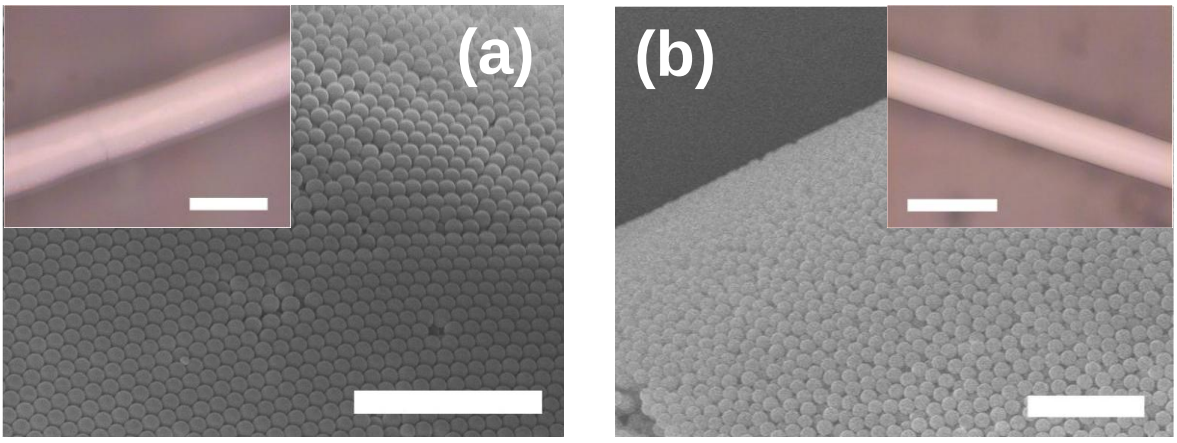

Figure 5.3 SEM images on the surface morphology of (a) CCC-460 and (b) CCC-660. The scale bars are 5 μm. Insets display optical microscopic images for CCCs with scale bars of 100 μm.

5.1 Fabrication of Planar Nickel Inverse Opals

5.1.1 Current Density in NED Process

Figure 5.4 demonstrates the time dependence of current density during the NED process on planar colloidal templates. The value for current density exhibited a sudden jump initially and fluctuated with a positive slope subsequently. Previously, the current variation was used to derive the number of layer for the as-deposited inverse opal [50]. Accordingly, the PS microsphere on the substrate served as a mask that screened the current density.

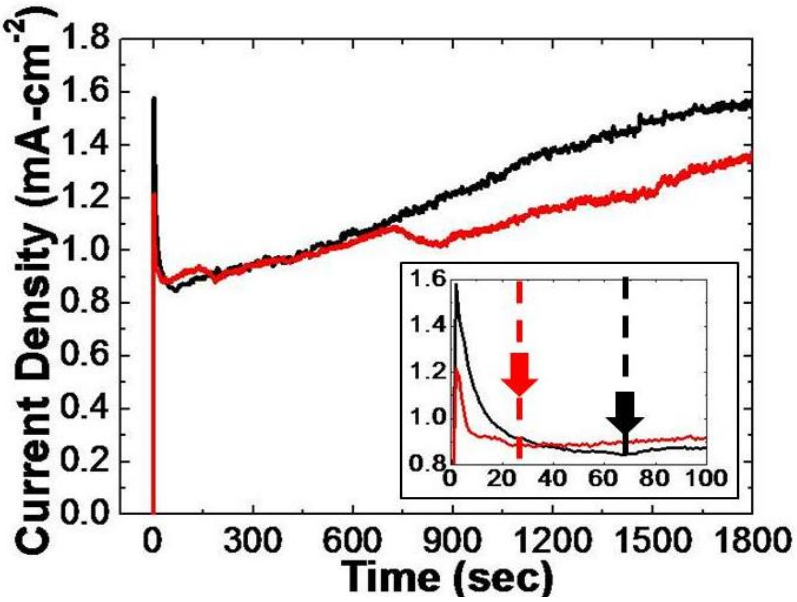

Figure 5.4 Time dependence of current density during the Ni electrodeposition at pH of 5.2 and 1 V on PCC-460 (**red**) and PCC-660 (**black**). The inset plot shows the transition points that were determined by the variation of current density at initial stage. Inset axes are identical with the principal plot.

From the plot, the first drop of current density was obtained at 25 and 70 sec for the PCC-460 and PCC-660, respectively. This indicated that the nickel was deposited on the substrate, and became thicker until filling the cone-like interstitials. Hence, it took about 25 and 70 sec in the NED process for the NIO-460 and NIO-660 to grow into their semi-layers. The positive slope was recorded in the current density, which means the supply of nickel ions was continuously throughout the colloidal template from the bulk electrolyte. Besides, the

increase in current density was resulted from the increased conductivity of electrode, because the nickel was deposited.

The XRD patterns for the NIO-660 and NIO-460 in multiple layers are exhibited in Fig. 5.5. The diffraction peaks in Fig. 5.5(a) confirmed a FCC structure with a preferred orientation of (111). The remaining two unmarked small peaks came from the substrate. The peaks from the substrates were also obtained in the plot of NIO-460 (Fig. 5.5(b)). The obvious noise from Fig. 5.5(b) indicated that its crystallinity was not as good as that of NIO-660. It is noted that the NIO-460 revealed only one characteristic peak in (111) plane. This suggested that formation of (200) and (220) planes was suppressed by physical confinement of the colloidal mask. To observe the as-deposited NIOs, the PS templates were further removed and the details in process are discussed later. Figure 5.6 shows the SEM images of NIOs-460 and NIO-660. Because it was expected to be harder for the electrolyte to percolate into the PCC-460, the quality of PCC-460 was likely to be maintained and improved over that of PCC-660. The insets in Fig. 5.6 exhibit the cross-sectional view for the NIOs. The ordered structure confirmed the robustness of the colloidal crystals in the electrolyte.

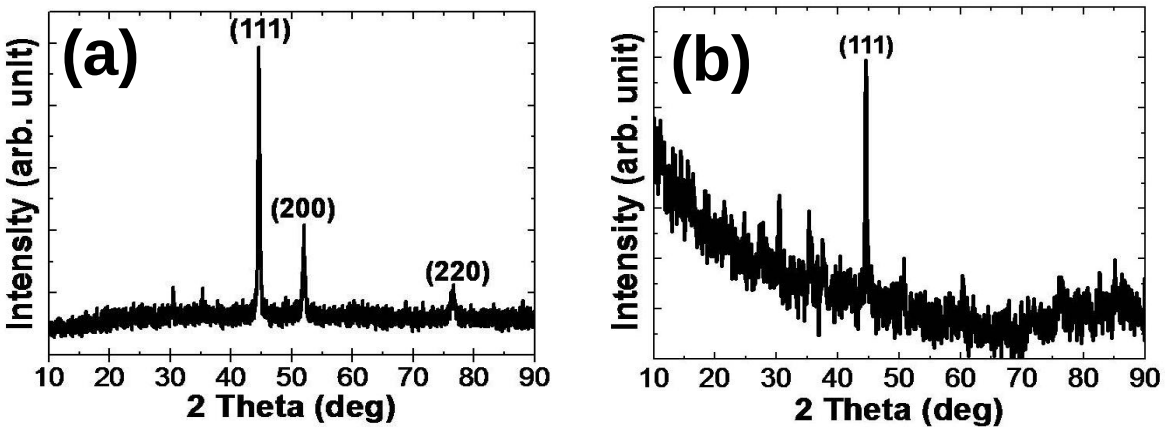

Figure 5.5 XRD patterns for planar (a) NIO-660 and (b) NIO-460.

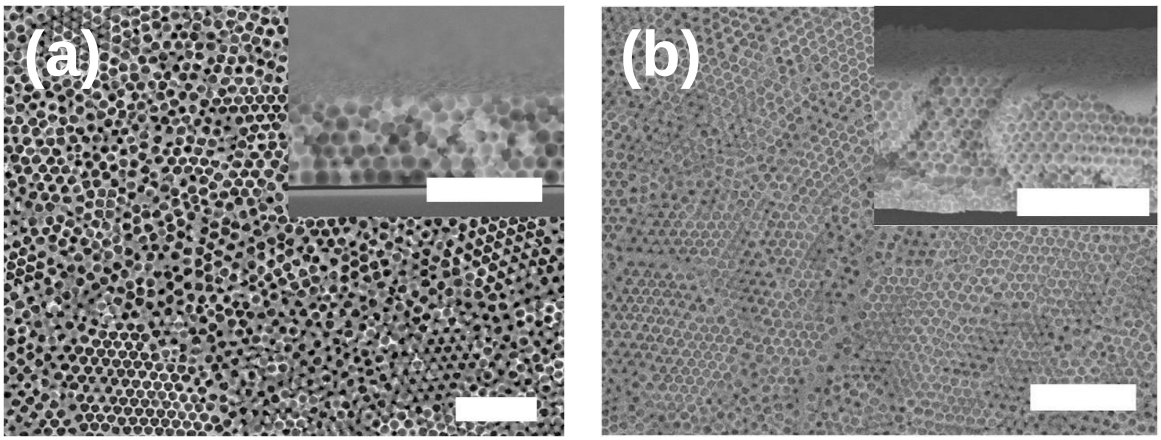

Figure 5.6 SEM images of multi-domains in planar (a) NIO-660 (b) NIO-460. The insets exhibit the cross-section view of each sample. All scale bars are 5 μm.

After Ni electrodepositions, the inverse opals revealed a somewhat disordered structure that displayed several lattice arrangements simultaneously. Their top view SEM images are shown in Fig. 5.7. Figure 5.7(a) exhibits the structure with only one hole in each pore, which corresponds to a rhombohedral lattice with 1-fold symmetry. Presented in Fig. 5.7(b) is a structure with two holes in each pore. That corresponds to the (110) in FCC. Figure 5.7(c) demonstrates a structure of closed-packed (111) plane. Figure 5.7(d) displays a (100) plane of FCC lattice with four holes in each pore, revealing a 4-fold symmetry with square shape. We surmised that appearance of these lattice structures was due to the shearing of microspheres occurring during NED process. Because immediately after the EPD, the samples were removed from the suspension and inserted into the Ni plating electrolyte. These disturbances would likely to engender undesirable shift in close-packed plane that results in defective structure.

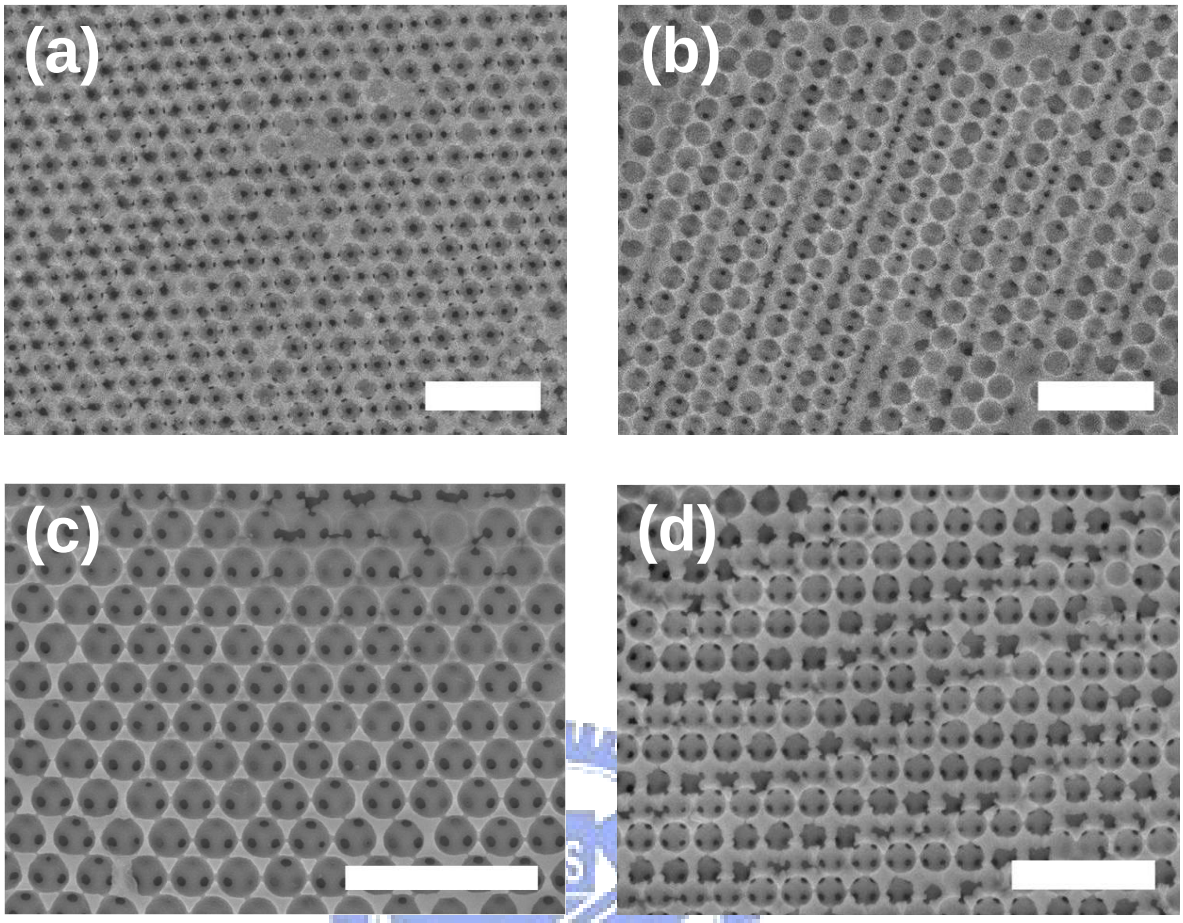

Figure 5.7 SEM images of different lattice arrangement in planar NIO-460;(a) Rhombohedral, (b) FCC-(110), (c) FCC-(111), and (d) FCC-(100). All scale bars are 2 μm.

5.1.2 Deposition Rate for Planar NED

Figure 5.8 presents the optical images of planar nickel inverse opals made of NED process for 30 min. Their color appeared in dark-rosy for the NIO-660 and grey-purple for the NIO-460. It is known that the color of NIOs was resulted from the contrast of refractive index between Ni and air. For example, the appearance of multi-layer NIOs would turn immediately dark when the ethanol was filled into the structure. The insets in Fig. 5.8 demonstrate the reflective color of the samples for semi-layer NIOs observed from different view angles. We realized that the NIOs with a semi-layer structure were in egg-shell shape, which functioned possibly as a concave mirror that could reflect the incident light contingent on the viewing angle. In short, the NIO with a semi-layer structure could reveal an iridescent character, while the ones with multi-layers were sensitive to contrast in the

refractive index.

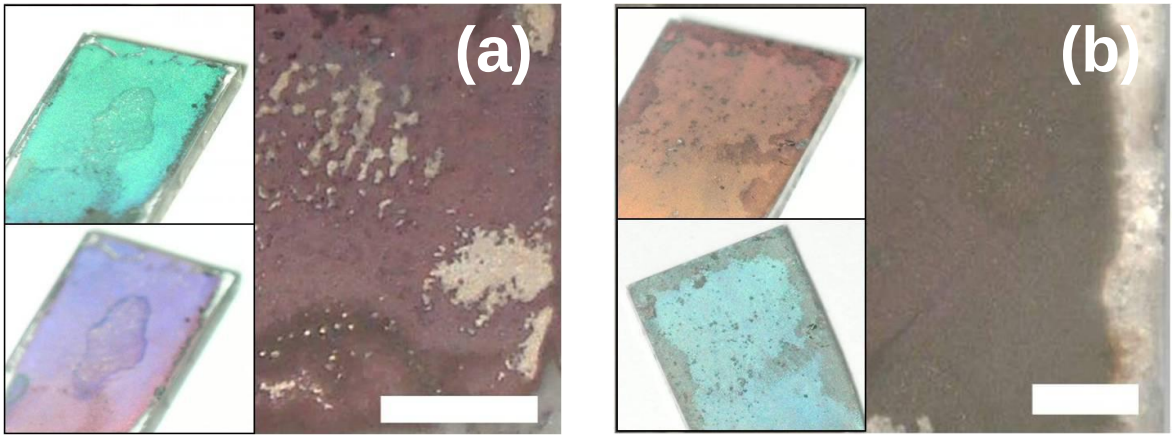

Figure 5.8 Photographic images of multi-layer (a) NIO-660 and (b) NIO-460. The scale bars are 500 μm. The insets in each figure display the color of the semi-layer samples changes that changes with the view angle.

Figure 5.9 demonstrates the variation of layer number as a function of NED time for the NIO-660 and NIO-460. The reduced NED rate for the NIO-660 was resulted from the larger filling volume in each layer compared with that of NIO-460s. The deposition rate for the NIO-460 and NIO-660 were 0.1641 μm-min^{-1} and 0.1494 μm-min^{-1}, respectively. This slight difference in the deposition rate might be attributed to the size-effect caused by microspheres. It is likely that the growth of particular planes was limited in NIO-460, leading to a higher conductivity for electron transport that increases the NED rate. In addition, the plating rates in both plots were slightly increasing with time. These behaviors suggested that the difficulty in electrolyte supply was eased as the deposit approached to the surface of colloidal template. Figure 5.10 presents the SEM images of NIOs in different filling fraction. With a reduced deposition rate, the morphologies for the NIO-660 could be controlled carefully via variation in the deposition time.

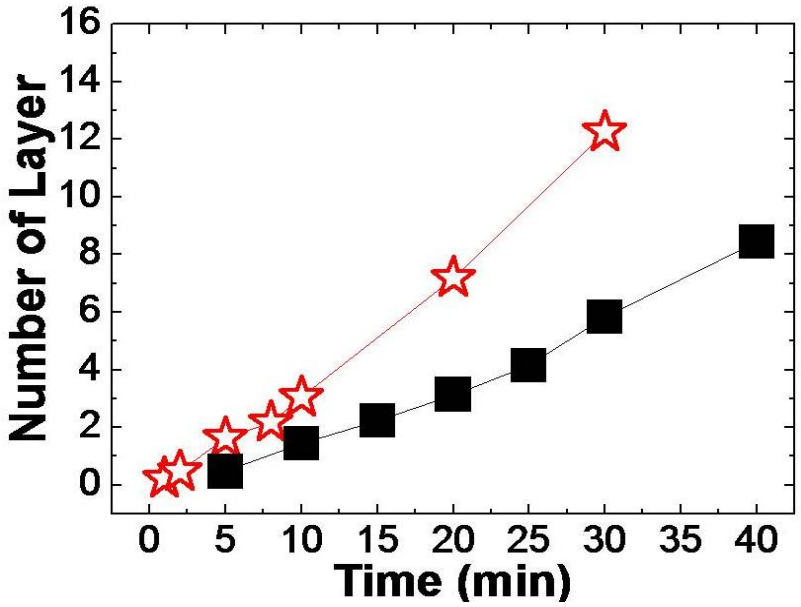

Figure 5.9 Layer number versus NED time for the planar NIO-660s (■) and NIO- 460s (☆) . The applied voltage was 1 V.

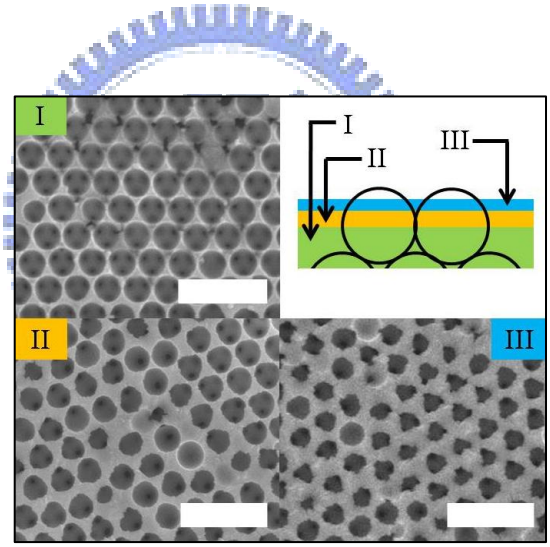

Figure 5.10 SEM images of NIO-660s with different filling fractions. Inset sketch shows a schematic diagram of different filling fractions. The scale bars are 2 μm.

Figure 5.11 and 5.12 exhibit the SEM images of NIO-660s and NIO-460s. From Fig. 5.11, the structure at the bottom of NIO-660s was usually in better arrangement than what appeared near the surface. Because of its larger size in voids, the percolation of electrolyte in the PCC-660 was expected to be easier than that of PCC-460. Hence, we observed a larger disturbance effect from shearing. As a result, we were able to obtain a better crystallinity from NIO-460.

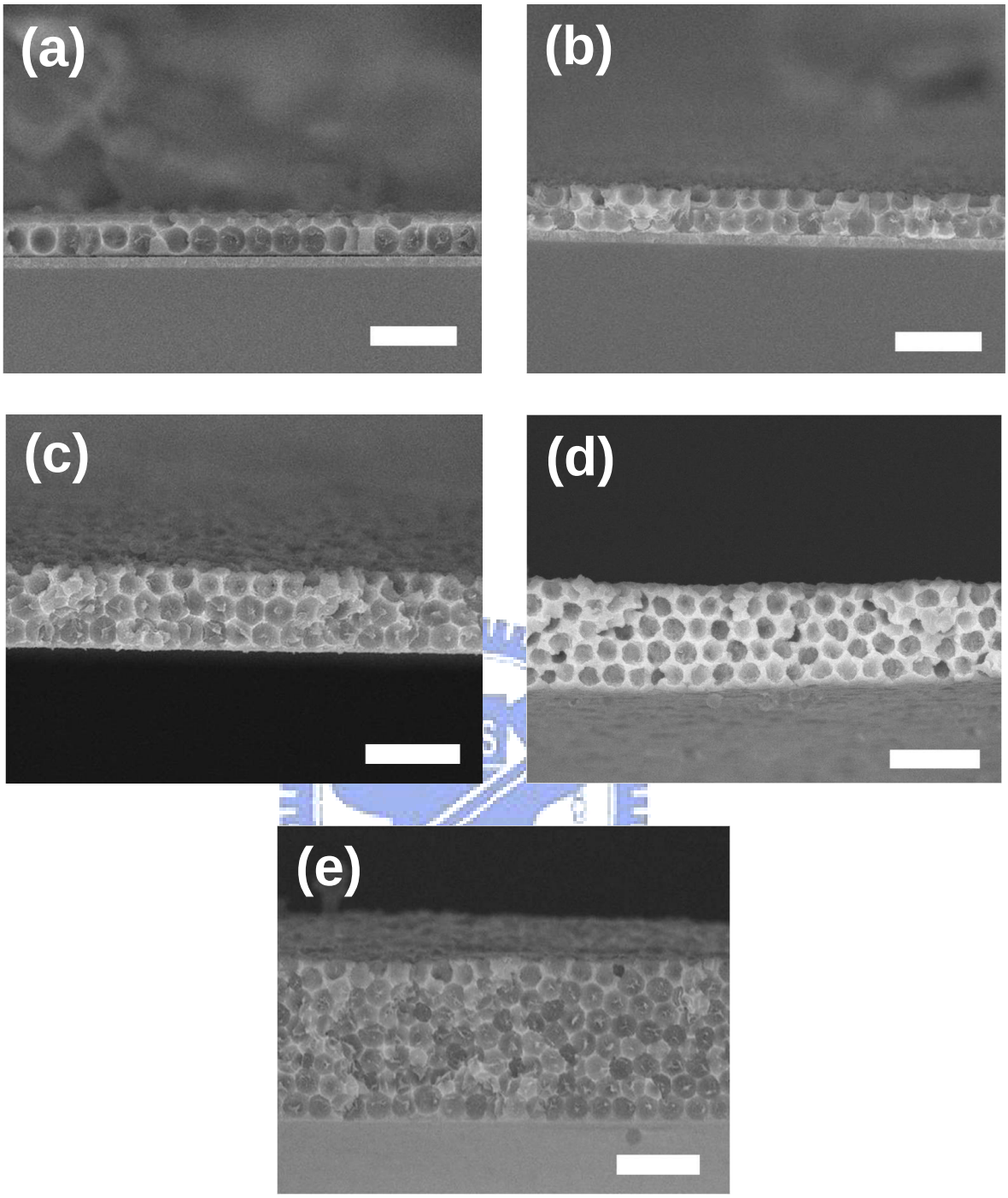

Figure 5.11 SEM images of NIO-660 prepared under 1 V for (a) 10, (b) 15, (c) 20, (d) 25, and (e) 30 min, respectively. All scale bars are 2 μm.

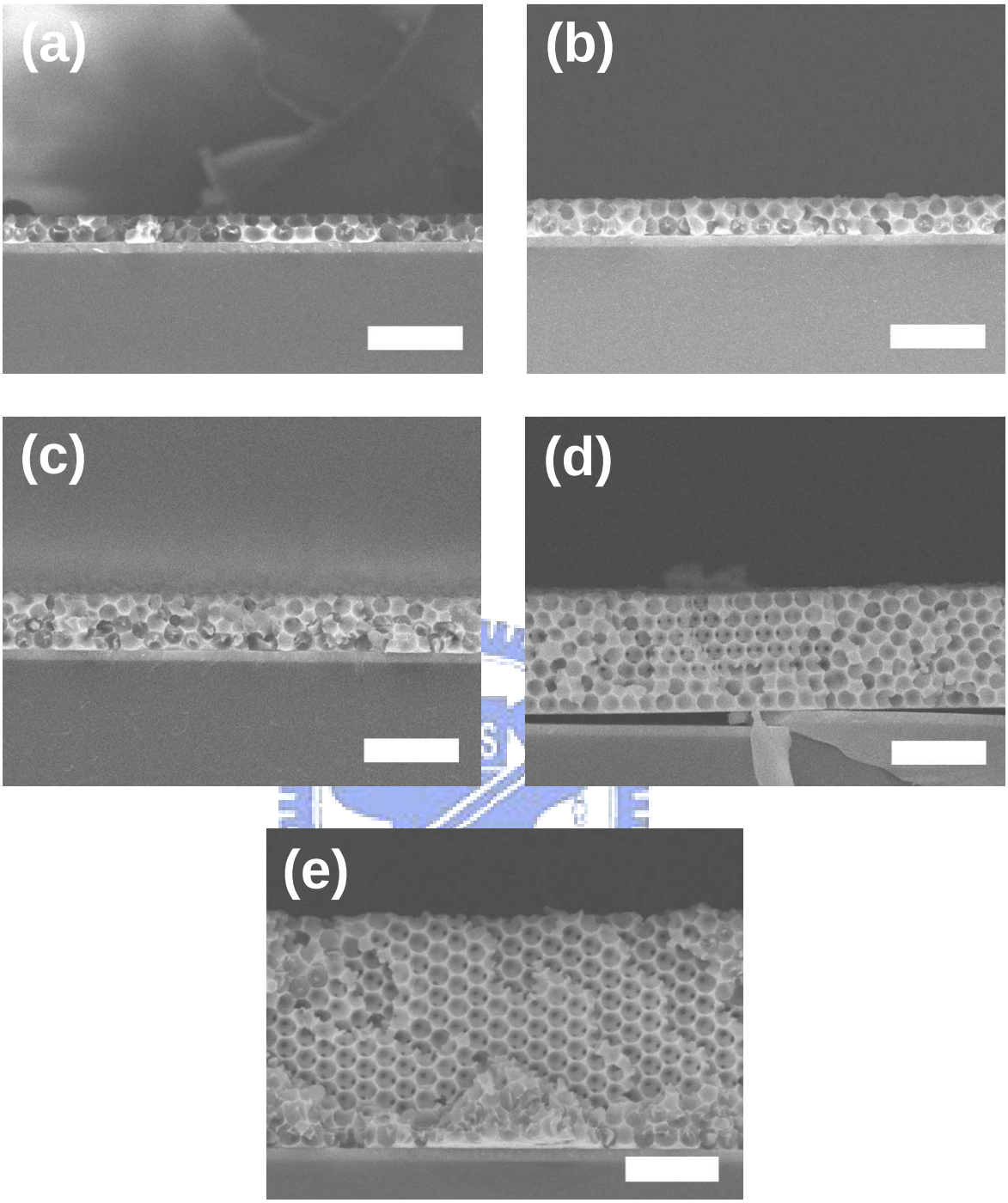

Figure 5.12 SEM images of the NIO-460 prepared under 1 V for (a) 5, (b) 8, (c) 10, (d) 20, and (e) 30 min, respectively. All scale bars are 2 μm.

5.2 Fabrication of Cylindrical Nickel Inverse Opals

5.2.1 Current Density in NED Process

Electrodeposition was carried out on CCCs to form the cylindrical inverse opals. Figure 5.13 presents the plot of current vs. time. Similar to the planar case, the electroplating process can be divided into two parts, as presented in the inset. The primary regime left to the dash line included a peak in current, followed by the regime right to the dash line that revealed an increasing current density. Consistent with earlier planar case, the values for current density were first increased and ascended to the highest point within 20 sec. It suggested that a rapid reduction of nickel ions occurring at the CF-electrolyte interface. We observed a larger current jump for the CCC-660 over that of CCC-460 because its defective colloidal structure allowed better electrolyte percolation.

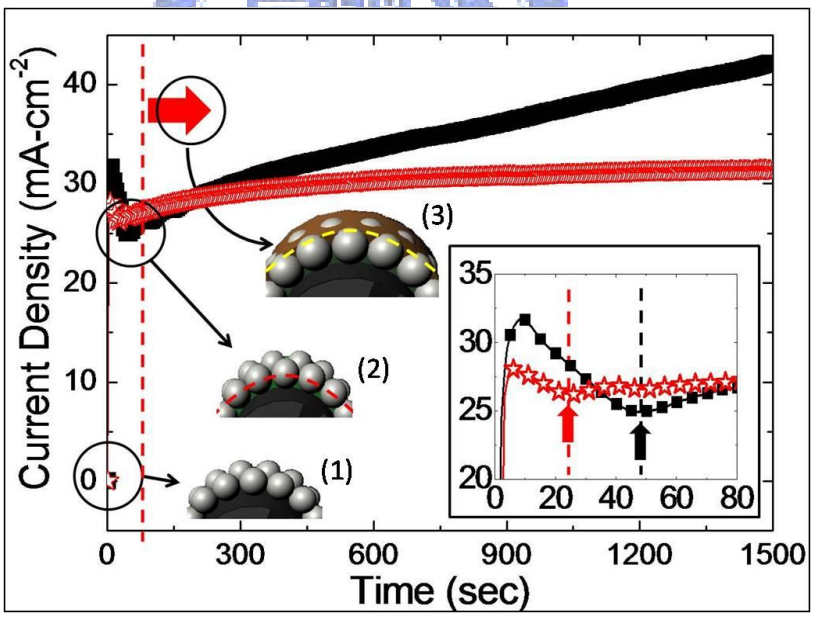

Figure 5.13 Time dependence of current density during the electrodeposition at pH of 5.2 and 1 V on CCC-460 (☆) and CCC-660 (■). The inset sketches illustrate the stages of deposits inside the PS template at each point indicated by arrows, and the plot shows the transition points that were determined by variation of current density at initial stage. Inset axes are identical with the principal plot.

After the current density reached the valley, the nickel deposits just filled the void around the semi-spheres, as shown in sketch (2). This suggested that a semi-egg-shell structure deposited on the CF can be achieved by controlling the deposition time. After that, the replenishment of Ni ions from the bulk electrolyte was funneled by the colloidal template, as shown in sketch (3). Therefore, the NED rate increased with various slopes, and the effective path for electroplating was extended with diameter of deposits, especially in CCC-660 case.

Figure 5.14 shows the CIO-660 with semi- and multi-layer deposits. The inset in Fig. 5.14(a) provides the semi-layer of CIO. The semi-layer was bent and its morphology was strongly affected by the CF. When the thickness of CIO was increased, its surface was becoming flatter and more uniform, as shown in Fig. 5.14(b). As shown in the inset, the CIO was in a disorder structure, but the inter-pores were still observed. This indicated that the PS microspheres were stacked together during the NED process. Figure 5.15 provides the EDX analysis of the as-prepared CIOs. The carbon and nickel peaks were from the substrate and coating, while the oxygen peak was from the oxide layer produced by heat treatment.

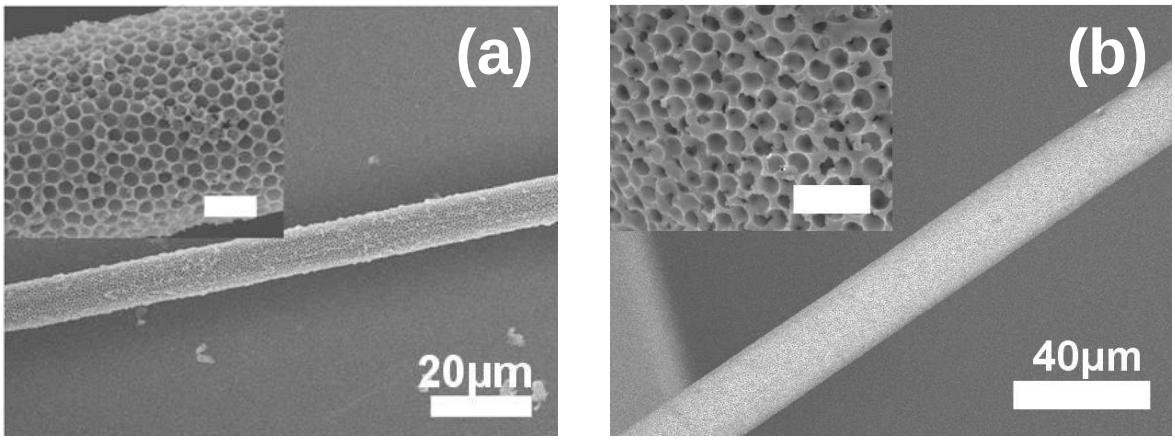

Figure 5.14 SEM images for the (a) semi-layer and (b) multi-layer CIO-660. Insets provide the magnified images. The scale bars in the insets are 2 μm.

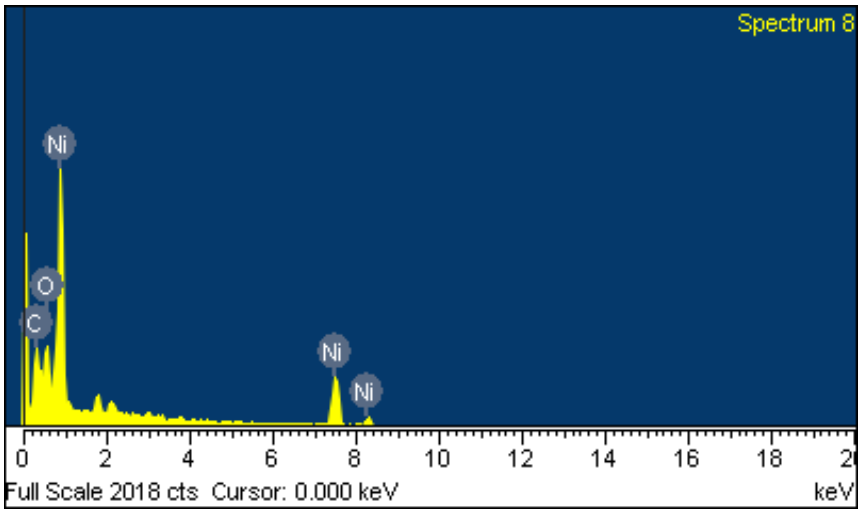

Figure 5.15 EDX analysis of the as-prepared CIOs.

Figure 5.16 provides the SEM images in cross-sectional and side views for the CIOs. As shown, the cylindrical inverse structures replicated the arrangement of primary CCCs. As shown in Fig. 5.16(a), the arrangement of 660 nm microspheres near the substrate was in a close-packed structure with a slightly bent angle. In addition, the ordered structure could be found at about 12~15 layers from the substrate.

In principle, when the circumference of any layer is at integral times of microsphere diameter, the arrangement for those microspheres in that particular layer is expected to stay ordered close-packed. However, in practical case, the stacking in a specific layer is also affected by the layers above and below. As a result, the possibility of close-packing in any layer is greatly reduced. Hence, occurrence of close-packed structure can only be observed when the $2\pi R$ (R is the radius) is much larger than the r (radius of microspheres). Because of this, the pores of the CIO-660, shown in Fig. 5.16(b) were still in disordered state.

On the contrary, the PS microspheres of 460 nm were in good order and formed a close-packed array near the substrate, as shown in Fig. 5.16(c). The ordered structure could be obtained after only 3~4 layers. In addition, more hexagonal pores appeared as the thickness for the CIO-460 was increased. Ordered domains could also be obtained on the surface, as shown in Fig. 5.16(d).

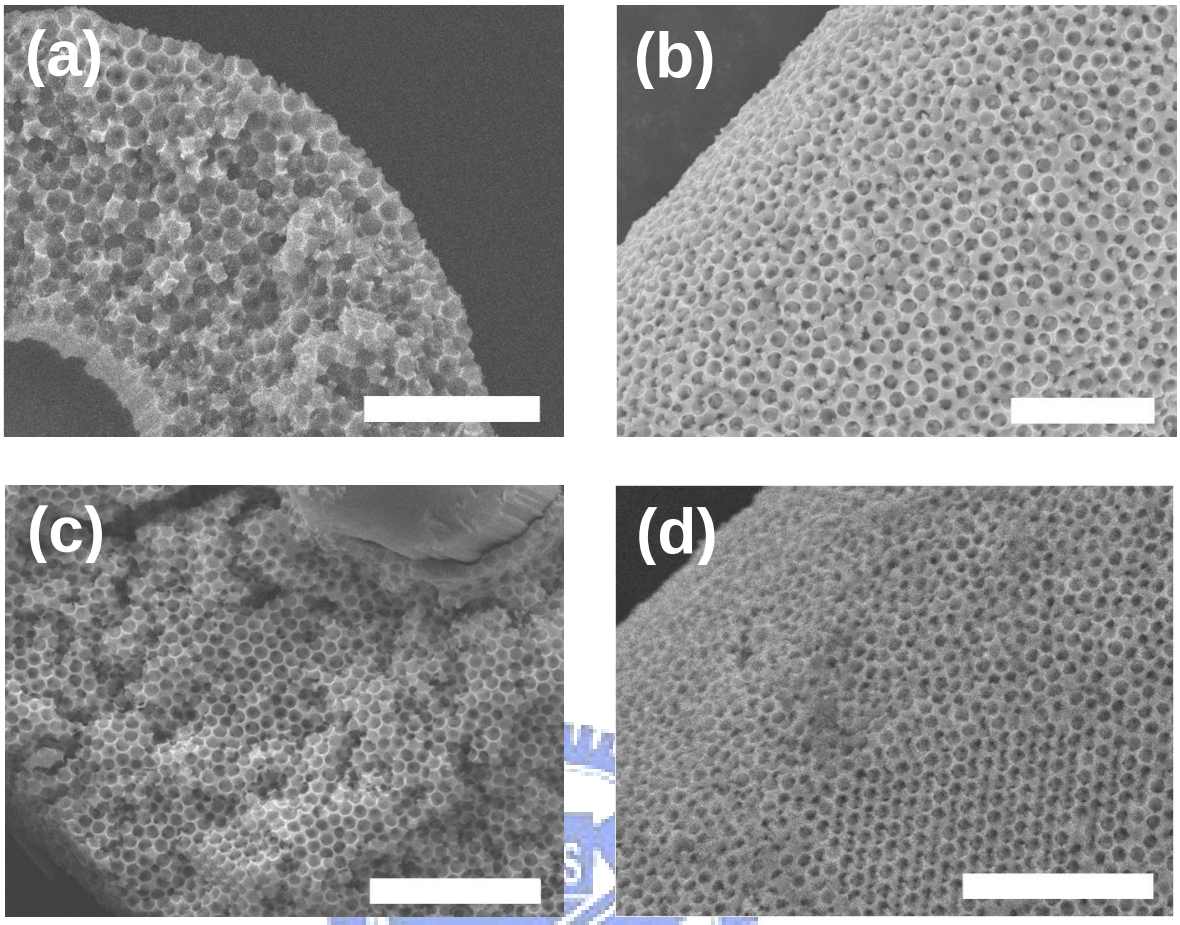

Figure 5.16 SEM images in the (a) cross-sectional and (b) side views for CIO-660, as well as (c) cross-sectional and (d) side views for CIO-460. The fabrication time was fixed at 10 min. The scale bars are 5 μm.

5.2.2 Deposition Rate of Cylindrical NED

Figure 5.17 demonstrates the OM images for the CIO-660 under different NED time. In Figure 5.17(a), the carbon fiber was covered with a semi-layer nickel inverse opal. Like the NIOs, some color segments were observed on the surface as a result of the concave morphology. The inset in Fig. 5.17(a) exhibits the fringes of a carbon fiber, and these fringes were also observed on the CIO surface shown in Fig. 5.17(a). When the fabrication time was increased, the CIOs revealed a dark-red color, as shown in Fig. 5.17(b). The darken appearance was resulted from the light absorption characteristic of porous structure. However, the brightness of metal was obtained when the NED time was increased, as displayed in Fig. 5.17(c). It suggested that a flatter surface was acquired as the diameter of

CIO was increased. In this way, the incident light was reflected easier than a thinner CIO. Figure 5.17(d) shows the magnified picture of CIO-660 of 10 min, and the pattern of inverse opal was clearly observed. It was noted that the bright spots represented the position of holes, while the protrusion-like grain boundaries appeared as dark lines.

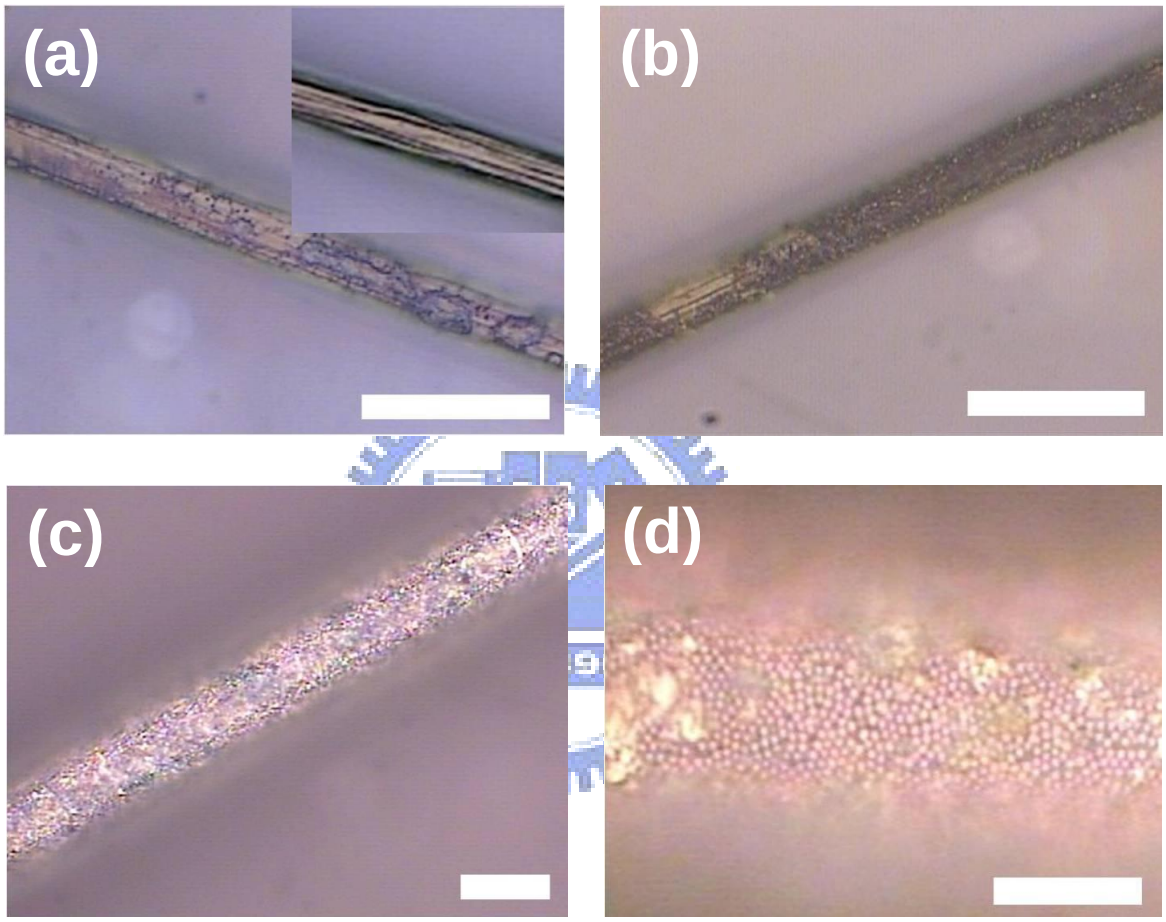

Figure 5.17 Optical microscopic images of the CIO-660s after NED process for (a) 30 sec, (b) 1 min, and (c) 10 min. Figure (d) is the magnified image of (b). The inset in (a) provides the image of a pure carbon fiber. The scale bars are 20 μm in (a) to (c), and 10 μm in (d).

Figure 5.18 demonstrates the time dependence of thickness for single CIO during the NED process. The deposition rate for the CIO-660 and CIO-460 were 0.4904 μm-min^{-1} and 0.2508 μm-min^{-1}, respectively. Apparently, the NED occurred faster on the CIO-660 case, which was consistent with the current density versus time plot of NED. This also suggested that difference in the deposition rate became obvious as the thickness of EPD layer in NED process was increased.

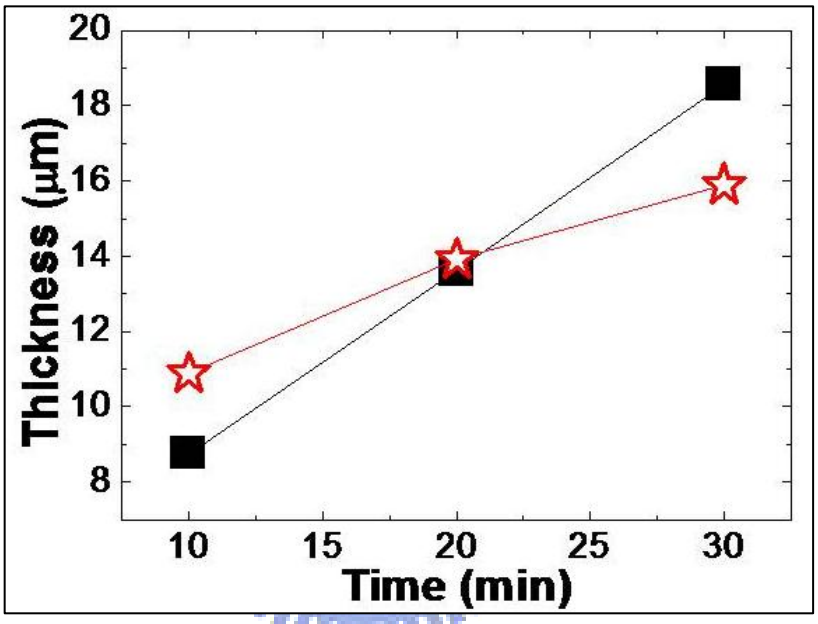

Figure 5.18 Thickness versus NED time for the CIO-660 (■) and CIO- 460 (☆) prepared at an applied voltage of 1 V.

Figure 5.19 presents the SEM image of CIO for different NED time. The depositing layers were around the carbon fibers, and the tubular structures were filled with periodic holes. The carbon fiber in the middle could be removed by thermal oxidation, as shown in Fig. 5.19(b) and Fig. 5.19(c). Figure 5.20 exhibits the SEM images of many CIOs. These samples were obtained by EPD on a CF bundle (~3000 CFs), followed by NED. Despite there was uniformity issue among individual CFs, the EPD and NED process were still able to prepare inverse opals in reasonable shape.

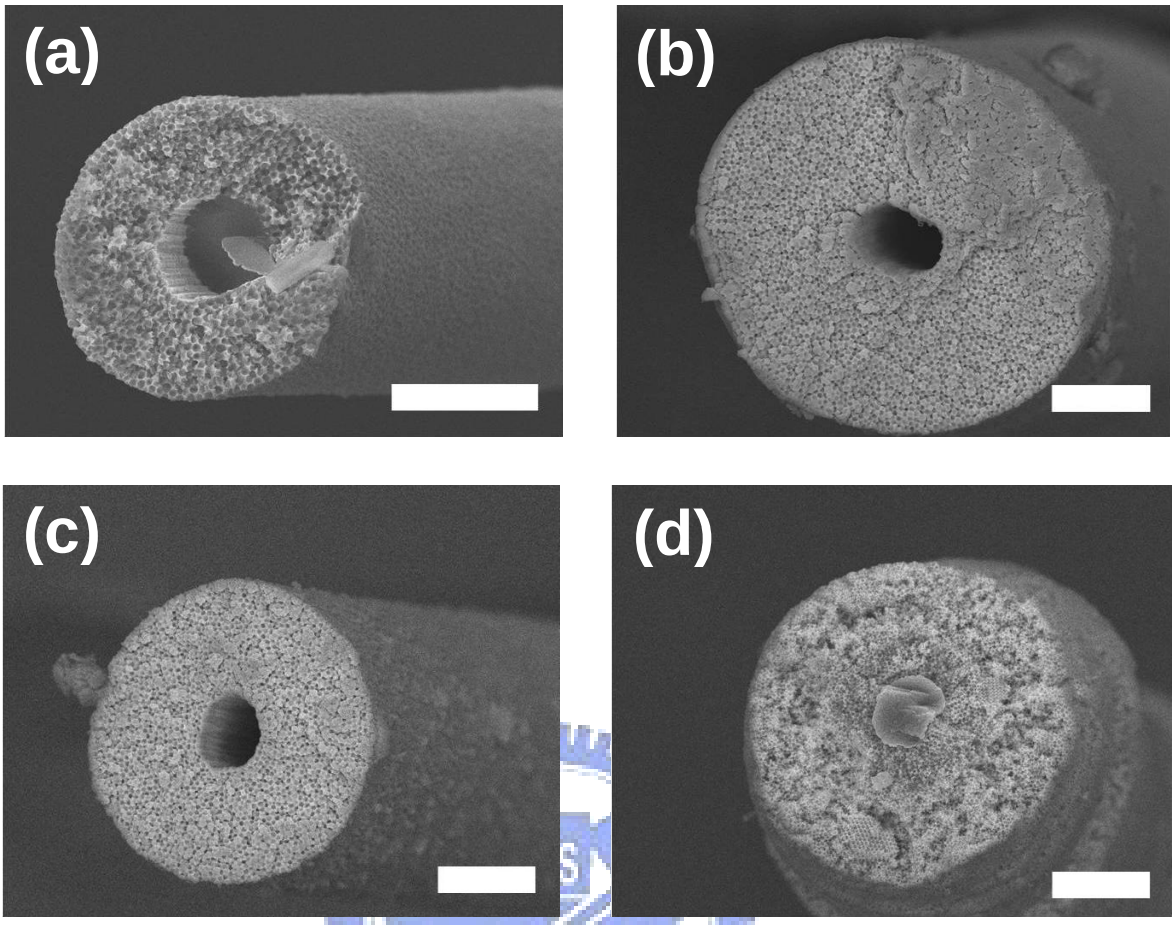

Figure 5.19 SEM images for the CIOs made of NED for different deposition time; (a) CIO-660 for 10 min, (b) CIO-660 for 30 min, (c) CIO-460 for 10 min, and (d) CIO-460 for 30 min. All scale bars are 10 μm.

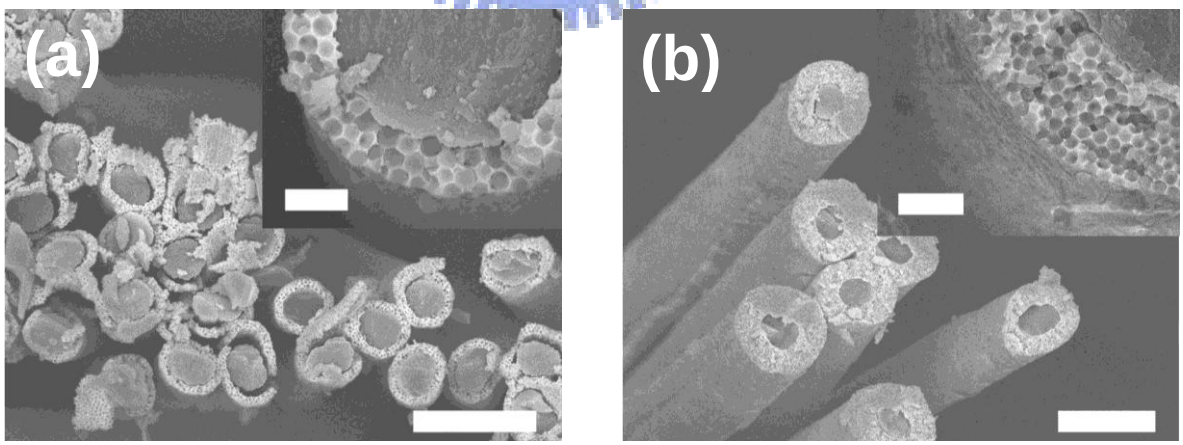

Figure 5.20 SEM images of a bundle (3000 CFs) in (a) CIO-660 and (b) CIO-460 made of NED for 20 min. Insets show the magnified view for the CIOs. The scale bars are 20 μm in the figures and 2 μm in the insets.

5.3 PS Removal Process

5.3.1 Chemical Dissolution

Figure 5.21 exhibits the OM image for the as-prepared CIO. In appearance, the Ni coating was covered with a pale film, which was attributed to the non-filled CCCs. To remove the PS template, ethyl acetate was used to dissolve the polystyrene at room temperature and 50℃, respectively.

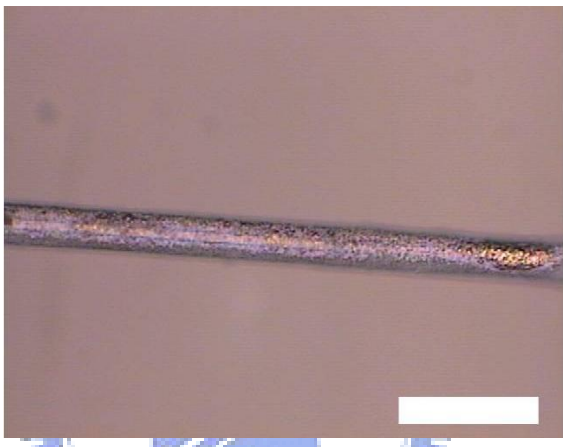

Figure 5.21 Optical image for the as-deposited CIO without removing the PS microspheres. The scale bar is 100 μm.

Figure 5.22 presents the SEM images for NIO-460 after immersion in ethyl acetate for 2 days at room temperature. As clearly seen in the top-view, the PS microspheres were partially dissolved, becoming a gel state. In Fig. 5.22(b), only the layers near the surface were PS-free, while those near the bottom were still filled by PS. Because the dissolution rate of PS was relatively slow at room temperature, the viscosity of dissolved particles remained high. Therefore, the etching temperature was further raised to 50℃, as shown in Fig. 5.22(c) and Fig. 5.22(d). We observed that the etching rate was increased with the temperature, while the evaporation of ethyl acetate was getting faster as expected. Hence, some precipitations were generated within the structure and on its surface because of supersaturation of PS. In addition, due to a faster etching rate and a lower viscosity of

dissolved PS, the PS microspheres at the bottom part were also dissolved, as shown in Fig. 5.22(d).

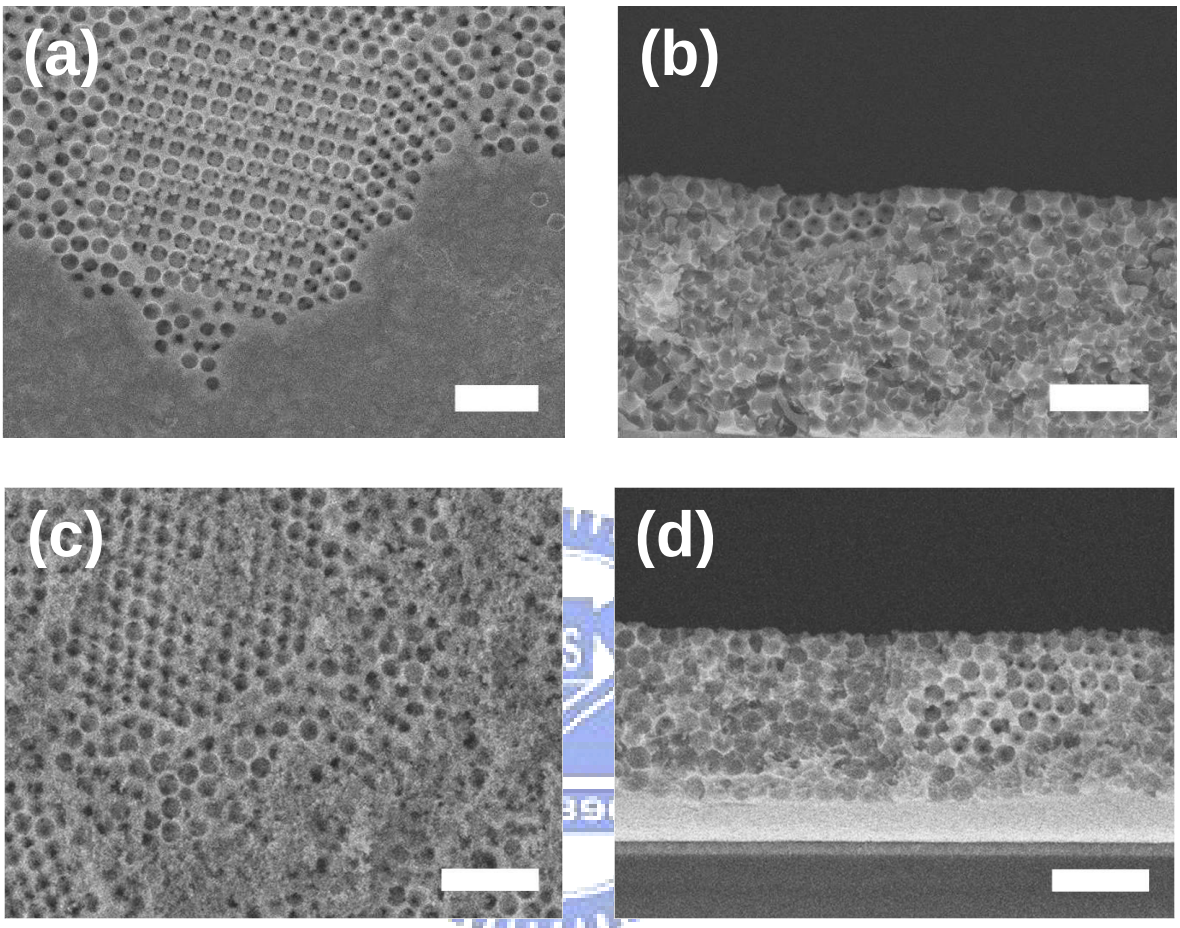

Figure 5.22 SEM images in (a) top and (b) cross-sectional view for the NIO460 after PS removal at room temperature, as well as (c) top and (d) cross-sectional view at 50℃. The immersion time was 2 days. The scale bars are 2 μm.

5.3.2 Thermal Oxidation

Figure 5.23 demonstrates the TGA profiles for the PS, as-deposited nickel, and CFs. In the TGA curve for the PS, event of notable weight loss occurred at 250 ℃, indicating volatile CO_x was formed from the oxidation of PS. On the other hand, the TGA response for the as-deposited Ni displayed a negligible weight increase until 500 ℃, at which point a rapid weight gain was detected. The sharp rise in the sample weight inferred considerable nickel oxidation above 500 ℃. The oxidation for CFs took place as the temperature was above 400

℃, but obvious weight loss occurred at 520 ℃. Combining these three curves, the heating temperature was set above 250 ℃ to remove the PS. Hence, heat treatments in 250, 350, and 450 ℃ for 2 days were carried out on NIO-460 samples to remove the colloidal template.

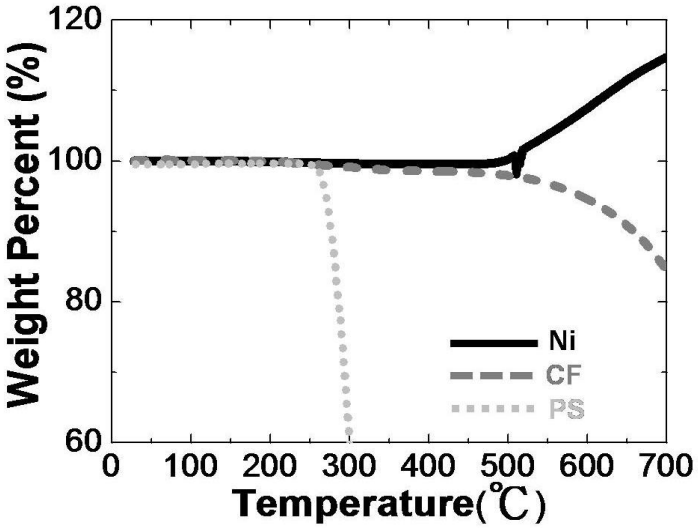

Figure 5.23 TGA profiles for the CFs, PS microspheres, and Ni coating.

Figure 5.24 provides the SEM images for the NIO-460 after heat treatment at different temperatures. As shown in Fig. 5.25(a), a heat treatment at 250 ℃ for 2 days could effectively evaporate the PS template without any alteration on the structure. Some PS residues were still trapped at the bottom of NIOs. However, they could be removed as the heating time was prolonged. As the temperature was raised to 350 ℃, the structure of NIO maintained moderate disorder in pores, as shown in Fig. 5.24(b). Meanwhile, the surface roughness for the NIOs was increased by the oxidation, and particles of nickel oxide were formed on the surface, as shown in the inset. Also, lattice distortion was observed on the NIOs after heat treatment at 450 ℃, as presented in Fig. 5.24(c). Theoretically, the volume ratio of nickel oxide to nickel was 1.6, which inferred that the oxidation process might change the pore size of the NIOs. As clearly seen in the figure, these pores were transformed from circles into polygons, and their positions were largely shifted due to the thermal oxidation.

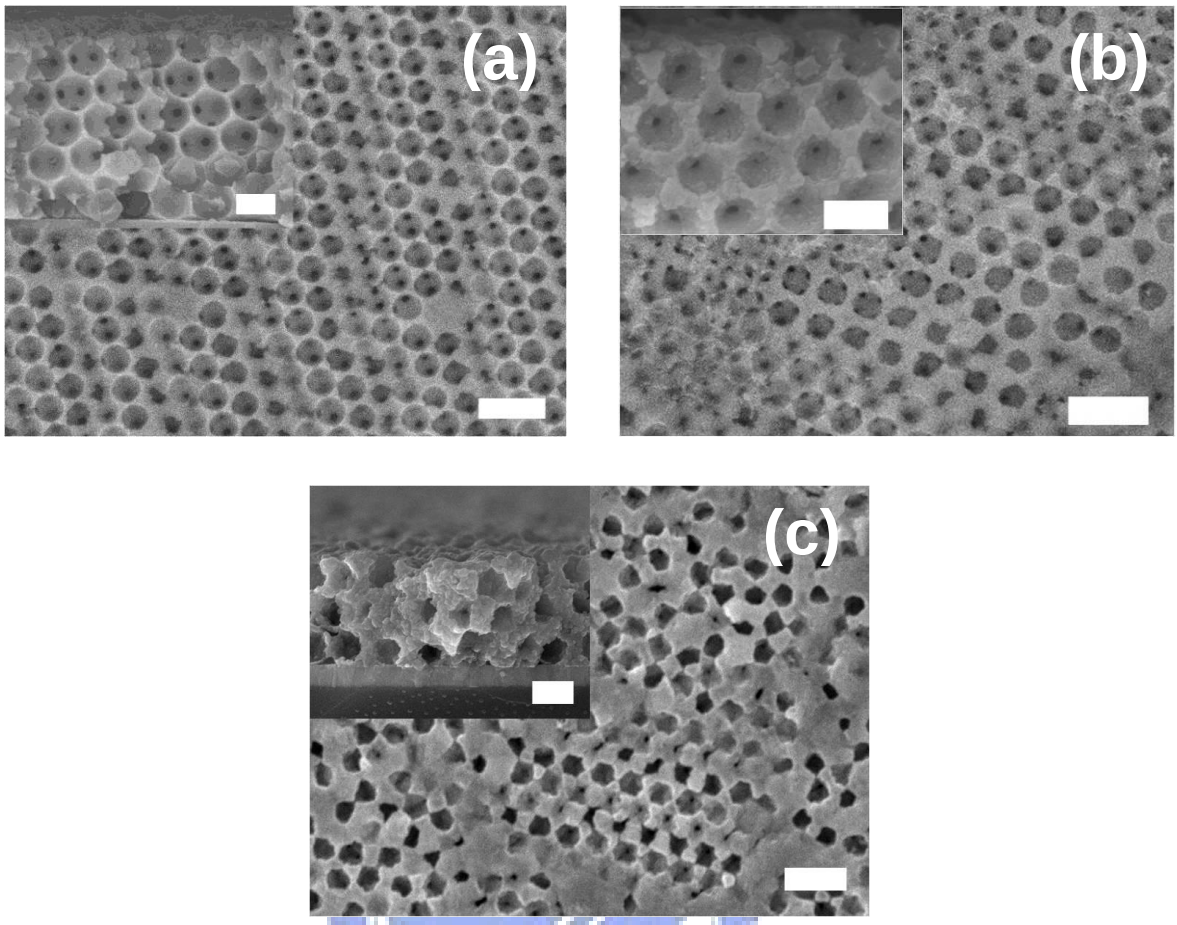

Figure 5.24 SEM images for the NIO-460 after thermal oxidation at (a) 250, (b) 350, and (c) 450 ℃ for 2 days. Insets show the cross-sectional view for the samples. The scale bars are 1 μm in the figures and 500 nm in the insets.

Figure 5.25 provides the XRD pattern for the NIO-460 after heat treatments. As mentioned before, the as-deposited NIO-460 revealed only one peak in (111) plane. Its intensity was largely increased by the heat treatment at 250 ℃ for 2 days. It suggested that the crystallinity of NIO-460 was improved considerably without formation of other preferred orientations. Moreover, the presence of (200) plane in the NIO was observed by heat treatment at 350 ℃. These peaks were converted to nickel oxide peaks at 450 ℃. This suggested that the oxidation was rapidly taking place above that temperature. In sum, with a heat treatment at 250 ℃, the PS templates in the NIO could be removed entirely, and the crystallinity of the samples was improved simultaneously.

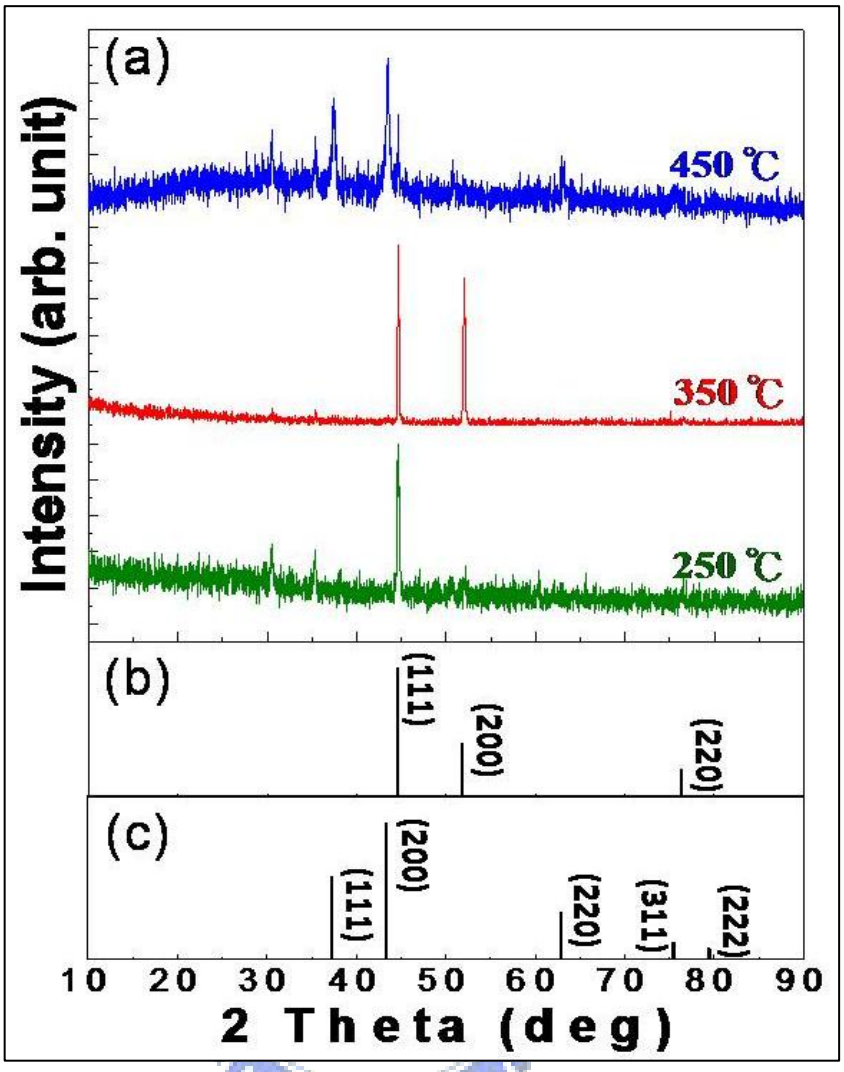

Figure 5.25 X-ray diffraction patterns for (a) the NIO-460 after heat treatment at various temperatures, (b) Ni from JCPDS 04-0850, and (c) NiO from JCPDS 47-1049.

Chapter 6

Measurements and Analyses

6.1 Electrical Measurements

6.1.1 Sheet Resistance of Planar Inverse Opals

Before taking the measurement, the surface of NIOs was deposited with gold electrodes by e-beam evaporation, as shown in Fig. 6.1. These gold electrodes were 300 nm in thickness, and the contact area between gold and NIOs was 0.0314 mm^2. The inset sketch provides a cross-sectional profile for the samples. The I-V curves were recorded with a 2-point arrangement, which was in the middle of the nearest two gold electrodes. The diameter for the measured electrodes was 200 μm, and the distance between them was 500 μm.

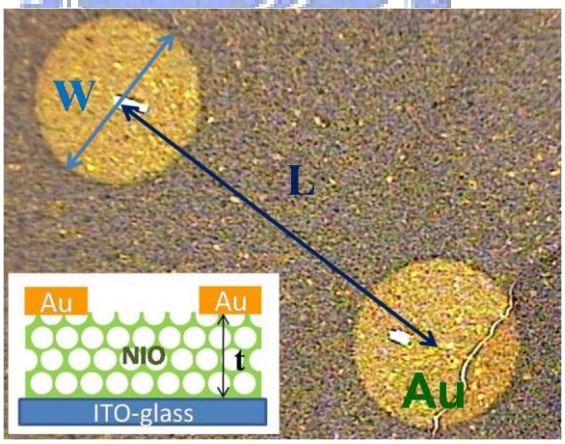

Figure 6.1 Optical microscopic image of gold electrodes on the NIO for electrical measurements. The sketch illustrates the setting in measurement.

To obtain the sheet resistance, the measured value was calculated with following equation;

$$\rho_s = \frac{\rho}{t} = R_{nio} \times \frac{W}{L} \qquad \frac{1}{R} = \frac{1}{R_{nio}} + \frac{1}{R_{ito}} \qquad \text{[eq. 6.1]}$$

where ρ_s is the sheet resistance, ρ is the resistivity, t is the thickness of NIOs, R_{nio} is the resistance of NIO film, W is the diameter of the gold electrodes, L is the distance between two

measured electrodes, R_{ito} is the resistance of ITO substrate, and R is the resistance derived from the linear I-V curve.

Figure 6.2 displays the sheet resistance of NIOs in different layers. Also provided are the sheet resistances for ITO and Ni film. As shown, the values for NIOs were much lower than that of pure ITO substrate. It is because the Ni was relatively conductive. The values for NIO-660 were close to that of Ni film. In contrast, the values for NIO-460 were considerably larger than both Ni film and NIO-660. We surmised that the smaller porous structure of NIO-460 provided a longer path not only on surface but in its structure for electron transport.

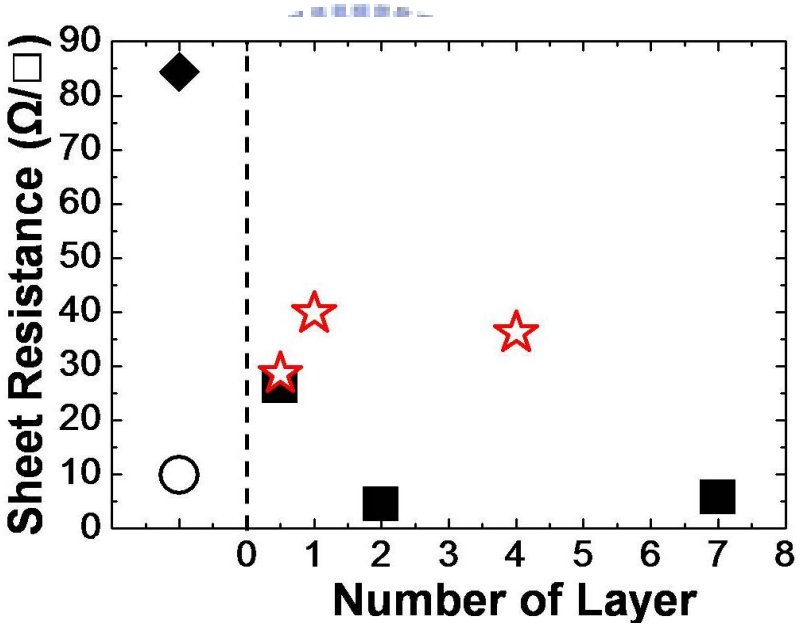

Figure 6.2 Plot of sheet resistance with respect to the layer number for NIO-660 (■) and NIO-460 (☆). The values for the as-deposited nickel film (◯) and ITO substrate (◆) are shown on the left for comparison purpose.

6.1.2 Resistivity of Cylindrical Inverse Opals

The CIO was regarded as a composite material that combines both CFs and Ni porous structure. Figure 6.3 presents the measurement setting for the CIO. The as-prepared CIO was mounted on an insulating glass with silver gels before taking the measurement. The I-V

curves were recorded with a two-probe measurement, and the distance between electrodes was controlledbetween 0.3 to 0.7 mm.

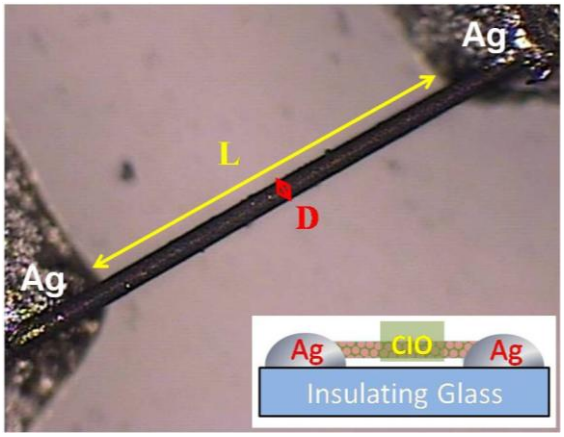

Figure 6.3 Optical image of silver electrodes on the CIO for electrical measurement. The sketch illustrates the setting in measurement.

To obtain the resistivity of CIOs, the measured value was calculated with following equation;

$$\rho = R \times \frac{L}{A} \qquad A = \pi \times \left(\frac{D}{2}\right)^2 \qquad \text{[eq. 6.2]}$$

where ρ is the resistivity of the composite, R is the resistance derived from the linear I-V curve, L is the distance between two measured electrodes, A is the cross-sectional area of the CIO, and D is the diameter of the CIO. As shown in Fig. 6.4, the resistivity of CIO was lower than that of pure CF. This indicated that the conductivity of the CF was improved by the Ni overcoats. Because the packing density of Ni for the CIO-460 and CIO-660 are almost equal, their resistivity both revealed at the same order as expected.

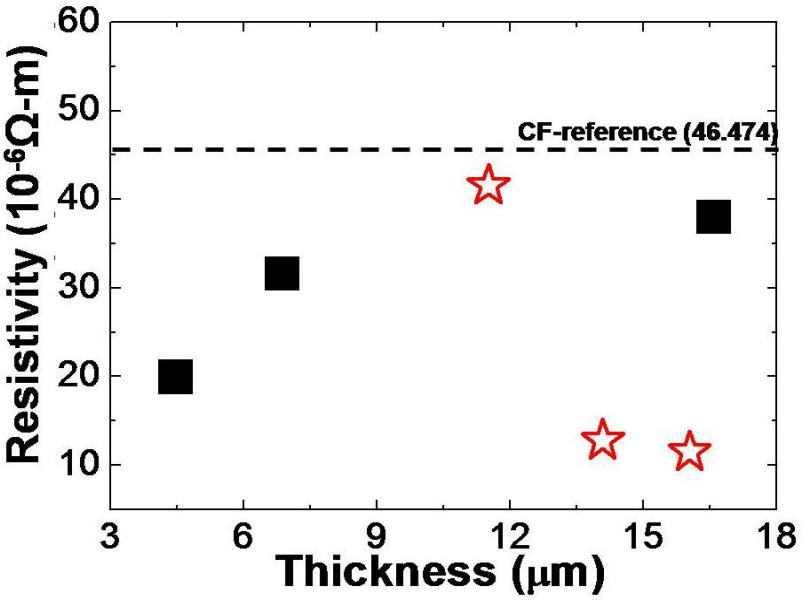

Figure 6.4 A plot of resistivity with respect to layer number for CIO-660s (■) and CIO- 460s (☆).

6.2 Optical Analyses

6.2.1 Reflection Spectra of Colloidal Crystals

Figure 6.5 presents the hybrid band structure of FCC performed by BandSOLVE Method with a commercial software (RSOFT). The index difference used in the simulation was 0.59 (PS:1.59; Air:1). In calculation, the forbidden band extended on Γ－L was at a region of 0.58~0.62. The corresponding photonic band gap (PBG) for the PCC-460 and PCC-660 were at the wavelength of 1049.26~1121.62 and 1505.45~1609.28 nm, respectively. To verify the calculation, near-IR reflectance spectra were obtained with an incidence light normal to the PCCs. Their spectra are provided in Fig. 6.6. The as-prepared PCC-460 and PCC-660 displayed peaks at 1088.87 and 1627.49 nm, which were close to the expected values from simulation. The slight discrepancy between the calculated values and the measured ones was resulted from the deviation in size of the PS microspheres, which was mentioned in chapter 4.

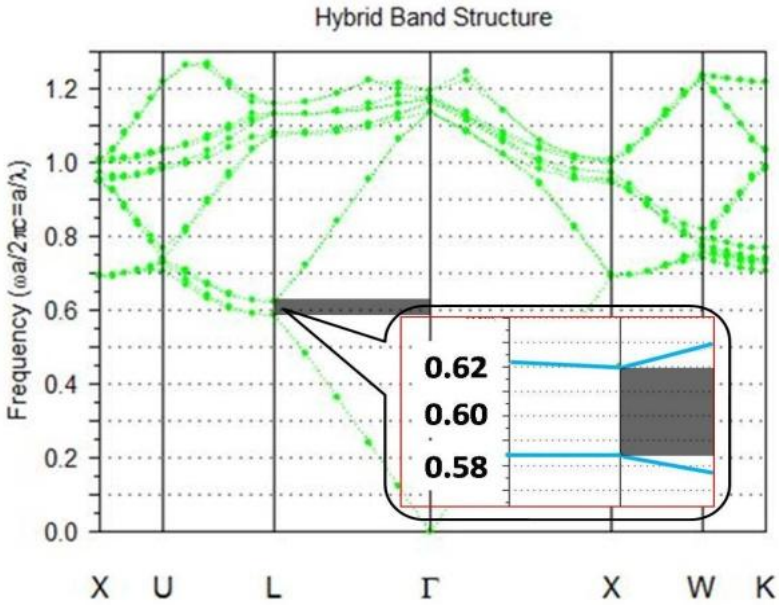

Figure 6.5 Simulated hybrid band structure of FCC with an index difference of 0.59.

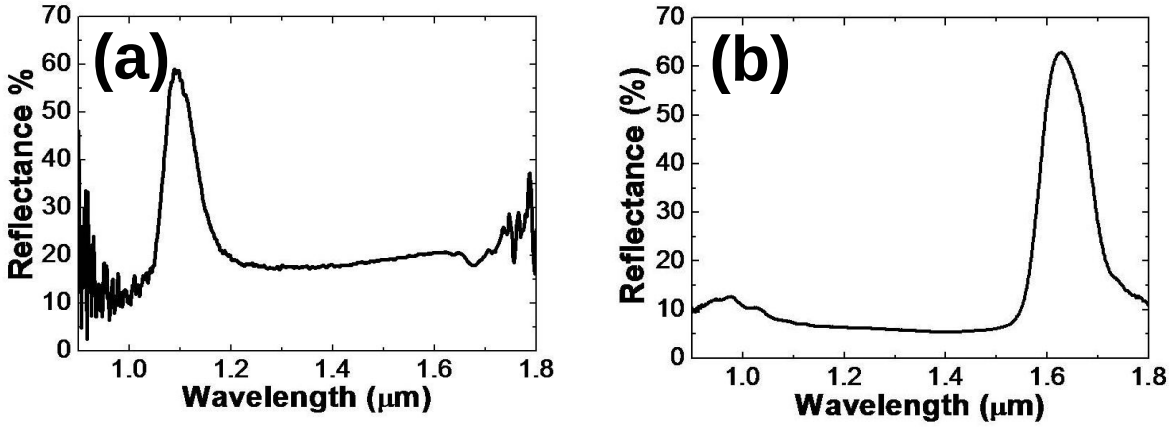

Figure 6.6 Reflectance spectra recorded from (a) PCC-460 and (b) PCC-660.

In addition, the reflectance at the PBG revealed a relatively high intensity about 60%. This level of reflectance justified the quality of PCCs made by the EPD process. The exact position of PBG can also be approached by the size of latex spheres via following equation [9]:

$$\lambda_c = 2n_{eff}d$$

$$n_{eff}^2 = n_{latex}^2 f + n_{air}^2(1-f) \qquad \text{[eq. 6.3]}$$

where λ_c is the wavelength where the PBG located, n_{eff} is the effective refractive index composed of latex and air, and d is the lattice spacing of (111) plane. In the equation [6.3], f is the filling factor of 0.74 for a close packed structure, and n_{latex}/n_{air} is the refractive index in each material. Following the equation, the positions of stop bands were expected to be 1104 and 1573 nm for PCC-460 and PCC-660, respectively. Notably, the measured values were also consistent with the ones from the equations above.

The CCCs were expected to reveal an unique optical response pattern due to the characteristic bending on the colloidal crystals. Before taking the measurement, the samples were fixed on a substrate that was not reactive in near-IR region. Then, the under measurement size was adjusted through an optical microscope to the area of individual CCC.

Figure 6.7 presents the reflectance spectra of CCCs prepared in different EPD time. Apparently, peak changes were observed in Fig. 6.7(a) of CCC-460 since the amount of effective (111) plane was increased with thickness. In contrast, a negligible difference was present for CCC-660, as provided in Fig. 6.7(b). It suggested that the structure of colloidal crystals was influenced by both the line defects and curved surface. Because the signal reflected from the CCCs was rather limited (in order to be collected by the detector), the peaks on these spectra only displayed a low reflectance of 5~20%.

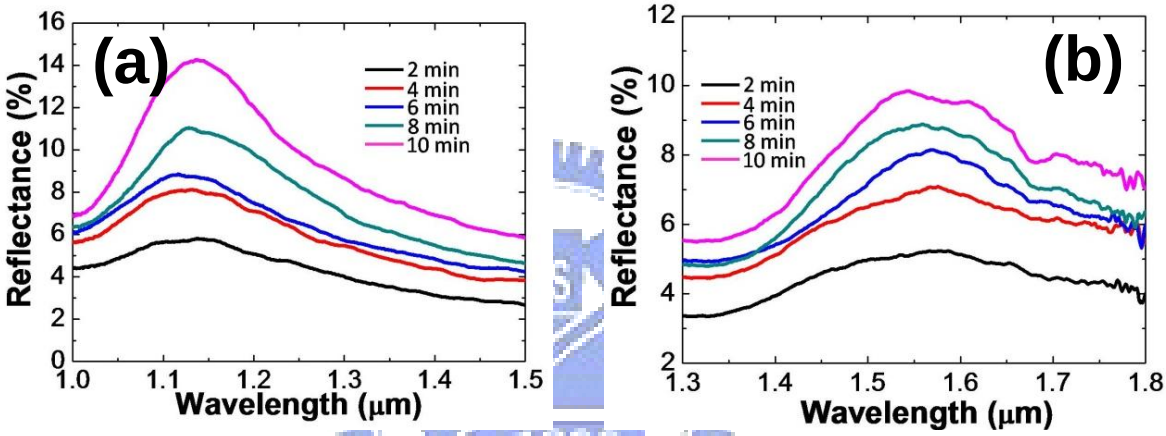

Figure 6.7 Reflectance spectra recorded from (a) CCC-460 and (b) CCC-660 for different EPD time.

A slight red shift from 1113.66 to 1135.61 nm was observed among the peaks from CCC-460. Theoretically, the filling factor (*f*) of air could be increased in a bent structure, making the peak closer to shorter wavelengths. Therefore, the position of peaks would move to longer wavelengths as the diameter of CCC was increased, until the distortion was fully compensated. It suggested that the bent structure in layer by layer formation might provide a continuous PBG. On the contrary, the peaks for CCC-660 remained unchanged with the increase of EPD time. This indicated that the stacking of PS microspheres was not sufficiently thick to compensate the bending in the structure within 10 min. Compared with these two cases, we can derive that the layers near the surface offered a distributed PBG

nature by its distortion, while layers far from the substrate contributed to the intensity of PBG just like a typical ordered structure.

Another contribution from the curved surface was that the half-height width was much broader than those recorded from the PCC. Because of the bending in the EPD layer, the lattice spacing of colloidal crystals on the (111) plane was slightly changed with a small angle. Its equilibrium was to produce a distribution of lattice constant. It was notable that the self-assembling of PS microspheres on CF demonstrated a model of scales. Hence, as difference in the size ratio of substrate to microsphere was close to 10~15, the colloidal crystals were bent into a non-closed packed structure. This bending behavior would decrease the intensity of PBG peaks. Nevertheless, the same bending structure could render a broadened PBG peak with a half-height width of 300 nm.

6.2.2 Light-Diffracting Fringes of Cylindrical Colloidal Crystals

Figure 6.8 exhibit the OM images for CCC-460 and CCC-660. Their surface displayed sparkling appearance in various color strips, and the color strips were aligned to each other. With a fixed light source, these color fringes were attributed to the light diffracting by the colloidal crystals from different angles.

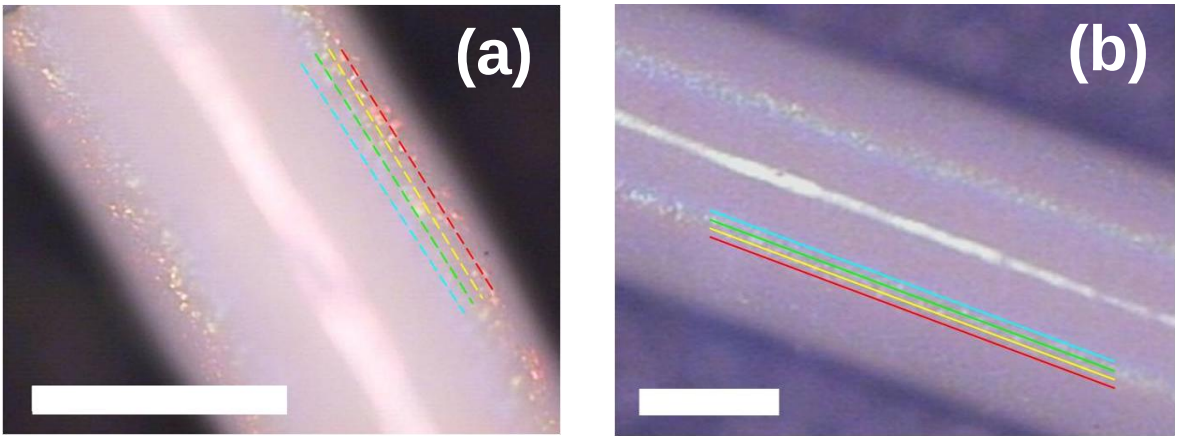

Figure 6.8 Color fringes in top view for (a) CCC-460 and (b) CCC-660. The scale bars are 200 μm. The fabrication times were 10min and 50 min, respectively.

Previously, V. Rastogi et al. [52] provided a model to demonstrate the reflection of parallel light waves that underwent a constructive or destructive interference, as shown in Fig. 6.9. The following equation derived from geometry in the figure illustrates the path difference of light waves;

$$\boldsymbol{m\lambda = d \times [sin(90 - \theta) + sin(\phi - \theta)]} \qquad \text{[eq. 6.4]}$$

where $\boldsymbol{m}$ is the integrals for the number of sets of fringes, $\boldsymbol{\lambda}$ is the wavelength of individual color fringe, $\boldsymbol{d}$ is the lattice spacing of (111) plane, and $\boldsymbol{\theta}$ and $\boldsymbol{\phi}$ are two specific angles defined from horizontal plane to the position of incident beams.

Because of the small diameter of the as-prepared CCCs, only the fringes in first order (**m = 1**) were obtained on the surface. Hence, the wavelength for the diffracting lights could be calculated through the equation by measuring each set of angles. Meanwhile, these fringes were observed under optical microscope, which inferred the incident light was normal to the surface ($\boldsymbol{\phi \sim 90^{\circ}}$). Therefore, the equation could be further simplified to:

$$\boldsymbol{\lambda = d \times [2sin(90 - \theta)] = 2d\cos\theta = 4ds/D} \qquad \text{[eq. 6.7]}$$

where $\boldsymbol{s}$ is the distance from the middle line to the fringe, and $\boldsymbol{D}$ is the diameter of the CCCs. From the modified equation, the wavelength of reflection can be easily calculated by the position of their fringes from OM images, as shown in Fig. 6.10. The inset bars exhibits the corresponding color of each wavelength via the RGB value translated from standard CIE 1931 chromaticity diagram [53]. The colors shown in Fig. 6.10 were partially matched with that obtained in OM observation. The deviation in color matching might be induced by a small tilt of the incident light.

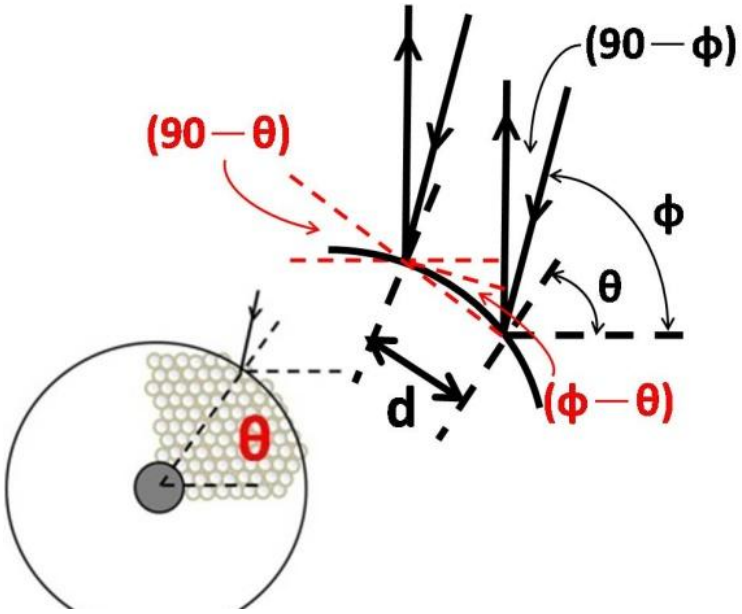

Figure 6.9 A schematic for theoretical calculation of fringe formation.

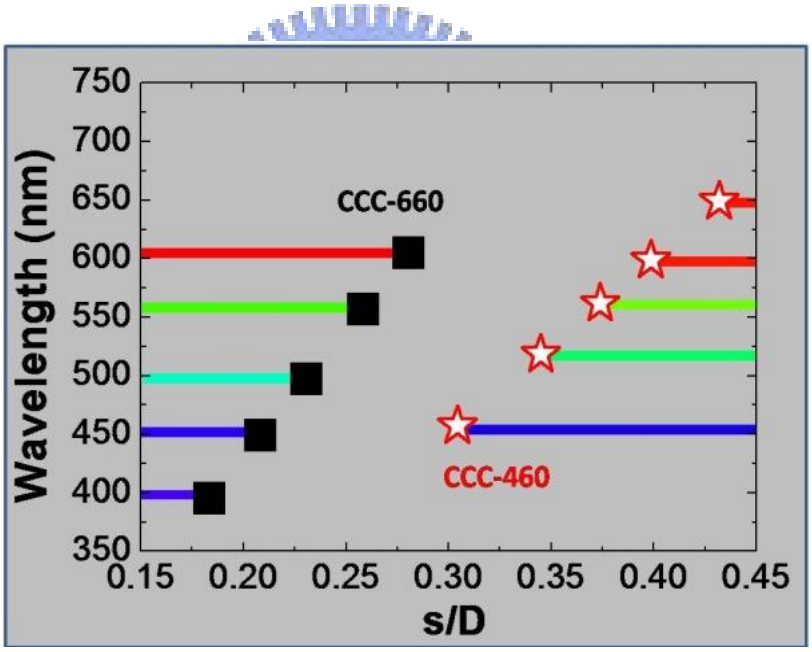

Figure 6.10 Wavelength of fringes versus the s/D plot of the CCCs for m = 1. The inset bars show the corresponded color created with RGB values on CIE 1931 chromaticity diagram.

6.2.3 Reflection Spectra of Nickel Inverse Opals

To obtain the PBG response of NIOs, the reflectance spectra were recorded with a normal light incidence in Mid-IR range. Figure 6.11 presents the reflectance spectra for the

NIO-660 with different number of layers. The Ni film provided a large reflectance in Mid-IR region, and maintained its value at 80% before entering the near-IR range. The noises detected at 2.62 and 4.25 μm were generated by the H_2O and CO_2, respectively. With a semi-layer NIO, the sample displayed a curve similar to that of the Ni film but at a slightly reduced reflectance. It suggested that the concave semi-layer structure engendered additional light scattering. Moreover, the PBG behavior was recorded as the layer number was increased. The NIO-660 with seven layers inverse structure revealed a curve whose intensity exhibited pronounced decay below 4 μm. In addition, the photonic band edge, defined at 50% reflectance, was observed at the wavelength of 2.25 μm on the plot.

The reflectance spectra of NIO-460 with different layer numbers are provided in Fig. 6.12. As expected, the PBG nature became evident as the thickness of NIO-460 was increased. As the layer number was increased to five, we could obtain characteristic photonic band edge, which was at the wavelength of 1.68 μm. Like the grid with smaller size, the reduction in the reflectance of NIO-460 occurred at a lower wavelength compared with that of NIO-660. The position for the photonic band edge can be approached with the real $\varepsilon_{real}(\lambda)$ and imaginary $\varepsilon_i(\lambda)$ dielectric constants of metals. The photonic band edge was predicted at a specific wavelength where the $|\varepsilon_{real}(\lambda)|$ was equal to $|\varepsilon_i(\lambda)|$ [19]. From the calculation using the dielectric constant of nickel [28], the edge of Ni was probably located at the wavelength of 2.48 μm. Therefore, we might expect that the photonic band edge would move to higher wavelengths with increasing layer numbers, until a steep drop in the reflectance was taking place.

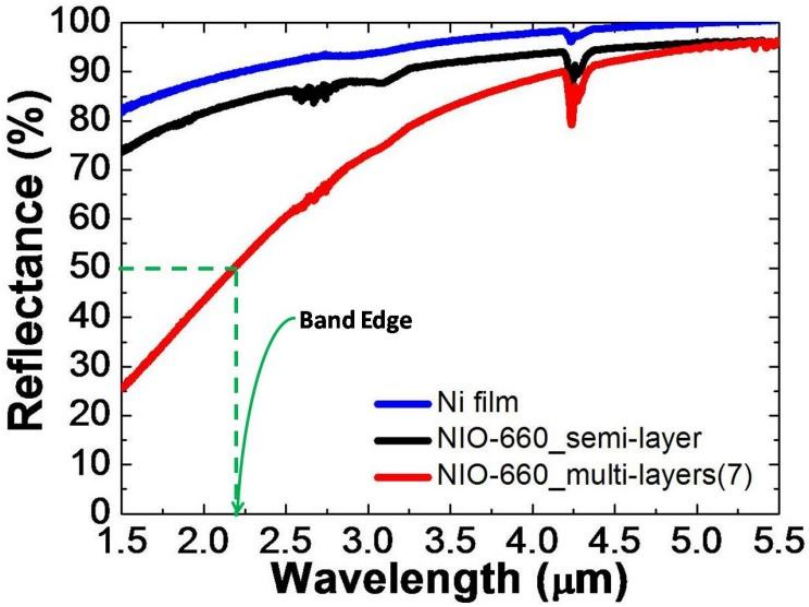

Figure 6.11 Mid-IR reflection spectra recorded from NIO-660 and Ni film.

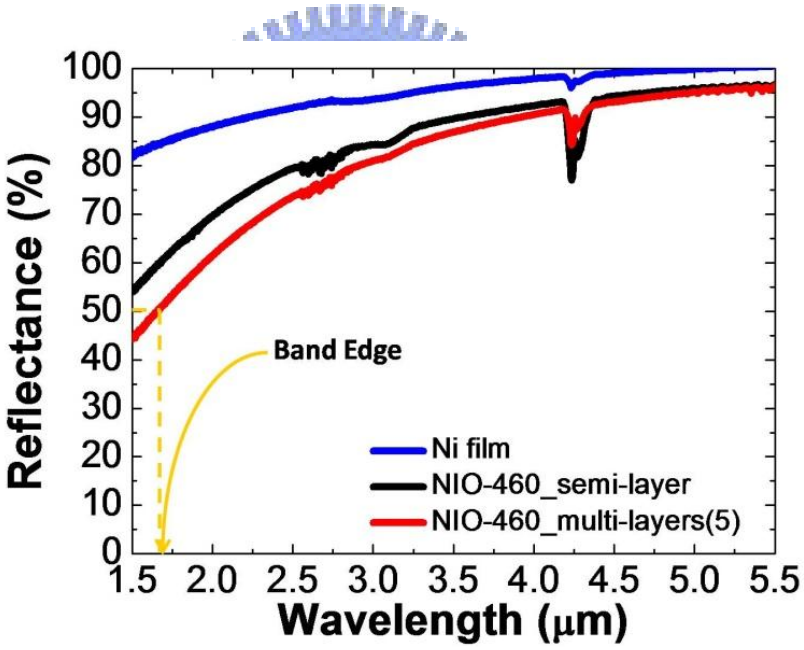

Figure 6.12 Mid-IR reflection spectra recorded from NIO-460 and Ni film.

Figure 6.13 provides the reflectance spectra of CIOs. In the measurement, the light source was illuminating at normal angle to the surface of CIOs. The reflectance from CIO revealed a characteristic oscillation in the region of long wavelength. It suggested that the CIO might serve as a cavity, rendering an optical resonance of standing EM waves. This evidence also inferred that the diameter of the CIOs was rather uniform so an optical resonance could be observed.

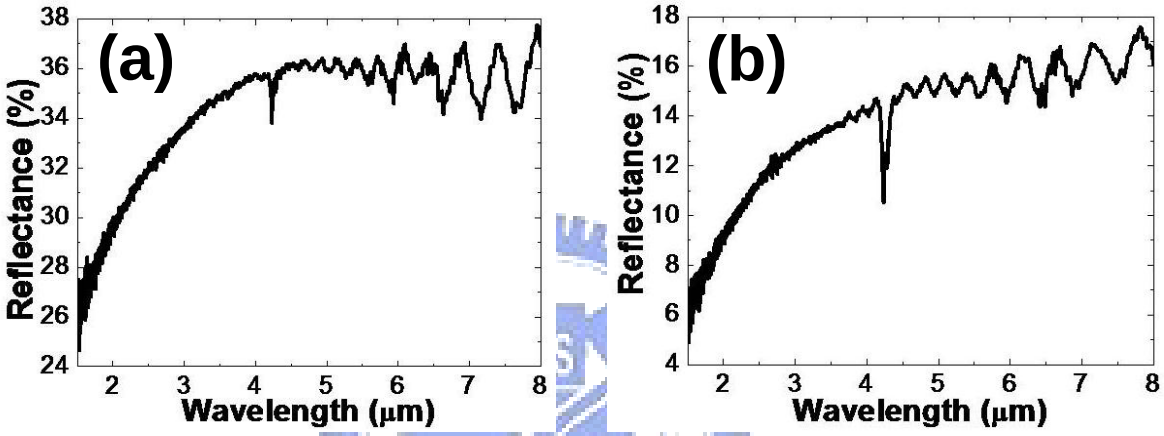

Figure 6.13 Mid-IR reflection spectra recorded from (a) CIO-660 and (b) CIO-460.

Chapter 7

Conclusions

Planar and cylindrical colloidal crystals were fabricated by electrophoretic depositions using 460 and 660 nm PS microspheres. With a moderate EPD rate, the PS microspheres were self-assembled into close-packed structures on the ITO substrate. However, in preparing the CCCs, the ordered arrangement of PS microspheres was affected by the curved surface of CF. The size difference between the microspheres and CFs determined the quality of CCCs. Hence, the CCC-460 revealed a higher quality than the CCC-660 as a result of size difference. Because the increase in the size of substrate provided a relatively flatter surface, the arrangement of PS microspheres on the CFs became ordered with the EPD time. In addition, the EPD rate on the CF was much larger than that on the ITO since the size of the CF was in micron scale.

Potentiostatic electrodeposition was carried out on the colloidal crystals to fabricate their nickel inverse opals. With a confined plating area, the growth of (220) plane was suppressed in NIOs. Moreover, the NIO-460 displayed only one preferred orientation of (111) plane. The current density versus time plot was recorded to connect with the thickness for the NIOs during the NED process. By controlling the NED time, semi-layer and multi-layer NIOs were successfully fabricated. In cylindrical cases, the NED rate for the CCC-660 was higher than that of CCC-460. A higher NED rate in the CCC-660 was resulted from its defective EPD layer, which was easier for Ni ions replenishment. Besides, the CIOs provided different profiles in microsphere arrangement, and the non-close packed structure was obtained in the near-CF regime. The ordered structure was observed as the thickness was increased, which was consistent with the observation in EPD process. In PS removal process, ethyl acetate was inefficient to clean the PS microspheres in the NIOs, even at a

temperature of 50 ℃. In contrast, thermal oxidation at 250 ℃ could not only remove the PS entirely without structure distortion, but also improve the crystallinity of NIOs.

In electrical properties, the sheet resistance of NIO-460 was larger than that of NIO-660. It suggested that the transport path for electrons was increased by the porous structure of NIOs. Furthermore, the CIOs revealed a lower resistivity than that of pure CF. In optical analyses, the as-prepared PCCs presented a high reflectance of 60 % at their photonic band gaps. On the other hand, the CCCs provided broader peaks because of the bending of the colloidal crystals. Moreover, the light-diffracting fringes were observed on the surface of the CCCs. By calculating the position of fringe, the observed color could be derived with CIE 1931 chromaticity diagram. Besides, the NIO displayed a photonic band edge in mid-IR range, and this character became obvious as the layer number of NIO was increased. For CIO, the reflectance with additional oscillation was observed as a result of optical resonance in a cavity structure.

References

[1] Yablonovitch E. Inhibited spontaneous emission in solid-state physics and electronics. Physical Review Letters. 1987;58(20):2059-62.

[2] John S. Strong localization of photons in certain disordered dielectric superlattices. Physical Review Letters. 1987;58(23):2486-9.

[3] Lee JH, Leung W, Ahn J, Lee T, Park IS, Constant K, et al. Layer-by-layer photonic crystal fabricated by low-temperature atomic layer deposition. Appl Phys Lett. 2007;90(15):3.

[4] Xia YN, Gates B, Yin YD, Lu Y. Monodispersed colloidal spheres: Old materials with new applications. Adv Mater. 2000;12(10):693-713.

[5] Noda S, Tomoda K, Yamamoto N, Chutinan A. Full three-dimensional photonic bandgap crystals at near-infrared wavelengths. Science. 2000;289(5479):604-6.

[6] Goncalves MC, Bras J, Almeida RM. Process optimization of sol-gel derived colloidal photonic crystals. Journal of Sol-Gel Science and Technology. 2007;42(2):135-43.

[7] Kim SH, Jeon SJ, Yi GR, Heo CJ, Choi JH, Yang SM. Optofluidic assembly of colloidal photonic crystals with controlled sizes, shapes, and structures. Adv Mater. 2008;20(9):1649-55.

[8] Dziomkina NV, Hempenius MA, Vancso GJ. Symmetry control of polymer colloidal monolayers and crystals by electrophoretic deposition onto patterned surfaces. Adv Mater. 2005;17(2):237-40.

[9] Rogach AL, Kotov NA, Koktysh DS, Ostrander JW, Ragoisha GA. Electrophoretic deposition of latex-based 3D colloidal photonic crystals: A technique for rapid production of high-quality opals. Chem Mat. 2000;12(9):2721-6.

[10] Yethiraj A, van Blaaderen A. A colloidal model system with an interaction tunable from

hard sphere to soft and dipolar. Nature. 2003;421(6922):513-7.

[11] Besra L, Liu M. A review on fundamentals and applications of electrophoretic deposition (EPD). Progress in Materials Science. 2007;52(1):1-61.

[12] Yang PD, Deng T, Zhao DY, Feng PY, Pine D, Chmelka BF, et al. Hierarchically ordered oxides. Science. 1998;282(5397):2244-6.

[13] Li F, Badel X, Linnros J, Wiley JB. Fabrication of colloidal crystals with tubular-like packings. Journal of the American Chemical Society. 2005;127(10):3268-9.

[14] Lin YK, Herman PR, Xu W. In-fiber colloidal photonic crystals and the formed stop band in fiber longitudinal direction. Journal of Applied Physics. 2007;102(7).

[15] Moon JH, Kim S, Yi GR, Lee YH, Yang SM. Fabrication of ordered macroporous cylinders by colloidal templating in microcapillaries. Langmuir. 2004;20(5):2033-5.

[16] Li JZ, Herman PR, Valdivia CE, Kitaev V, Ozin GA. Colloidal photonic crystal cladded optical fibers: Towards a new type of photonic band gap fiber. Optics Express. 2005;13(17):6454-9.

[17] Yu XD, Lee YJ, Furstenberg R, White JO, Braun PV. Filling fraction dependent properties of inverse opal metallic photonic crystals. Adv Mater. 2007;19(13):1689-92.

[18] Yang YL, Hou FJ, Wu SC, Huang WH, Lai MC, Huang YT. Fabrication and characterization of three-dimensional all metallic photonic crystals for near infrared applications. Appl Phys Lett. 2009;94(4):3.

[19] Lin SY, Ye DX, Lu TM, Bur J, Kim YS, Ho KM. Achieving a photonic band edge near visible wavelengths by metallic coatings. Journal of Applied Physics. 2006;99(8).

[20] Waterhouse GIN, Waterland MR. Opal and inverse opal photonic crystals: Fabrication and characterization. Polyhedron. 2007;26(2):356-68.

[21] Blanco A, Chomski E, Grabtchak S, Ibisate M, John S, Leonard SW, et al. Large-scale synthesis of a silicon photonic crystal with a complete three-dimensional bandgap near 1.5 micrometres. Nature. 2000;405(6785):437-40.

[22] Cong HL, Cao WX. Two-dimensionally ordered copper grid patterns prepared via electroless deposition using a colloidal-crystal film as the template. Advanced Functional Materials. 2005;15(11):1821-4.

[23] Hao Y, Zhu FQ, Chien CL, Searson PC. Fabrication and magnetic properties of ordered macroporous nickel structures. Journal of the Electrochemical Society. 2007;154(2):D65-D9.

[24] Yablonovitch E, Gmitter TJ. Photonic band-structure: the face-centered-cubic case. Physical Review Letters. 1989;63(18):1950-3.

[25] Yablonovitch E, Gmitter TJ, Leung KM. Photonic band structure: the face-centered-cubic case employing nonospherical atoms. Physical Review Letters. 1991;67(17):2295-8.

[26] Ho KM, Chan CT, Soukoulis CM, Biswas R, Sigalas M. Photonic band gaps in 3-dimensions: new layer--by-layer peroidic structures. Solid State Communications. 1994;89(5):413-6.

[27] Busch K, John S. Photonic band gap formation in certain self-organizing systems. Physical Review E. 1998;58(3):3896-908.

[28] Palik ED. Handbook of optical constants of solids. London: Academic press 1985. p.323.

[29] Wang Z, Chan CT, Zhang W, Ming N, Sheng P. Three-dimensional self-assembly of metal nanoparticles: Possible photonic crystal with a complete gap below the plasma frequency. Physical Review B. 2001;64(11):113108-.

[30] Inoue M, Arai K, Fujii T, Abe M. One-dimensional magnetophotonic crystals. 43rd Annual Conference on Magnetism and Magnetic Materials; 1998; Miami, Florida. p. 5768-70.

[31] Inoue M, Fujikawa R, Baryshev A, Khanikaev A, Lim PB, Uchida H, et al. Magnetophotonic crystals. J Phys D-Appl Phys. 2006;39(8):R151-R61.

[32] Kasap SO. Optoelectronics and photonics: principles and practices: Prentice Hall 2001. p. 27.

[33] Cregan RF, Mangan BJ, Knight JC, Birks TA, Russell PS, Roberts PJ, et al. Single-mode photonic band gap guidance of light in air. Science. 1999;285(5433):1537-9.

[34] Garcia-Santamaria F, Lopez C, Meseguer F, Lopez-Tejeira F, Sanchez-Dehesa J, Miyazaki HT. Opal-like photonic crystal with diamond lattice. Appl Phys Lett. 2001;79(15):2309-11.

[35] Everett DH. Basic principles of colloid science. Royal Society of Chemistry. 1988.

[36] Solomentsev Y, Bohmer M, Anderson JL. Particle clustering and pattern formation during electrophoretic deposition: A hydrodynamic model. Langmuir. 1997;13(23):6058-68.

[37] Huang YJ, Lai CH, Wu PW. Fabrication of Large-Area Colloidal Crystals by Electrophoretic Deposition in Vertical Arrangement. Electrochemical and Solid-State Letters. 2008;11:P20.

[38] Miguez H, Yang SM, Tetreault N, Ozin GA. Oriented free-standing three-dimensional silicon inverted colloidal photonic crystal microfibers. Adv Mater. 2002;14(24):1805-8.

[39] Wang H, Li X, Nakamura H, Miyazaki M, Maeda H. Continuous particle self-arrangement in a long microcapillary. Adv Mater. 2002;14(22).

[40] Zheng YB, Juluri BK, Huang TJ. The self-assembly of monodisperse nanospheres within microtubes. Nanotechnology. 2007;18(27):275706.

[41] Moon JH, Yi GR, Yang SM. Fabrication of hollow colloidal crystal cylinders and their inverted polymeric replicas. Journal of Colloid and Interface Science. 2005;287(1):173-7.

[42] Paunovic M, Schlesinger M. Fundamentals of electrochemical deposition: Wiley-Interscience 2006. p. 53-8.

[43] Kavan L, Zukalova M, Kalba M, Graetzel M. Lithium insertion into anatase inverse opal. Journal of the Electrochemical Society. 2004;151:A1301.

[44] Bartlett PN, Baumberg JJ, Coyle S, Abdelsalam ME. Optical properties of nanostructured metal films. Faraday Discussions. 2004;125:117-32.

[45] Bartlett PN, Birkin PR, Ghanem MA. Electrochemical deposition of macroporous

platinum, palladium and cobalt films using polystyrene latex sphere templates. Chemical Communications. 2000;2000(17):1671-2.

[46] Chung YW, Leu C, Lee JH, Yen JH, Hon MH. Fabrication of various nickel nanostructures by manipulating the one-step electrodeposition process. Journal of the Electrochemical Society. 2007;154:E77.

[47] Napolskii K, Sapoletova N, Eliseev A, Tsirlina G, Rubacheva A, Gan'shina E, et al. Magnetophotonic properties of inverse magnetic metal opals. Journal of Magnetism and Magnetic Materials. 2009; 321:833-5.

[48] Napolskii KS, Sinitskii A, Grigoriev SV, Grigorieva NA, Eckerlebe H, Eliseev AA, et al. Topology constrained magnetic structure of Ni photonic crystals. Physica B: Physics of Condensed Matter. 2007;397(1-2):23-6.

[49] Chung YW, Leu IC, Lee JH, Yen JH, Hon MH. Fabrication of egg-shell-roofed macroporous nickel films by a template-mediated electrodeposition process. Electrochimica Acta. 2007;53(4):1703-7.

[50] Sumida T, Wada Y, Kitamura T, Yanagida S. Construction of stacked opaline films and electrochemical deposition of ordered macroporous nickel. Langmuir. 2002;18(10):3886-94.

[51] Biesheuvel PM, Verweij H. Theory of cast formation in electrophoretic deposition. Journal of the American Ceramic Society. 1999;82(6):1451-5.

[52] Rastogi V, Melle S, Calderon OG, Garcia AA, Marquez M, Velev OD. Synthesis of Light-Diffracting Assemblies from Microspheres and Nanoparticles in Droplets on a Superhydrophobic Surface. Adv Mater. 2008;20(22):4263-8.

[53] Orava J, Jaaskelainen T, Parkkinen J, Leppanen VP. Diffractive CIE 1931 chromaticity diagram. Color Research and Application. 2007;32(5):409-13.